Improving Condition and Sensitivity of Linear Inverse Problems in Magnetic Applications

Dissertation zur Erlangung des akademischen Grades
Doktoringenieur (Dr.-Ing.)

vorgelegt der Fakultät für Informatik und Automatisierung
der Technischen Universität Ilmenau

von Dipl.-Inf. Roland Eichardt

Gutachter: 1. Prof. Dr.-Ing. habil. Jens Haueisen
2. Prof. Dr. Marko Vauhkonen
3. Prof. Dr. Luca Di Rienzo

Tag der Einreichung: 29. September 2011
Tag der wissenschaftlichen Aussprache: 12. Januar 2012

urn:nbn:de:gbv:ilm1-2012000170

Abstract

The identification and reconstruction of hidden, not directly accessible processes from measured data is important in many areas of research and engineering. This thesis focusses on applications in magnetostatics, magnetocardiography, and magnetic induction tomography. One approach to identify these processes is to solve a related linear inverse problem. Unfortunately, noise and errors in the data have a significant impact on inverse solutions.

The aim of this work is to reduce the effects of noise and errors by improving the condition of the problem and to increase the sensitivity of measurement setups. To quantify the condition, we propose the ratio of the largest and the mean singular value of the kernel matrix. Moreover, we outline approaches to analyse quantitatively and qualitatively the sensitivity to electromagnetic sources and electrical conductivity changes.

In four simulation studies, strategies to improve the condition and sensitivity in magnetic applications are described. First, we present a tabu search algorithm to optimize arrangements of magnetic sensors. Optimized sensor arrays result in a considerably improved condition compared with regular arrangements. Second, we adapt parameters that define source space grids for magnetic nanoparticle imaging. One conclusion is that the source space should be defined slightly larger than the sensor area. Third, we demonstrate for mono-axial sensor arrays that variations in the sensor directions and small variations in the sensor positions lead to improvements of the condition, too. Finally, we evaluate and compare the sensitivities of six coil setups for magnetic induction tomography. Our investigations indicate a rapid decay of sensitivity by several orders of magnitude within a range of a few centimetres. By using relatively large coils that cover the measurement region almost completely, the condition and sensitivity can be improved clearly.

The methods and strategies presented in this thesis facilitate substantial improvements of the condition for linear inverse problems in magnetic applications. In particular, the arrangement of sensors relative to the measurement object is critical to the condition and to the quality of inverse solutions. Moreover, the presented methods are applicable to linear inverse problems in various fields.

Zusammenfassung

Die Identifikation nicht direkt zugänglicher Prozesse anhand gemessener Daten ist von großer Bedeutung in vielen Bereichen. Im Fokus dieser Arbeit liegen Applikationen in der Magnetostatik, Magnetokardiographie und Magnetinduktionstomographie. Ein Ansatz zur Identifikation besteht in der Lösung eines entsprechenden linear inversen Problems. Unglücklicherweise haben in den Daten enthaltene Fehler und Rauschen einen signifikanten Einfluss auf die inverse Lösung.

Ziel dieser Arbeit ist die Reduktion der Einflüsse von Fehlern und Rauschen durch eine Verbesserung der Kondition des Problems, sowie eine Steigerung der Sensitivität der Messanordnungen. Zur Bestimmung der Kondition wird das Verhältnis des größten und mittleren Singulärwerts der Kernmatrix als neues Maß vorgeschlagen. Darüber hinaus werden Ansätze zur Analyse der Sensitivität hinsichtlich der Messung elektromagnetischer Quellen und der Erfassung elektrischer Leitfähigkeitsveränderungen präsentiert.

Strategien zur Verbesserung von Kondition und Sensitivität werden in vier Simulationsstudien beschrieben. In der ersten Studie wird ein Tabu-Suche-Ansatz zur Optimierung der Anordnung magnetischer Sensoren vorgestellt. Anordnungen mit optimierte Sensorpositionen resultieren dabei in einer deutlich besseren Kondition als regelmäßige Anordnungen. In einer zweiten Studie werden Parameter adaptiert, welche den Quellenraum für die Bildgebung durch magnetische Nanopartikel definieren. Als eine Schlussfolgerung sollte der Quellenraum etwas größer als das Sensorareal definiert werden. Diese Arbeit zeigt ebenfalls, dass Variationen in den Sensorrichtungen für monoaxiale Sensorarrays zu einer Verbesserung der Kondition führen. Zudem wird die Sensitivität von Spulenanordnungen für die Magnetinduktionstomographie bewertet und verglichen. Durch Nutzung relativ großer Spulen, die das Messgebiet nahezu vollständig abdecken, können Kondition und Sensitivität wesentlich verbessert werden.

Die präsentierten Methoden und Strategien ermöglichen eine substantielle Verbesserung der Kondition des linear inversen Problems bei der Analyse magnetischer Messungen. Insbesondere die Anordnung von Sensoren in Bezug auf das Messobjekt ist kritisch für die Kondition, sowie die Qualität inverser Lösungen. Die vorgestellten Methoden sind darü ber hinaus für linear inverse Probleme in zahlreichen Bereichen einsetzbar.

Acknowledgements

I am greatly indebted to my supervisor Jens Haueisen for guiding my research and for always finding time to discuss scientific results and new ideas during the last years.

Many colleagues associated with the Ilmenau University of Technology, the Jena University Hospital, and Philips Research in Aachen directly or indirectly supported my work. My publications would not have been possible without the common effort of all authors. I thank these people for the efficient and pleasant cooperation I constantly experienced through my graduation time.

Furthermore, I thank Stephan Lau for the contribution of the simulation results shown in section 4.2.3. Various comments and suggestion from Daniel Baumgarten, Jens Haueisen, Stephan Lau, Luca Di Rienzo, and Marko Vauhkonen helped to improve my thesis.

My final thanks are directed to Uwe Graichen for answering all my LaTeX-related questions and for providing a versatile template, which I used for writing this thesis.

Nomenclature

Acronyms

AtB	Advanced Technologies Biomagnetics, Pescara, Italy
BEM	boundary element method
ECG	electrocardiography
EEG	electrocardiography
EFEM	edge finite element method
FEM	finite element method
GCV	generalized cross validation
MCG	magnetocardiography
MEG	magnetoencephalography
MIT	magnetic induction tomography
PSO	particle swarm optimization
PTB	Physikalisch-Technische Bundesanstalt, Berlin, Germany
SD	standard deviation
SNR	signal to noise ratio
SQUID	superconducting quantum interference device
STL	standard template library
SVD	singular value decomposition

TSVD	truncated singular value decomposition
VOI	volume of interest

Notations

0	matrix or vector with all elements 0
A	matrix, $A \in \mathbb{R}^{m \times n}$
$A[i, \sim]$	ith row of A
$A[i, j]$	element of row i and column j of A
$\mathrm{B}(i, j, t)$	magnetic field at integration point t of sensor i, originating from source j, $\mathrm{B}(i, j, t) \in \mathbb{R}^{3 \times 1}$
b	vector of magnetic measurement values, $b \in \mathbb{R}^{m \times 1}$
c	changes of electrical conductivity, $v \in \mathbb{R}^{m \times 1}$
$\mathbb{C}$	complex field
$\kappa_p(A)$	condition number of A with respect to p-norm
$\kappa(A)$	condition number of A with respect to 2-norm
d_i	direction of sensor i, $d_i \in \mathbb{R}^{3 \times 1}$, $\|d_i\| = 1$
$\mathrm{diag}(x)$	matrix with diagonal elements x
e_j	direction of source j, $e_j \in \mathbb{R}^{3 \times 1}$
$\exp(x)$	exponential function, e^x
$\mathcal{F}$	non-linear forward operator
I	identity matrix
J	Jacobian matrix, real part, $J \in \mathbb{R}^{m \times n}$
L	lead field matrix, $L \in \mathbb{R}^{m \times n}$
$\mathbb{N}$	natural numbers including 0
$O(\cdot)$	quantification of computational costs, O-notation
p	vector of dipole moments, $p \in \mathbb{R}^{n \times 1}$
p-norm of x	$(\sum_i \lvert x[i] \rvert^p)^{1/p}$, $p \geq 1$
r, $\mathrm{rank}(A)$	rank of matrix A

$rd(A)$	relative determination with respect to a linear operator A
$\mathbb{R}$	real field
$\mathbb{R}^+$	real field of numbers > 0
$\mathbb{R}^\star$	real field without 0
r_{ijt}	displacement vector between integration point t of sensor i and source j
$\tilde{r}_{ijt}$	displacement unit vector corresponding to r_{ijt} with $\|\tilde{r}_{ijt}\|_2 = 1$
σ_i, $\sigma_i(A)$	ith singular value of A
s	total number of singular values of A, including 0; $s := \min(m, n)$
S^A	sensitivity with respect to a linear operator A
v	measured secondary voltage differences, $v \in \mathbb{R}^{m \times 1}$
w_{it}	weight of integration point t of sensor i, $w_{it} \in \mathbb{R}^\star$

Symbols

A^{-1}	inverse of A
A^+	Moore-Penrose inverse (pseudo-inverse) of A
A^T	A transposed
$\|\cdot\|$	absolute values of matrix, vector, scalar elements; number of set elements
$\|\cdot\|_p$	p-norm of matrix or vector
$\mathtt{A} := \mathtt{B}$	`A` is defined by `B`
$\mathtt{A} \implies \mathtt{B}$	if `A` then `B`
$\mathtt{A} \iff \mathtt{B}$	`A` if and only if `B`
$\wedge$	logical conjunction
$\vee$	logical disjunction
$\leftarrow$	assignment in algorithms
$a \cdot b$	scalar product of vectors a and b
$\exists$	existential quantifier

$\forall$	universal quantifier
$\setminus$	relative complement of sets
$\cup$	union of sets
$\times$	product of scalars; Cartesian product of sets

Notation

Positions, coordinates and distances are in units of m, unless otherwise stated. The sensitivities of magnetometer arrays to magnetostatic dipoles are in units of $\mathrm{TA}^{-1}\mathrm{m}^{-2}$, and the sensitivities of magnetic induction tomography systems to conductivity changes are in VmS^{-1}. The moments of magnetic dipoles are given in Am^2 and the electrical conductivities are in Sm^{-1}. Matrices are indicated by upper case, vectors and scalars by lower case italic letters. We use i, j, and k as indices.

The PDF file of this document provides for all links to figures, tables, sections, and publications also the corresponding hyper-references. Digital object identifiers (doi) in the bibliography refer to the full texts on the publisher's websites. Page numbers in the bibliography link back to the citing pages.

Contents

1 Introduction

1.1. Inverse Problems in Magnetic Applications

Overview

Inverse problems arise in almost all fields of science and engineering. On the basis of observed data, an inverse problem consists in the identification and reconstruction of the underlying causes. This reconstruction can provide essential insight into hidden, not directly accessible processes of interest.

To solve inverse problems, an appropriate modelling of the causes, the observed data, and their interaction is generally required. Since the majority of inverse problems can not be solved directly, an iterative optimization or linearization techniques are utilized. Unfortunately, the solutions may not exist or be unique, and small changes in the observations can lead to substantial changes in the results. Inevitable errors and noise contained in the measurement data can lead to dominant interferences in inverse solutions. We term inaccuracies that originate, for instance by limitations of floating point numbers, data sampling and quantization processes as *errors*, and parts of the measurement that not represent the signals of interest as *noise*.

Linear inverse problems, where small changes in the measurement data can have substantial effects on the solution, are denoted as *ill-conditioned*. Imposed *a priori* assumptions enable effective solutions of inverse problems. During the last decades, numerous approaches that reduce the influence of noise and errors within the solution process were proposed.

Our objective is to improve the condition of linear inverse problems in magnetic applications to generally reduce the effects of noise and errors on solutions, independently from specific linear inverse methods. Moreover, the sensitivity of measurement systems can be very low. We present methods to analyse and to compare the sensitivity of different measurement setups to further improve solutions of linear inverse problems.

This work focusses on applications, in which static magnetic or quasi-static electrical sources are reconstructed from magnetic measurements. Furthermore, we consider

the application of estimating changes of the electrical conductivities by magnetic induction tomography.

Reconstructing Static Magnetic Sources

Typical applications that involve magnetostatic inverse problems are the reconstruction of magnetic nanoparticles distributions for imaging purposes [Baumgarten et al. 2008], the localization of magnetic markers in the gastro-intestinal system [Hilgenfeld and Haueisen 2004], and the detection of buried magnetic objects from geomagnetic measurements [Eichardt et al. 2009a]. In these examples, measured magnetic activities originate from almost static magnetic sources, which can be approximated by magnetostatic dipoles.

For the imaging of magnetic nanoparticles, functionalized particles with diameters in the range of nanometres are applied to a sample under test. Owing to active and passive distribution processes, nanoparticles spread in a sample and bind to target structures, such as tumour cells. Subsequently, bound and unbound nanoparticles are magnetized until saturation using a static external field. When turning off this magnetic field, particles start to align back to random orientations. In this process of relaxation, a decay of the magnetic remanence field caused by aligned particles can be observed. The reorientation of particles bound to target structures in absence of an external magnetic field ensues relatively slowly and is referred to as Nèel relaxation. The remanence field and the Nèel relaxation can be measured using highly sensitive sensor technologies.

In geomagnetic applications, hidden ferromagnetic and paramagnetic objects cause deformations of the quasi-homogeneous magnetic field of the earth. Based on magnetic measurements at the ground surface, one can determine positions of hidden objects using inverse methods. Since the earths magnetic field is changing very slowly, we can assume static magnetic sources. Accordingly, compact and sufficiently distant magnetic objects can be approximated by magnetostatic dipoles.

Previous work in this field was presented by McFee et al. [1990], Barrell and Naus [2007], and Sheinker et al. [2009]. In [Eichardt et al. 2009a], we deployed a measurement system that exhibited several gradiometer sensors mounted on a non-metallic vehicle, which could be pulled by car over ground surface. Recorded sets of data typically consisted of successively scanned lines with sample point distances of a few centimetres or less and line-to-line distances of about 0.5 m. Differential GPS (global positioning system) and inertial sensors provided sensor positions and orientations for each measurement sample.

Reconstructing Bioelectrical Current Sources from Magnetic Measurements

The reconstruction of electrical currents or potentials from measured magnetic fields of the human heart (magnetocardiography, MCG) and brain (magnetoencephalography, MEG) plays a vital role in research and medical diagnosis.

We apply the tabu search algorithm to optimize sensor arrangements in MCG. First recordings of the magnetic field of the heart using single coils were presented by Baule and McFee [1963]. Today, sensor systems with several hundred sensors cover major regions of the chest to measure the magnetic fields emerging from physiologic or pathophysiologic cardiac processes. To reconstruct the underlying electrical activities, a person-specific volume conductor model of the torso is typically used. The electromagnetic model is based on quasi-static approximations of Maxwell's equations, since frequencies of biological electrical currents are in the range of or below 1 kHz. Relevant clinical applications of the MCG include the localization of ventricular arrhythmogenic sites in patients suffering from Wolff-Parkinson-White syndrome [Nenonen et al. 1993; Leder et al. 2001] and the imaging of delayed high-frequency depolarization signals indicating the risk of malignant tachyarrhythmias after myocardial infarction [Leder et al. 1998]. Surveys on MCG are provided by Andrä and Nowak [2006, section 2.3], Clark and Braginski [2006, section 11.3], and Weinstock [1996, chapter 10].

Reconstructing Electrical Conductivities by Magnetic Induction

The aim of the magnetic induction approach is the reconstruction of the electrical conductivity and permittivity of objects such as the human head or body. By using multiple coils for exciting and measuring magnetic fields, magnetic induction tomography (MIT) enables a visual representation of electrical conductivity and permittivity values of the measurement object.

When emitting time-varying magnetic fields to an electrically conducting object, eddy currents emerge depending on conductivity, permittivity, and permeability. In turn, these eddy currents produce secondary magnetic fields, which can be measured by coils. Primary and secondary magnetic fields cause inductions of primary and phase-shifted secondary voltages at the measurement coils. As a consequence of low conductivities of biological tissue, secondary voltages are very weak in biomedical applications.

The first work in the area of magnetic induction from Tarjan and McFee [1968] focused on the detection of vital signs. The first MIT system was presented by Netz et al. [1993]. Further concepts of tomographic systems were published, for example by Korjenevsky et al. [2000], Igney et al. [2005], Watson et al. [2008], Scharfetter et al. [2008], and Vauhkonen et al. [2008]. Applications of magnetic induction and MIT include monitoring of vital parameters, detection of bleedings, and sensing of defects in metal components. An overview of MIT is given by Griffiths [2001].

1.2. Outline of this Thesis

In the subsequent chapter 2, we address definition and properties of linear inverse problems in magnetic applications, describe the setup of related kernel matrices, and take a look at methods to solve linear inverse problems.

Chapter 3 presents methods to assess the condition and sensitivity, both representing practically important properties of kernel matrices related to linear inverse problems. To evaluate the condition, the condition number with respect to the 2-norm is used. Furthermore, we deploy a new measure that quantifies the ratio of largest and mean singular value of kernel matrices. Both measures are also defined relative to the kth singular value, which can be relevant, for example when comparing the condition for sensor systems with different numbers of sensors.

In chapter 4, we describe strategies to evaluate and improve the condition and the sensitivity in magnetic applications. A tabu search algorithm for the optimization of sensor arrangements is presented in section 4.2. We demonstrate the improvement of the condition in the application of MCG, when optimized sensor positions are used instead of regular sensor arrangements. Section 4.3 shows the effects of adaptations of source grid parameters on the condition of linear inverse problems in magnetic nanoparticle imaging. The results indicate that the area of the source space should extend the sensor area slightly. The number of sources considerably affects the condition, in case that fewer sources than sensors are utilized. By using generic examples of mono-axial sensor arrays, we show in section 4.4 that variations in the sensor directions and small variations in the sensor positions lead to improvements of the condition, too. Sensitivities of different coil setups for MIT are evaluated and compared in section 4.5. We observe a rapid decay of the sensitivity by several orders of magnitude within a relatively small range between coils and volume elements.

The main part is closed by general conclusions and an outlook in chapter 5. In appendix A, we present a supplemental study on linear inverse problems in magnetic applications. It reveals that predefining the directions of sources mainly improves the condition, if in this process the degree of overdetermination is considerably increased. Appendix B provides general details on the singular value decomposition, the Moore-Penrose inverse, and matrix norms.

Unless stated otherwise, this thesis represents my own scientific work. This also applies for parts that are based on joint publications. Contents that originate from other people's work are identified correspondingly. Figure 1.1 outlines the structure of this thesis at a glance.

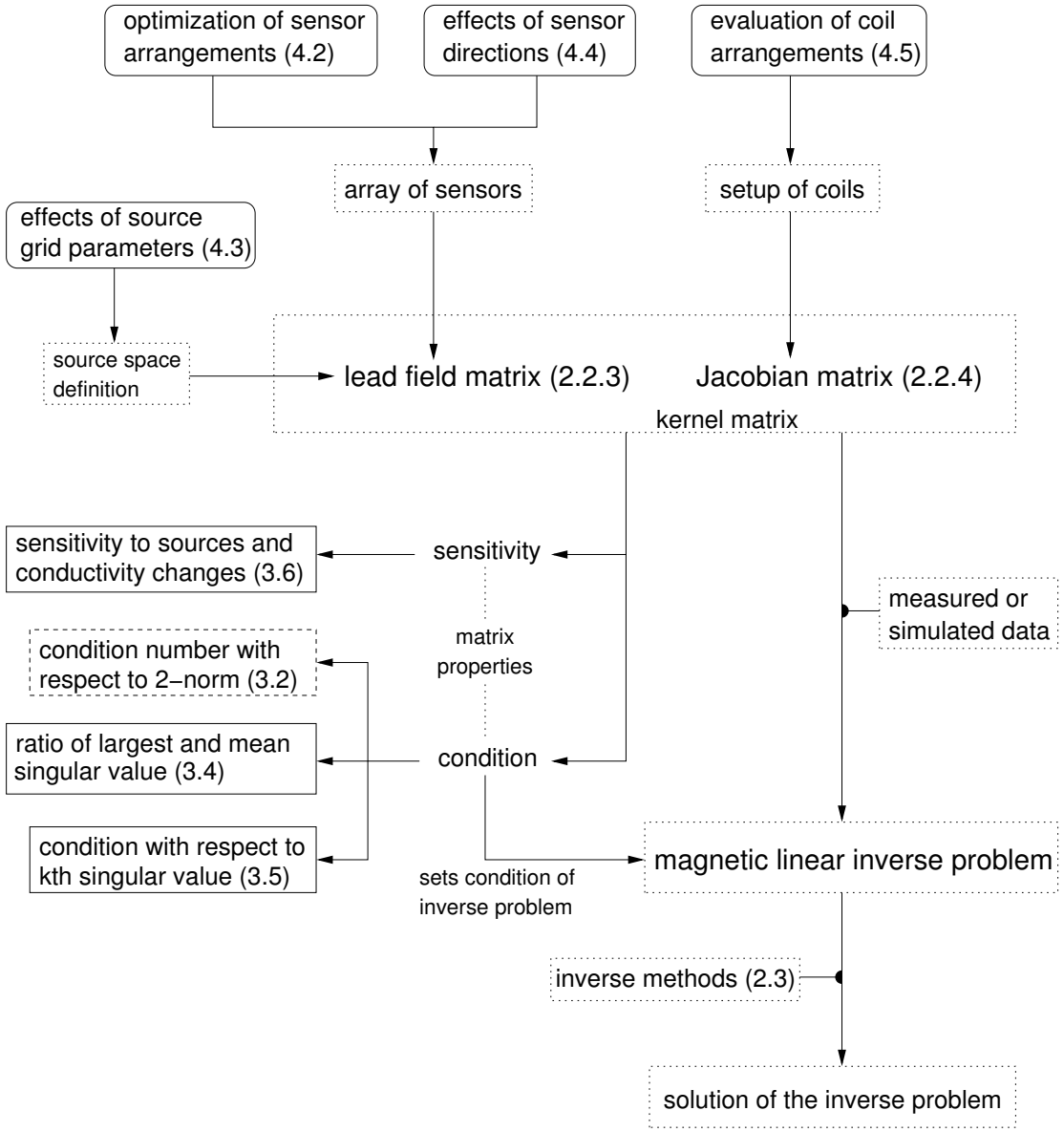

Figure 1.1.: Outline of this thesis. Major investigations are indicated by boxes with rounded edges. Newly defined measures for the evaluation of the condition and sensitivity of kernel matrices are represented by solid rectangles. References to the particular sections of this thesis are given in parenthesis.

2 Theory of Inverse Problems in Magnetics

2.1. Magnetic Sensors, Sensor Arrays, and Models

Sensor systems can utilize different types of sensors to measure the magnetic field (magnetometers) or its gradient (gradiometers). Two of the currently most relevant sensor technologies are coils and superconducting quantum interference devices (SQUIDs).

The measurement principle of coils is based on Faraday's law of induction. Coils measure the temporal derivative of the magnetic flux $\mathrm{d}\Phi/\mathrm{d}t$ with $\Phi = BA$. The sensitivity to the magnetic field B depends inherently on the cross sectional area A and the number of windings. However, these parameters are usually subject to practical restrictions. Highly sensitive coil magnetometers result in substantial sensor dimensions, such as in the first MEG experiment by Cohen [1968]. In the field of MIT, coils are applied for the measurement and excitation of magnetic fields using frequencies in the range of megahertz, as they are required to induce eddy currents for conductivity measurements. In combination with SQUID sensors, coils increase the sensor pickup area and enable the design of gradiometers.

An overview on the technology of SQUIDs, SQUID systems, and their applications give, for instance Clark and Braginski [2004, 2006] and Andrä and Nowak [2006]. Presently, SQUIDs represent one of the most sensitive technologies to measure magnetic fields at lowest levels of noise. The measurement principle bases essentially on two quantum mechanical phenomena: flux quantization, first predicted by London [1950], and the Josephson effect described by Josephson [1962]. First publications on SQUID-based sensor technologies were presented by Jaklevic et al. [1964] and Silver and Zimmerman [1967]. SQUID sensors are small in size, but require liquid helium (low temperature SQUIDs) or liquid nitrogen cooling (high temperature SQUIDs). This results in voluminous cryostat casings, and high initial and maintenance costs. Recent multichannel magnetometer systems for MEG or MCG typically combine several hundred SQUID sensors.

Coils and SQUIDs merely provide vectorial measurements of relative changes of the magnetic field. Today, three-axial magnetometers are used in many multichannel

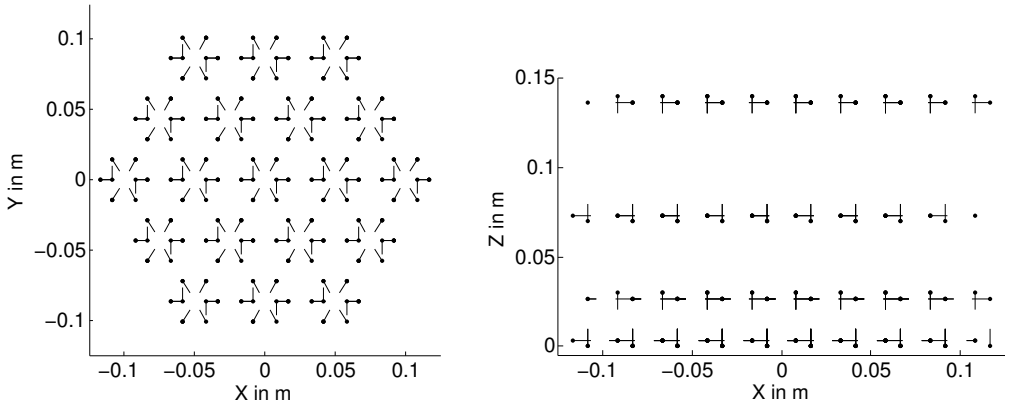

(a) top view of the sensors **(b)** front view

Figure 2.1.: The PTB 304 channel SQUID sensor system. Sensor positions are indicated by dots, directions by small bars.

sensor arrays. Three-axial magnetometer obtain full spatial information of the magnetic field at each sample point by measuring all three orthogonal components.

In section 4.3 and appendix A, we deploy sensor models of the Physikalisch-Technische Bundesanstalt (PTB), Berlin, Germany, 304 channel SQUID system (Schnabel et al. [2004], Figure 2.1) and the Advanced Technologies Biomagnetics (AtB), Pescara, Italy, Argos 200 system with 195 SQUID sensors (Figure 2.2). Both sensor arrays utilize orthogonally oriented magnetic sensors in multiple layers. The pickup area of each sensor is $8\,\text{mm} \times 8\,\text{mm}$. In our simulations, we do not consider specific characteristics of measurement systems, such as the noise sensitivity, the electronic system, or the electromagnetic shielding.

Further sensor technologies applicable for biomedical measurements have been evolved recently. For instance, optically pumped magnetometers, as presented by Bloom [1962], were successfully applied for MCG recordings by Bison et al. [2003]. Such sensors are relatively small and work at room temperature. Therefore, they facilitate multichannel measurements at low costs and enable a higher degree of flexibility for the sensor positions compared with SQUIDs. Further concepts of magnetic sensors are outlined by Ripka [2001].

We model magnetometers as ideal point-like sensors and use identical weights for sensors within one simulation. The sensor weights reflect values for coil area and windings, as they typically apply for SQUID sensor systems. To model MIT systems, coils are approximated by up to several thousands sensor integration points, depending on the coil dimensions and the size of the finite elements. As observed by Vauhkonen [2008], the quantity of coil discretization points seems to have a relatively high influence on the numerical accuracy of finite element computations.

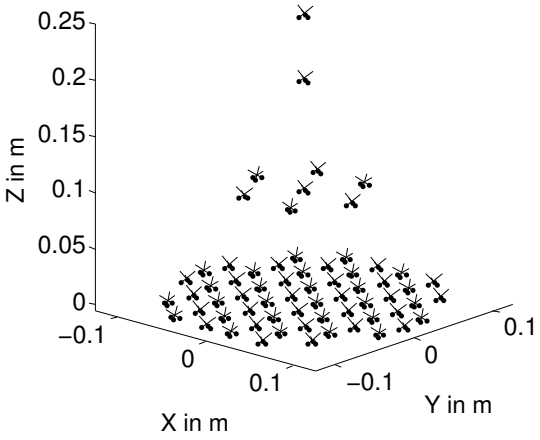

Figure 2.2.: Positions and directions of 195 SQUID sensors of the AtB Argos 200 system.

2.2. Setting up Inverse Problems

2.2.1. Reconstruction of Electromagnetic Sources

The inverse problem we consider consists in the reconstruction of electromagnetic sources based on measured data. In this process, parameters P_i describe the sources, for example by their positions, orientations, and the moments. By solving an inverse problem, the source parameters P_i are estimated from the measurement values B. This inverse problem likewise involves a direct problem, which consists in the computation of sensor values B_f from given source parameters P. To solve the direct problem, appropriate models for sources, sensors, and the propagation of electromagnetic fields between sources and sensors (forward model) are required. The relation between direct and inverse problems are illustrated in Figure 2.3.

Similar to Tarantola [2005, section 1.1], we introduce a *model space* containing all conceivable models that describe together with their parametrization the electromagnetic sources. Furthermore, the *data space* contains all conceivable measurements. We can formalize the solution of the direct problem by introducing a forward operator $\mathcal{F}$ that maps the model space onto the data space with

$$B_f = \mathcal{F}(P) \ . \tag{2.1}$$

The deployed sensor, source, and forward models are implemented by the forward operator $\mathcal{F}$. Since it is generally not possible to obtain its inverse $\mathcal{F}^{-1}$ directly, we formalize the solution of an inverse problem

$$P_i = \arg\min_P \|\mathcal{F}(P) - B\|_2 + \mathcal{M}(P) \ . \tag{2.2}$$

By using *a priori* assumptions $\mathcal{M}$, we can imply constraints that have to or should be fulfilled by P_i. To solve inverse problems as defined in equation (2.2), iterative

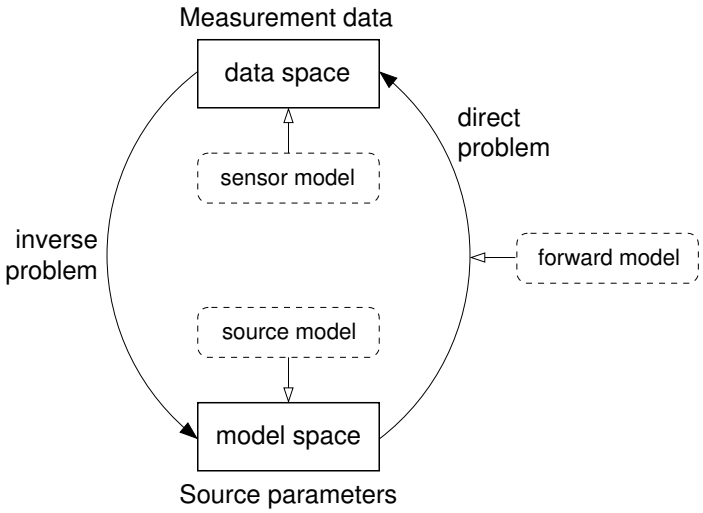

Figure 2.3.: Illustration of the direct and the inverse problem for the reconstruction of electromagnetic sources. The required modelling is indicated by the dashed boxes.

optimization procedures, such as proposed by Nelder and Mead [1965] or as we present in [Eichardt et al. 2008], are typically applied.

The properties of direct and inverse problems differ considerably. The direct problem can be characterized as *well posed*, which implies that the existence, uniqueness and stability of a solution B_f are provided. When having a stable solution, it continuously depends on the input data: Small changes in the input solely lead to small changes in the result. In contrast, the inverse problem is generally *ill-posed*, This implies the non-existence or the non-uniqueness, and the instability of solutions P_i. By involving particular *a priori* assumptions on P_i, we enforce the existence as well as the uniqueness and improve the stability of the solutions. The terminology of well and ill posed problems are attributed to Hadamard [1902], cited, for example by Hawkes [1989, part 1].

2.2.2. Linearization of Inverse Problems

The forward operator $\mathcal{F}$ forms the central element when solving direct and inverse problems. When deploying a dipole-based source model, the domain of $\mathcal{F}$ (model space) is represented by $6n$ parameters that describe the position, orientation, and moment for each of the n sources. Thereby, n needs to be defined in advance. The operator $\mathcal{F}$ depends non-linearly on the parameters for the dipole positions and linearly on the parameters for the orientation and the moment.

To allow a direct inversion of $\mathcal{F}$ and to considerably simplify computations of direct and inverse solutions, $\mathcal{F}$ can be transformed into an linear operator. In electromagnetic applications that focus on the reconstruction of electromagnetic dipolar sources, the linear forward operator is typically denoted as *lead field matrix*

[Hämäläinen and Ilmoniemi 1984, 1994] and denoted by L. In the more general context of numerical analysis, this operator is referred to as *kernel matrix*. Within this thesis, we indicate general kernel matrices by A.

According to the non-linear operator $\mathcal{F}$, the lead field L maps the model space into the data space and comprises information on the sensor, source, and forward models. In this process, L specifies the influence of the activity of sources on the sensors and correspondingly the sensitivity of the sensors to the activity of the sources.

To create L as a linear representation of $\mathcal{F}$, the source space needs to be discretized. Potential locations of sources are predefined, for example by using regular arrangements of dipoles (source space grids) within a volume of interest. Also the directions of the sources are determined in advance. In case that the source directions are *a priori* known, we can use these information directly. To facilitate arbitrary directions of sources, we define at each source position three orthogonally oriented dipoles with uniform moments. Thereby, the total number of sources contained in the model is increased by factor three. After solving the linear inverse problem, the final source orientations and moments can be obtained by the linear combination of the three predefined direction vectors, scaled by their estimated moments.

Each row of $L \in \mathbb{R}^{m \times n}$ corresponds to one of the m sensors and each column represents one of the n source dipoles. Parameters $p \in \mathbb{R}^{n \times 1}$ describe the moments of magnetic or electrical current dipoles for the predefined sources contained in L with respect to their particular positions and directions. We describe the linear direct problem of computing measurement values $b \in \mathbb{R}^{m \times 1}$ from dipole moments p by

$$b = Lp\,. \tag{2.3}$$

For simplicity, we consider in this thesis only single measurements at one point in time. However, an extension to multiple measurements is easily feasible, for example by extending vectors b and p to matrices, in which each column represents one measurement sample in time. In this case, the presented methods are valid likewise or can be adapted easily. We discuss the computation of L in the next section 2.2.3.

According to the linear direct problem in equation (2.3), the linear inverse problem consists in the estimation of the dipole moments p from the measured data b. This inverse problem corresponds to the least square problem of finding optimal source parameters p that explain the measurement data b best. If the number of known measurement values in b exceeds the number of unknown source parameters in p, that is $m > n$, the linear inverse problem is denoted as *overdetermined*. When the quantity of measurement values is smaller than the number of source parameters, that is $m < n$, the linear inverse problem is referred to as *underdetermined*. A synoptic view on standard methods to solve linear inverse problems follows in section 2.3.

2.2.3. Creating the Lead Field Matrix

The element for the sensor with index i and the source with index j of the lead field matrix $L \in \mathbb{R}^{m \times n}$ can be computed by

$$L[i,j] = \sum_{t \in \mathcal{T}_i} w_{it}\, d_i \cdot \mathrm{B}(i,j,t)\,, \tag{2.4}$$

where $t \in \mathcal{T}_i$ is the integration point index for sensor i, w_{it} is the integration point weight, and $d_i \in \mathbb{R}^{3\times 1}$ is the sensor direction, with $\|d_i\|_2 = 1$.

The determination of the magnetic field $B(i,j,t) \in \mathbb{R}^{3\times 1}$ depends on the utilized source, sensor, and forward modelling. A standard methodology in many biomedical application is to model electromagnetic sources by equivalent current dipoles. For forward modelling, quasi-static approximations of Maxwell's equations in conjunction with boundary (BEM) or finite element method (FEM) based models of the conducting volume are typically applied. In these applications, the forward modelling is more specifically denoted as volume conductor modelling.

In applications, such as the inverse estimation of magnetic nanoparticle distributions from remanence measurements or the detection of hidden magnetic objects in the underground, sources can be represented by magnetic dipoles. For these examples, we can assume that magnetic sources are static and that a homogeneous volume conductor with constant magnetic permeability is present. Therefore, the magnetostatic dipole model can be applied to describe the sources and the propagation of magnetic fields.

An overview on the magnetostatic model and applications give Clark and Braginski [2006, section 10.1]. Using this model, we can obtain the magnetic field B that originates from the source with index j at the integration point t of the sensor i by

$$\mathrm{B}(i,j,t) = \frac{\mu_0}{4\,\pi}\left(\frac{3\,e_j \cdot r_{ijt}}{\|r_{ijt}\|_2^5}\, r_{ijt} \;-\; \frac{e_j}{\|r_{ijt}\|_2^3}\right). \tag{2.5}$$

The direction and the magnetic moment of a sources are specified by $e_j \in \mathbb{R}^{3\times 1}$. The displacement vector connecting source j with the integration point t of sensor i is denoted by r_{ijt}. To set up L, we predefine the sources by using uniform moments with $\|e\|_2 = 1$.

When simulating a static magnetic field using equation (2.5), relevant numerical errors might arise in regions with strong gradients, where the magnetic field is supposed to be almost zero. In the studies [Eichardt and Haueisen 2010] and [Eichardt et al. 2010], we compute B using a normalized displacement vector

$$\mathrm{B}(i,j,t) = \frac{\mu_0}{4\,\pi\,\|r_{ijt}\|_2^3}\,\left(3\,[e_j \cdot \tilde{r}_{ijt}]\,\tilde{r}_{ijt} \;-\; e_j\right) \quad \text{with} \quad \tilde{r}_{ijt} = \frac{r_{ijt}}{\|r_{ijt}\|_2} \tag{2.6}$$

that provides a higher numerical stability.

When sensors are modelled as ideal point-like magnetometers, we have for all sensors constantly $t = 1$. Therefore, $\mathrm{B}(i,j,t)$ is simplified to $\mathrm{B}(i,j) := \mathrm{B}(i,j,1)$ and all indices t can be omitted in the equations (2.4), (2.5), and (2.6).

2.2.4. Estimating Conductivity Changes in MIT

The linear inverse problem in MIT consists in estimating complex conductivity changes $\boldsymbol{c} \in \mathbb{C}^{n\times 1}$ from measured secondary voltage differences $\boldsymbol{v} \in \mathbb{R}^{m\times 1}$ between two points in time, with $\boldsymbol{v} := \boldsymbol{v}_1 - \boldsymbol{v}_0$. Secondary voltages are related to secondary magnetic fields that emerge from eddy currents. The kernel matrix $\boldsymbol{J} \in \mathbb{C}^{m\times n}$ of the linear inverse problem in MIT is denoted as Jacobian matrix and is defined by

$$\boldsymbol{J} := \frac{\partial \boldsymbol{v}}{\partial \boldsymbol{c}} \,. \tag{2.7}$$

The Jacobian matrix contains all relevant information on the setup of coils and the electromagnetic modelling.

For electromagnetic computations in MIT, we use the software implementation of Vauhkonen et al. [2007]. Approximations of Maxwell's equations are utilized that consider the frequency for excitation of 10 MHz, the size, and the specific electrical properties of the measurement object. For numerical modelling, the edge finite element method (EFEM) is used. The electromagnetic field is approximated by first-order vector basis functions. Further information and details on the applied models are given by Bíró [1999], Morris et al. [2001], Merwa et al. [2003], and Vauhkonen et al. [2007].

Each nodal element in the EFEM model contains information on the relative permeability, relative permittivity, and electrical conductivity of the measurement object and domain. In our approach, the real parts of $\boldsymbol{c}$ and $\boldsymbol{J}$ are mainly related to changes of electrical conductivities, whereas the complex parts refer to changes of relative permittivities primarily. We denote real parts of $\boldsymbol{c}$, $\boldsymbol{J}$, and $\boldsymbol{v}$ by

$$\begin{aligned} c &:= \mathrm{real}(\boldsymbol{c}) \,, \\ J &:= \mathrm{real}(\boldsymbol{J}) \,, \\ v &:= \mathrm{real}(\boldsymbol{v}) \,. \end{aligned}$$

When solving the linear inverse problem of estimating conductivity changes, we assume that the relative permeability is 1 and that the permittivity is constant. We can formalize the direct problem of mapping conductivity changes to voltage changes by

$$v = Jc \,, \tag{2.8}$$

which results in a linear inverse problem of estimating c from v.

2.3. Solving Linear Inverse Problems

2.3.1. Introduction

In this section, we consider general linear inverse problems of estimating parameters $x \in \mathbb{R}^{n\times 1}$ from observations $y \in \mathbb{R}^{m\times 1}$ using the kernel matrix $A \in \mathbb{R}^{m\times n}$, according

to

$$y = Ax\,. \tag{2.9}$$

The simplest approach to obtain x is to use the Moore-Penrose inverse (pseudo-inverse) A^+ (see appendix B.3) with

$$x = A^+ y\,.$$

Corresponding to Penrose [1955], the Moore-Penrose inverse uniquely exists for all matrices A. Consequently, also the solution x is existent and unique. However, this linear inverse problem is still ill conditioned and solutions are in general not stable. Inevitable noise and errors contained in y affect the solutions x considerably. Therefore, regularization approaches, such as the truncated singular value decomposition (section 2.3.2) or the Tikhonov-Phillips method (section 2.3.3) are often necessary to obtain solutions that are not dominated by the effects of noise and errors.

Furthermore, an explicit computation of the Moore-Penrose inverse should be avoided, since numerical errors and computational costs are higher compared with calculations using implicit representations of the matrix pseudo-inverse. An overview on this matter gives Higham [1996, section 13.1].

2.3.2. Truncated Singular Value Decomposition

A generic tool that can be used to compute the inverse solution of problem (2.9) is the singular value decomposition (SVD) method.

From equation

$$y = Ax = \left(U\Sigma V^T\right) x\,,$$

we can obtain x by

$$x = \left(U\Sigma V^T\right)^+ y = V\Sigma^+ U^T y = \sum_{i=1}^{r} \frac{u_i^T y}{\sigma_i} v_i \tag{2.10}$$

with

$$\Sigma^+ := \operatorname{diag}\left(\sigma_1^{-1}, \ldots, \sigma_r^{-1}, 0, \ldots, 0\right) \in \mathbb{R}^{n\times m}\,. \tag{2.11}$$

According to Golub and Kahan [1965] and Björck [1996, section 1.2.5], this x is the unique solution of the linear inverse problem

$$\min_x \left(\|y - Ax\|_2^2\right)\,, \tag{2.12}$$

which describes the discrepancy the between measured data y and the forward solution Ax with respect to the 2-norm. Details on the SVD are given by Golub and Kahan [1965]; Golub and van Loan [1996] and the appendix B.2.

When solving inverse problems, for instance by using (2.10), large differences of singular values σ_i can lead to considerable amplifications of errors and noise in the inverse solutions. Relatively large σ_i represent major features of the kernel matrix A. Since σ_i^{-1} are then relatively small, the influence of distortions contained in y on the solution x is also low. Proportionally small σ_i represent minor features of A. However, they considerably increase the effects of noise and errors on x, as σ_i^{-1} are large in relation to σ_1^{-1}. Differences in the scale among singular values can be assessed by measuring the condition, which is covered by chapter 3.

By excluding the smallest part of singular values of A from the estimation of x, we apply the truncated singular value decomposition (TSVD) [Hanson 1971]. In this regularization process, an similar linear inverse problem with improved condition is solved.The influence of noise and errors contained in A and y on solutions x can be reduced.

The TSVD solution of the linear inverse problem can be obtained by

$$x = x_k := \sum_{i=1}^{k} \frac{u_i^T y}{\sigma_i} v_i \,. \tag{2.13}$$

The TSVD regularization is controlled by the regularization parameter $k \in \mathbb{N}$, with $1 \leq k \leq r$. Corresponding to [Hansen 1998, sections 4.2 and 5.3], we define filter factors for the by

$$f_i^k := \begin{cases} 1 & i \leq k \\ 0 & i > k \end{cases} . \tag{2.14}$$

An alternative formulation of the TSVD solution x_k using filter factors f^k is given by

$$x_k = \sum_{i=1}^{r} f_i^k \, \frac{u_i^T y}{\sigma_i} v_i \,. \tag{2.15}$$

By applying the TSVD regularization with $k < r$, we effectively improve the condition (see the following section 3.2) of the regularized linear inverse problem. Because singular values smaller than σ_k are not utilized to compute the inverse solution, the condition number of the TSVD regularized linear inverse problem can be defined

$$\kappa_{tsvd}(A, k) := \frac{\sigma_1(A)}{\sigma_k(A)} \,. \tag{2.16}$$

Since $k < r \leq s$ and $\sigma_k \geq \sigma_s$, we obtain for any matrix A and parameter k

$$1 \leq \kappa_{tsvd}(A, k) < \kappa(A) \,. \tag{2.17}$$

2.3.3. Tikhonov-Phillips Regularization

The approach of Tikhonov-Phillips was similarly proposed by Phillips [1962] and Tikhonov [1963], cited by Hansen [1998]. It extends the problem (2.12) by introducing a *model term* to improve the condition and solution stability. The linear inverse problem solved by the Tikhonov-Phillips approach consists in

$$\min_x \Big(\underbrace{\|y - Ax\|_2^2}_{\text{data term}} + \lambda^2 \underbrace{\|Rx\|_2^2}_{\text{model term}} \Big) , \tag{2.18}$$

where $\lambda \in \mathbb{R}$, with $\lambda \geq 0$, is the regularization parameter that weights between the model and the data term. The regularization operator $R \in \mathbb{R}^{n \times n}$ can be designed to achieve smooth solutions x by using second order spatial derivatives [see, for example Messinger-Rapport and Rudy 1988] or, in the simplest case of $R = I$, to privilege solutions with minimum energy $\|x\|_2^2$.

A solution of the minimization problem (2.18) can be obtained [see, for example Golub et al. 1999] by

$$x = x_\lambda := \left(A^T A + \lambda^2 R^T R \right)^{-1} A^T y \, . \tag{2.19}$$

For the standard form of (2.18) with $R = I$, the equation (2.19) can be simplified to

$$x_\lambda = \left(A^T \, A + \lambda^2 I^{n \times n} \right)^{-1} A^T y \, . \tag{2.20}$$

For underdetermined linear inverse problem with $R = I$, solutions x_λ are computed more efficiently by

$$x_\lambda = A^T \, \left(A A^T + \lambda^2 I^{m \times m} \right)^{-1} y \, . \tag{2.21}$$

To express the standard form of the Tikhonov-Phillips regularization by filter factors and the SVD components, we define f^λ corresponding to Hansen [1998, section 5.1.1] by

$$f_i^\lambda := \frac{\sigma_i^2}{\sigma_i^2 + \lambda^2} \, . \tag{2.22}$$

With f^λ we can obtain x_λ by

$$x_\lambda = \sum_{i=1}^{r} f_i^\lambda \, \frac{u_i^T y}{\sigma_i} v_i \, . \tag{2.23}$$

When applying the TSVD and Tikhonov-Phillips methods with $\lambda \approx \sigma_k$, similar inverse solutions with $x_k \approx x_\lambda$ are often obtained. In general, the matrix inverse in equations (2.19) – (2.21) should not be computed explicitly. In MathWorks® MATLAB, the `mldivide` operation is typically applied.

2.3.4. Choice of Regularization Parameters

The choice of regularization parameters, which are k for TSVD and λ for Tikhonov-Phillips, has essential influences on the quality of inverse solutions x. If an inverse problem is insufficiently regularized, that is, we use too high values of k or too small values of λ, then x is dominated by effects of errors and noise. On the other hand, an excessive regularization leads to a poor explanation of the measurement data y and to results, which are overly biased by the applied regularization model. An optimal determination of regularization parameters is in practice often a difficult issue.

Two frequently used methods, which determine regularization parameters automatically, are the generalized cross validation (GCV) method introduced by Wahba [1977] and the L-curve of Hansen [1992]. GCV provides the regularization parameter that minimizes the weighted mean square of the data prediction error, which is specified in equation (1.4) of [Wahba 1977]. Noise and errors are assumed to be uncorrelated with zero mean and common, possibly unknown variance.

By applying the L-curve, we select the regularization parameter α that sufficiently minimizes the residual

$$\|Ax_\alpha - y\|_2 \tag{2.24}$$

and the model term

$$\|Rx_\alpha\|_2 \,. \tag{2.25}$$

For TSVD, we use $R = I$ in the model term. The vector x_α is the inverse solution obtained with regularization parameter α. The plot of the quantity (2.25) against (2.24) in log-log scale often exhibits an L-shaped curve. The particular α representing the corner of the L-curve with maximum curvature is considered as optimal. An overview on these and further approaches to set regularization parameters provide Hansen [1998, chapter 7] and Vogel [2002, chapter 7]. In certain cases, GCV and L-curve do not result in proper values for α. This occurs when the prediction error exhibits no minimum, the L-curve has no adequate L-shape, or the corner of the L-curve can not be detected correctly.

Alternatively, we can also chose regularization parameters empirically. One possibility to set k in case of the TSVD is

$$k = \lceil \beta\, r \rceil \,, \tag{2.26}$$

where $r = \operatorname{rank}(A)$; β is manually chosen based on previous solutions or tests, with $0 < \beta \leq 1$. From this k, we can choose λ for the standard form of the Tikhonov-Phillips approach by

$$\lambda = \sigma_k \,.$$

This empiric approach does not consider any optimality criterion. However, it often results in acceptable solutions when the linear inverse problem, its condition, and the characteristics of noise and errors are varying only inconsiderably for different representations of the measurement data.

2.3.5. Weighted and Sparse Solutions

The TSVD and Tikhonov-Phillips (with $R = I$) methods privilege solutions with minimum norm $\|x\|_2$. This results in a minimum energy bias of the solutions x, which appear smooth and non-focal. This bias is particularly critical when the distances between the positions of the sources and sensors differ considerably and when the source space is only partly framed by sensors. Owing to the minimum 2-norm bias, the estimated activity of sources is often too closely located at the sensors.

To reduce the localization bias for distant sources, we can use a specific source weighting matrix R to adapt the linear inverse problem in equation (2.19), as presented for instance by Köhler et al. [1996]. Furthermore, we can normalize the kernel matrix A prior to the inversion process by left multiplication with a matrix $N \in \mathbb{R}^{n\times n}$. The linear inverse solution using the parameter α for regularization and the matrix N for normalization can be obtained by

$$x = N(NA)^{+}_{\alpha} y\,.$$

When defining N [see, for example Phillips et al. 1997] by

$$N := \operatorname{diag}\left(\|A[\sim,1]\|_2^{-1},\ \ldots,\ \|A[\sim,n]\|_2^{-1}\right)\,,$$

where $A[\sim,i]$ represents the ith column of A, we obtain for all columns of the matrix product NA identical sensitivity values corresponding to the definitions in section 3.6. However, the weighting of distant sources can result in considerable disturbances in x when the measurement data are affected by higher levels of noise. Furthermore, the regularization and determination of regularization parameters have more pronounced effects on x compared with uncompensated solutions.

To facilitate sparse solutions x with only a few elements unequal zero the 1-norm in the model term can be utilized [Tsaig and Donoho 2006]. The resulting inverse problem consists in minimizing the expression

$$\min_x \left(\|b - Ax\|_2^2 + \lambda^2 \|Rx\|_1^2\right)\,. \tag{2.27}$$

Owing to the 1-norm, problem (2.27) is not linear and requires iterative solvers. Various algorithms exist to obtain sparse solutions. Basic approaches were proposed for example by Gorodnitsky et al. [1995], Natarajan [1995], and Daubechies et al. [2008]. As reported by Gorodnitsky et al. [1995], recursively weighted 1-norm solutions provide higher spatial accuracies for deep sources than weighted solutions with minimum 2-norm.

3 Assessing Condition and Sensitivity

3.1. Overview

Linear inverse problems can be characterized by assessing the properties of the respective kernel matrix. The main part of this chapter focusses on the evaluation of the matrix condition using the condition number with respect to the 2-norm and the ratio between largest and mean singular value. By evaluating the condition, we can quantify the potential amplification of noise and errors in the measurement data on the linear inverse solution. Moreover, we present approaches to quantify the sensitivity of measurement systems to conductivity changes and to activities of electromagnetic sources.

3.2. Condition and the Condition Number

A frequently used measure of condition is the condition number κ_p relative to the p-norm. The condition number as a measure for rounding-off errors was first applied by Turing [1948].

For square matrices A, $\kappa_p(A)$ is defined by

$$\kappa_p(A) := \|A\|_p \, \|A^{-1}\|_p \tag{3.1}$$

with $\kappa_p(A) := \infty$, if A is singular [Golub and van Loan 1996, section 2.7.2].

Kernel matrices related to linear inverse problems in magnetic applications are in general not square. To analyse the condition of a rectangular matrix A, we apply corresponding Zielke [1988] the Moore-Penrose inverse A^+ to compute κ_p with

$$\kappa_p(A) := \|A\|_p \, \|A^+\|_p \,, \tag{3.2}$$

and $\kappa_p(A) := \infty$, if A is rank-deficient. For square A, the definitions (3.1) and (3.2) are equivalent. The condition number of $A \in \mathbb{R}^{m \times n}$ with respect to the 2-norm follows from (3.2) with

$$\kappa(A) := \kappa_2(A) = \frac{\sigma_1(A)}{\sigma_s(A)} \,, \tag{3.3}$$

where σ_1 is the largest and σ_s the smallest singular value including 0. The index s denotes the total number of singular values with

$$s := \min(m, n)\,. \tag{3.4}$$

Similar to Higham [1995], we define the condition of the linear inverse problem

$$y = Ax\,, \tag{3.5}$$

with $A \in \mathbb{R}^{m\times n}$, by

$$\kappa_p(A, y) := \kappa_p(A) + \frac{\|A^+\|_p \, \|y\|_p}{\|A^+ y\|_p}\,. \tag{3.6}$$

The inequality

$$\|A\|_p \geq \frac{\|y\|_p}{\|x\|_p}, \tag{3.7}$$

follows from the definition (3.5) and from the property $\|Ax\|_p \leq \|A\|_p \, \|x\|_p$ [Golub and van Loan 1996, inequality (2.3.3)]. Using $\|A^+ y\|_p = \|x\|_p$, the inequality (3.7), and the definitions (3.2) and (3.6), we obtain analogue to Higham [1995]

$$\kappa_p(A) \leq \kappa_p(A, y) \leq 2\,\kappa_p(A)\,. \tag{3.8}$$

With this limitation, the matrix condition number $\kappa_p(A)$ is an adequate measure for the condition $\kappa_p(A, y)$ of a related linear inverse problem, too.

By κ_p and κ we denote the condition numbers with respect to the p-norm and the 2-norm for any $A \in \mathbb{R}^{m\times n}$. The following properties apply to κ_p [Hogben 2007, section 37.5]

$$\begin{aligned}
&\kappa_p \geq 1\,,\\
&\forall l \in \mathbb{R}^\star\colon\ \kappa_p(l\,A) = \kappa_p(A)\,,\\
&\kappa_p(W A) \ \leq\ \kappa_p(W)\,\kappa_p(A)\,,\\
&\forall p, q \in \{1, 2, F, \infty\}\colon\ \exists\, l_1, l_2 \in \mathbb{R}^+\colon\ l_1\,\kappa_p(A) \ \leq\ \kappa_q(A) \ \leq\ l_2\,\kappa_p(A)\,,\\
&\kappa(A) = 1 \iff \exists\, l \in \mathbb{R}^\star\colon\ A^T A = l\,I \ \vee\ A A^T = l\,I\,,\\
&\kappa(A) = \infty \iff \operatorname{rank}(A) < s\,,\\
&\kappa(A) = \kappa(A^+) = \kappa(A^T)\,.
\end{aligned} \tag{3.9}$$

Specific values for the constants l_1 and l_2 in inequality (3.9), depending on p and q, are given by Zielke [1988]. Further properties of the SVD and matrix norms are provided in appendices B.2 and B.4.

For square matrices, κ^{-1} is a measure for the normwise [Demmel 1987], [Stewart and Sun 1990, theorem III.2.8], [Demmel 1997, theorem 2.1] and the componentwise distance [Rump 1999] to the nearest singular matrix. For rectangular matrices, κ^{-1}

proportionally measures the normwise distance to the nearest rank-deficient matrix [Demko 1986].

Furthermore, $\kappa(A)$ quantifies the sensitivity of A^{-1} to changes in A [Stewart and Sun 1990, page 119f]. Referring to linear inverse problems, κ denotes likewise the sensitivity of the output to changes in the input. Such changes in the input are not solely related to the measurement signal. The input data are constantly effected by measurement noise and numerical errors. Demmel [1988] applies the condition number as a general measure of difficulty for problems in numerical analysis.

As κ can also be considered as a measure of row dependency, Di Rienzo et al. [2005] use κ as a rough indicator for the information content of a kernel matrix. They apply κ to compare sensor arrangements of mono-axial and three-axial magnetometers. The condition number was further used by Rouve et al. [2006] to identify optimal arrangements of magnetic sensors.

3.3. Computing Singular Values and the Condition Number

To compute singular values and vectors, software packages often revert to efficient LAPACK implementations. A documentation on LAPACK is available from Anderson et al. [1999]. To compute singular values and κ, we use with the exception of section 4.2 the SVD algorithm of MathWorks® MATLAB. For the decomposition of real matrices in double precision, MATLAB 2010a deploys the QR-based LAPACK DGESVD routine.

DGESVD results in deviations of computed singular values $\hat{\sigma}_i$ from true values σ_i, bounded by [Anderson et al. 1999, section 4.9.1]

$$|\hat{\sigma}_i - \sigma_i| \leq \epsilon\, \sigma_1\,, \tag{3.10}$$

in which $\epsilon \approx 2.2 \times 10^{-16}$ is the relative floating-point accuracy of the 64 bit systems we deployed for the computations. Consequently, a high relative accuracy in $\hat{\sigma}_i$ is only ensured for singular values close to σ_1. For particularly small values σ_i, we have to anticipate significant numerical errors. To compute κ, we divide corresponding the definition (3.3) by the smallest singular value σ_s, which is a numerically instable operation, too [see, for example Hermann 2001, chapter 1.2].

Considering the definition of the condition number in (3.3), the accuracy of κ crucially depends on the smallest singular value σ_s. Using the inequality (3.10), we obtain for the relative error of σ_s

$$\frac{|\hat{\sigma}_s - \sigma_s|}{\sigma_s} \leq \frac{\epsilon\, \sigma_1}{\sigma_s} = \epsilon\, \kappa\,. \tag{3.11}$$

Consequently, values of κ with $\kappa \geq \epsilon^{-1}$ are potentially inaccurate even in the order of magnitude. Demmel [1987] and Higham [1995] state that the condition number of computing the condition number is the condition number.

For special classes of matrices it is possible to compute all, even tiny singular values with high relative accuracy. For instance, special methods for the rank-revealing decomposition with a subsequent SVD provide high relative accuracies of singular values for *graded*, *totally positive*, and *Cauchy* matrices. An overview on this topic give Demmel et al. [1999]. However, this is in general not possible for all matrices and the costs of computing the SVD can increase significantly. As noted by Demmel et al. [1999, page 27], the DGESVD is to date the most accurate LAPACK routine for the SVD of general dense matrices, such as the kernel matrices of linear inverse problems, which we are considering.

3.4. Ratio of Largest and Mean Singular Value as Measure of Condition

To assess the condition of a matrix A, we introduce the measure ρ that quantifies the ratio between largest and mean singular value of A. We define ρ by part 1 of

$$\rho(A) \overset{1}{:=} \frac{\sigma_1(A)}{\frac{1}{n}\sum_{i=1}^{n}\sigma_i(A)} \overset{2}{=} \frac{n\,\sigma_1(A)}{\sum_{i=1}^{n}\sigma_i(A)} \overset{3}{=} \left(\frac{1}{n}\sum_{i=1}^{n}\frac{\sigma_i(A)}{\sigma_1(A)}\right)^{-1}, \tag{3.12}$$

with $\rho(A) := \infty$, if $A = 0$. Part 1 of the definition (3.12) is equivalent to the ratio of n-times the largest singular value divided by the sum of singular values (part 2). Corresponding to part 3 of (3.12), ρ is a measure for the average decay of singular values of A, too.

A visual evaluation of the decay of singular values has been used before by Nalbach and Dössel [2002] to compare the information content of MCG and ECG (electrocardiography) sensor arrangements. Moreover, Engl et al. [1996, section 2.2] use this decay to quantify the degree of ill-posedness[1] of a linear inverse problem.

We use ρ as a qualitative measure of the matrix condition. However, it does not directly reflect the distance to singularity or to a matrix of smaller rank. In particular, ρ is an appropriate surrogate for κ when effects of numerical inaccuracies that occur during the computation of κ should be avoided or when values of κ may exceed the inverse of the relative floating point accuracy (refer previous section 3.3).

From the definition (3.12), we can conclude the following properties of ρ

$$\begin{aligned}
&\rho(A) \geq 1\,,\\
&\forall l \in \mathbb{R}^{\star}\colon\ \rho(l\,A) = \rho(A)\,,\\
&\rho(A) = 1 \iff \exists\, l \in \mathbb{R}^{\star}\colon\ A^T A = l\,I \ \vee\ A A^T = l\,I\,,\\
&\rho(A) = \rho\left(A^T\right)\,.
\end{aligned}$$

[1] In the framework of this thesis, the terminology *measure of condition* is more appropriate than *measure of ill-posedness*. We term corresponding to section 2.2.1 a problem as ill posed, if solutions show numerical instabilities and if they may not exist or be unique. Ill-conditioned linear inverse problems lead to instable solutions.

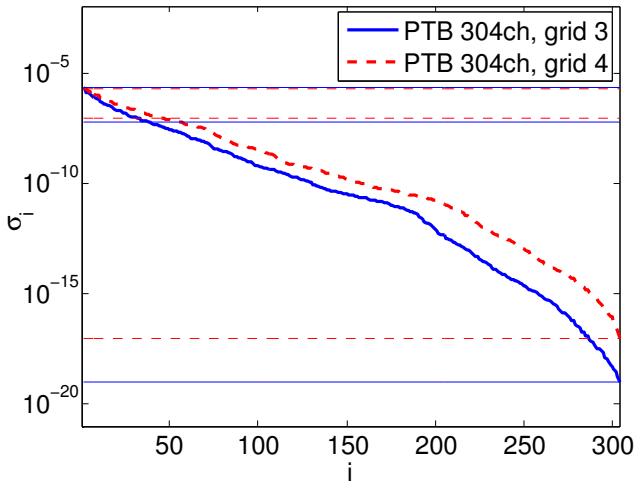

Figure 3.1.: Semi-logarithmic plot of the singular values of two kernel matrices that incorporate the PTB 304 channel SQUID sensor system and the source grids 3 (blue solid lines) and 4 (red dashed lines) of the following section 4.3.2. The largest, mean, and smallest singular values are indicated by thin horizontal lines.

Figure 3.1 shows as an example the semi-logarithmic plot of the singular values of two lead field matrices related to linear inverse problems in magnetostatic applications. The decay to zero without particular gaps and the roughly exponential slope are characteristic for the distribution of the singular values in such applications. The horizontal lines in Figure 3.1 indicate the largest, mean, and smallest singular values, which represent the basis for the determination of κ and ρ.

3.5. Comparing the Condition for Different Sensor Arrays

To reasonably compare the condition of linear inverse problems for different sensor arrays by means of κ or ρ, the kernel matrices have to involve identical definitions of the source space and exhibit identical numbers of singular values. Consequently, the linear inverse problem is required to be overdetermined with fewer sources than sensors or in case of underdetermined linear inverse problems the sensor arrays have to deploy equal numbers of sensors.

In contrast, Figure 3.2 illustrates that comparing sensor arrays with different numbers of sensors by κ and ρ is in general not meaningful for underdetermined linear inverse problems. The PTB 304 channel sensor array provides higher and, therefore, worse values of κ and ρ compared with its subset of the 114 lowest sensors. To reduce the effects of noise and errors to solutions of linear inverse problems, regularization methods are applied to improve the condition. In case of the TSVD

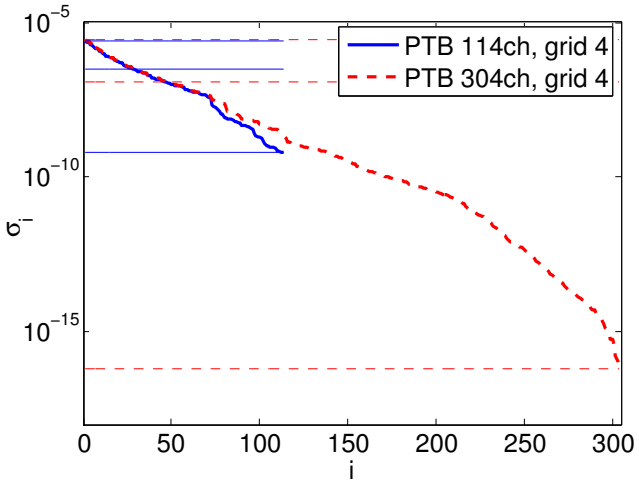

Figure 3.2.: Semi-logarithmic plot of singular values of two lead field matrices, both using the source grid 4 with 3025 sources of the following section 4.3.2. One example kernel matrix uses the PTB 304 channel sensor system including all sensors (red dashed lines). The second kernel matrix implies the subset of the lowest 114 SQUID sensors (blue lines). The largest, mean, and smallest singular values are indicated by thin horizontal lines.

method (see section 2.3), the particular singular value related to the truncation threshold k determines together with the largest singular value the condition of the regularized linear inverse problem. Since the singular values 2–114 are larger for the 304 channel configuration and because the largest singular values are almost identical, the use of the 304 channel setup leads in practice to a better condition of the regularized linear inverse problem and to more stable solutions.

To enable specific comparisons of sensor arrays with different numbers of sensors, we can evaluate the condition relative to the kth singular value. We define κ and ρ relative to the kth singular value of the kernel matrix, with $1 \leq k \leq \operatorname{rank}(A)$, by

$$\kappa^k(A) := \frac{\sigma_1(A)}{\sigma_k(A)} \tag{3.13}$$

and

$$\rho^k(A) := \frac{\sigma_1(A)}{\frac{1}{k}\sum_{i=1}^{k}\sigma_i(A)}\,. \tag{3.14}$$

Besides measuring the condition, further criteria to assess and compare sensor arrangements with respect to linear inverse problems were proposed. Di Rienzo and Haueisen [2007] used the projection method to compare mono-axial with three-axial magnetometer arrays in the application of MCG. Furthermore, Di Rienzo and Haueisen [2006] defined lower error bounds of TSVD solutions to assess the performance of sensor arrangements. Curtis et al. [2004] determined average angles

between the rows of the kernel matrix, which represent the receivers of a measurement device, to quantify the the dependency in n-dimensional space. Davide et al. [1993] deployed the sensitivity and resolution of a non-linear forward operator for the evaluation of sensor arrays.

3.6. Sensitivity Analysis

By analysing the sensitivity of a lead field matrix $L \in \mathbb{R}^{m \times n}$, we are able to measure the influence of electromagnetic dipoles at particular source positions on the measurement system. We define the sensitivity of a magnetic sensor array relative to the source with index i by

$$S_i^L := \sum_{j=1}^{m} |L[j,i]| \ . \tag{3.15}$$

In case that each source position i comprises three orthogonally directed dipoles with row indices $x(i)$, $y(i)$, and $z(i)$, we extend the definition (3.15) to

$$S_i^{L^3} := S_{x(i)}^L + S_{y(i)}^L + S_{z(i)}^L \tag{3.16}$$

to quantify the total sensitivity. In section 4.3, we evaluate the sensitivity of lead field matrices to sources that are represented by point-like magnetostatic dipoles. In this application, S^L and S^{L^3} solely depend on the sensor array, the source positions, and the source directions. Units of S^L and S^{L^3} are in $\mathrm{TA}^{-1}\mathrm{m}^{-2}$ (magnetometer arrays, magnetic sources), $\mathrm{TA}^{-1}\mathrm{m}^{-3}$ (arrays of first-order gradiometers, magnetic sources), $\mathrm{TA}^{-1}\mathrm{m}^{-1}$ (magnetometers, electrical sources), and $\mathrm{TA}^{-1}\mathrm{m}^{-2}$ (first-order gradiometers, electrical sources), respectively.

Similarly, we define for MIT coil setups the sensitivity to changes of the electrical conductivity in a volume element i by considering the Jacobian matrix J with

$$S_i^J := \sum_{j=1}^{m} |J[j,i]| \ . \tag{3.17}$$

The inherent dependency of S^J on the volumes of finite elements has to be considered when evaluating the sensitivity in MIT. The quantities of S^J are given in units of VmS^{-1}.

To obtain scalar measures for the sensitivity, we use in section 4.5 the median of S^J. Other formulations of the sensitivity were presented by Soleimani [2005], Soleimani et al. [2006], and Pham and Peyton [2008].

4 Improving Sensor and Source Configurations

4.1. Overview

This chapter focusses on improving the condition of linear inverse problems and on evaluating the sensitivity in magnetic applications.

In section 4.2, we optimize sensor positions and directions for the application of MCG. A newly developed tabu search algorithm is applied to find sensor arrangements that result in lead field matrices with a minimum condition number. The presented work is based on the publication [Lau et al. 2008b].

The objective of section 4.3 is to identify source grid parameters that provide an improved condition of the magnetostatic linear inverse problem in magnetic nanoparticle imaging. Thereby, we use ρ to measure the condition, as ρ provides a higher numerical stability than κ. This part of the thesis is based on the publications [Eichardt et al. 2010] and [Eichardt et al. Submitted].

In section 4.4, we investigate the influence of random variations in the sensor directions on the condition. We show that the condition number κ can be considerably reduced when the sensors directions are randomly varying compared with uniform directions toward -Z. The original work on this topic was published in [Eichardt and Haueisen 2009] and in [Eichardt and Haueisen 2010].

The fourth section of this chapter, 4.5, addresses the linear inverse problem in MIT. By simulations we evaluate and compare the sensitivity and condition for exemplary arrangements of measurements and excitation coils. This section is essentially based on the work published in [Eichardt et al. 2009b], which focusses on the sensitivity comparison for MIT systems in the application of stroke classification. In this thesis, however, we use a more general volume of interest. Therefore, the methods, results, and conclusions in this thesis differ slightly from the previous publication.

4.2. Optimization of Sensors Arrangements

4.2.1. Introduction

The question of how to optimally arrange sensors arises in many applications, in particular, if the number of sensors is limited by technical restrictions, the sensors and the measurement equipment are expensive, and if sensors can be placed in a spacious region without considerable limitations.

In this section, we present a general approach to optimize sensor configurations with respect to linear inverse problems. As an exemplary application, we focus on the optimization of the sensors positions and directions for MCG.

4.2.2. Principles of Tabu Search

Optimization Scheme

We address the optimization of the sensor positions and directions with respect to the condition number κ of the lead field matrix L.

To optimize the arrangement of sensors, a lead field L incorporating the definition of the source space and all possible sensor positions and directions is created first. In this process, the source space contains a configuration of sources that cover the considered application representatively. The row i of $L \in \mathbb{R}^{m \times n}$, with $1 \leq i \leq m$, describes the influence of the n defined sources on the sensor i. If the sensors are not subject to structural dependencies, the rows of L can be handled individually. For example, such dependencies typically arise when three-axial magnetometers are modelled by three mono-axial sensors.

Within the process of optimization, we improve the condition by identifying the subset of rows of L, which provides the minimum condition number κ for a predefined number of sensors. A similar approach that uses a sequential selection algorithm was presented by Lux et al. [1978] to reduce the number of leads in body surface potential maps.

Tabu Search Algorithm

To find an optimal set of sensors, we utilize the heuristic *tabu search* optimization procedure, presented by Glover [1990] and Glover and Laguna [1997]. When looking for an optimal subset of w from m sensors with minimum condition number κ, the search space is represented by

$$\binom{m}{w} = \frac{m!}{w!\,(m-w)!} \tag{4.1}$$

possible combinations of sensors, if the selection is not restricted by constraints.

The proposed tabu search strategy we use to optimize the arrangement of sensors is illustrated by Algorithm 1. The input of the algorithm mainly consists of the

Algorithm 1 Tabu search algorithm to find w sensors that minimize κ.

Require: $L \in \mathbb{R}^{m \times n} \wedge 1 \leq w < m \wedge MaxIter > 1 \wedge NumNeighbours \geq 1$
Ensure: $W^* \subset W$ with $|W^*| = w \wedge \forall W' \in TabuList\colon \kappa(\, L[W^*, \sim]\,) \leq \kappa(\, L[W', \sim]\,)$

```
W ← {1, ..., m}    /* indices of sensors */
W* ← CreateRandomSubset(W, w)    /* with W* ⊂ W ∧ |W*| = w */
κ* ← κ( L[W*, ∼] )    /* condition number as the optimization criterion */
TabuList ← { W* }    /* insert W* into tabu list */
for Iter = 1 to MaxIter do
  NumExchange ← SetExchangeNumber(Iter, MaxIter, w)
  for i = 1 to NumNeighbours do
    W' ← ExchangeSensors(W \ W*, W*, NumExchange)
    if W' ∉ TabuList then
      κ' ← κ( L[W', ∼] )    /* condition number of new arrangement */
      if κ' ≤ κ* then
        W* ← W'    /* update optimum */
        κ* ← κ'
      end if
      TabuList ← TabuList ∪ { W' }    /* do not evaluate this W' again */
    end if
  end for
end for
```

lead field $L \in \mathbb{R}^{m \times n}$, which contains the information on all m possible sensors, and the number of sensors to select, w. Further input parameters specify the number of iterations ($MaxIter$) and the quantity of new neighbouring solutions created in each of the iterations ($NumNeighbours$). The tabu search algorithm returns a set of sensor indices W^*, with $|W^*| = w$, providing the minimum condition number $\kappa^* = \kappa(\, L[W^*, \sim]\,)$. The matrix $L[W^*, \sim]$ denotes the lead field derived from the input L that comprises only the rows with sensor indices in W^*.

Besides the limitation of iterations by $MaxIter$, we do not apply more sophisticated break criteria, such as an evaluation of the optimization progress. New solutions of the optimization problem are generated by the ExchangeSensors() function. In each iteration, $NumNeighbours$ new candidate solutions W' are created from the current optimum set of sensor indices W^* by exchanging $NumExchange$ elements between W^* and $W \setminus W^*$. The variable $NumExchange$ is automatically set, depending on the current iteration number, $MaxIter$, and w. The tabu search typically starts with relatively large values of $NumExchange$ to enable a globally oriented search. During the process of optimization, this parameter is gradually decreased to improve the local search ability. The ExchangeSensors() function and the initial lead field L are designed such that violations of optimization constraints are fully avoided. In particular, L contains only sensors that comply with the minimum distance criterion and ExchangeSensors() does not select sensors with different directions at identical positions. Therefore, the expensive clearance of conflicts is not required. By default,

we do not apply practically relevant limitations to the size of the tabu list. However, it is easily possible to set such a limit and to remove outdated list elements.

Notes on the Implementation

We implemented the tabu search algorithm in ANSI C++ using the GNU compiler collection. Algorithms and data containers from the standard template library (STL) were used as algorithmic foundations. The text book of Josuttis [1999] gives an extensive overview on the STL in C++ .

To quantify upper bounds in terms of f for the complexity and the computational costs g of an operation, we use corresponding Knuth [1976] the O-notation with

$$g(x) \in O(f(x)) \iff \exists c, x_0 \colon \forall x > x_0 \colon |g(x)| \leq c\, f(x)\,. \tag{4.2}$$

The variable x specifies the dimension of the input data, such as the number of elements or the matrix size. For instance, we term costs g as polynomial, if

$$g(x) \in O(f(x)) \quad \text{where} \quad f(x) = x^a$$

and a is constant, or shorter, if

$$g(x) \in O(x^a)\,.$$

To enable a simple notation, we use in the pseudocode of Algorithm 1 sets or families of sets as containers. For the efficient data handling, the C++ implementation operates with vectors and maps (balanced trees) instead. The sensor indices W, W^*, and W' are represented by `vector<unsigned int>` containers. Sensor indices are inserted into W at the beginning of the optimization procedure. The randomized exchange of used and unused sensors indices is accomplished by the `random_shuffle`, `swap_ranges`, and `sort` methods. The computational costs of creating a new configuration of sensors W' can be quantified with $O(m + w \log w)$, where m is the total number and w the number of used sensors.

To store already evaluated candidate solutions W' in the tabu list efficiently, we utilize the `map` container by introducing a $<$-relation for vectors of sensor indices. The STL maps are implemented as balanced red-black trees, which provide logarithmic complexities for all elementary operations. Consequently, the location, insertion, and deletion of sensor configurations within the tabu list result in computational costs of $O(\log x)$, where x is the number of elements contained in the $TabuList$ map.

The most expensive operation in Algorithm 1 is the computation of the optimization criterion κ for a lead field submatrix of a given sensor configuration W'. These costs are dominated by the complexity of the SVD. The SVD results in costs of $O(wn^2)$ for a matrix $L[W', \sim] \in \mathbb{R}^{w \times n}$, in which without loss of generality w is greater or equal n (otherwise, we transpose L and the SVD result).

In conclusion, the computational costs of tabu search for optimizing an array with w of m sensors in $MaxIter$ iterations is asymptotically bounded by

$$O(MaxIter\,(m + w \log w + \log x) + x\, wn^2)\,, \tag{4.3}$$

where n specifies the number of considered sources and x is the maximum number of solutions in the tabu list.

4.2.3. Sensor Optimization in Magnetocardiography

Introduction

The proposed tabu search algorithm is applied for the optimization of sensor arrangements in MCG. Newly emerging sensor technologies, such as optically pumped magnetometers, work at room temperature and facilitate less restrictive arrangements of sensors. Furthermore, we compare the performances of the tabu search algorithm with a quasi-continuous particle swarm optimizer (PSO). Stephan Lau developed this version of PSO and carried out the simulations for our joint publication [Lau et al. 2008b]. I thank him for supplying simulation data and results, presented in this section of my thesis.

Methods

We optimize sensor arrangements in a 20 cm × 20 cm sensor plane in front of the human chest. The search space for the tabu search optimization is represented by 11×11 potential sensor positions, in combination with 26 possible directions. The compliance with the minimum sensor distance constraint of 2 cm is implicitly satisfied by using any of these sensor positions. To search globally and locally, we linearly reduce the number of sensors to be exchanged from $w/2$ to 1 over the first 2/3 of iterations.

Although PSO is able to search in continuous space, a discretization of 2.5 mm in X/Y direction is applied to reduce the computational costs of generating the lead field matrices. This results in 85×85 possible sensor positions, combined with 62 possible sensor directions. The computational costs of tabu search and PSO are limited to produce a maximum of 10^6 candidate solutions. For the optimization of sensor arrangements, we consider arrays with $w = 13$ to 99 sensors. For both optimizers, the best results out of ten runs are presented.

The source space model comprises 13 current dipoles, distributed around the left ventricle of the heart with the positions $\{apex\} \cup \{antero,\ latero,\ septo,\ infero\} \times \{apical,\ medial,\ basal\}$. The volume conductor model is based on the magnetic resonance imaging data from a healthy volunteer and on quasi-static formulations of the Maxwell equations. To model the propagation of the electromagnetic field, we use the boundary element method with linear approximations. The compartments are represented by the surfaces of the lungs and the torso with transitions of the conductivity corresponding Geddes and Baker [1967] from 0.04 to $0.2\,\mathrm{Sm}^{-1}$.

The data for the volume conductor and the source model were previously created by Haueisen et al. [2002] and used by Di Rienzo et al. [2005]. The minimum distance between the torso surface and the sensor plane is 2.7 cm. Lead field matrices that contain all possible sensor positions and directions are created with the SimBio [2011]

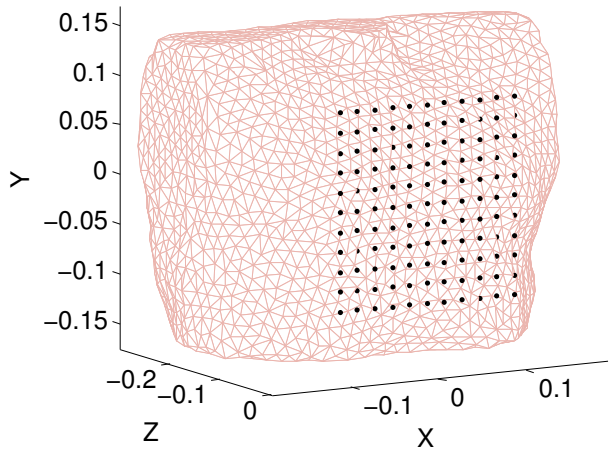

Figure 4.1.: Plane of the 11×11 possible sensors positions ($\bullet$) and the surface of the torso volume.

toolbox. Figure 4.1 illustrates the possible sensor positions in front of the torso surface.

Results

The condition number κ of the optimized sensor arrangements using tabu search and PSO are presented in Figure 4.2a for sensors numbers w between 13 and 99. The condition numbers for regular, not optimized sensor arrangements lie between 765 and 1318. By optimizing the sensor positions and directions with tabu search, κ is reduced to values between 103 and 203. A small growth of κ for increasing numbers of sensors can be observed. The optimized condition numbers using tabu search are in our simulations slightly lower compared with PSO. Also the increase of κ for increasing numbers of sensors is less pronounced for tabu search than for PSO. One example of an arrangement with 41 sensors optimized with tabu search is shown in Figure 4.2b. The sensors are preferably positioned in regions with strong gradients of the magnetic field. The distribution of sensors clearly deviates from a regular arrangement.

4.2.4. Discussion

For the application of MCG, the condition number κ can be considerably reduced by optimizing the arrangements of sensors. In our study, tabu search produces slightly better results than the quasi-continous PSO method, which uses finer discretizations of sensor positions and directions. The benefits of tabu search regarding PSO can be explained by the combinatorial optimization, which avoids constrained solutions and redundant determinations of the objective function values.

Furthermore, the number of combinatorially possible sensor arrangements corresponding equation (4.1) is in the majority of practical applications considerably

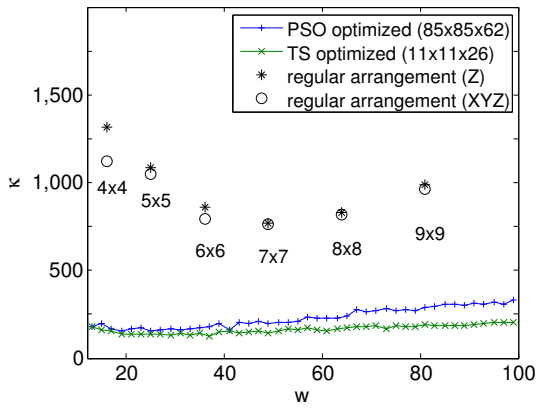

(a) Results of κ for optimized arrangements of w sensors when using tabu search (TS) and PSO. The values of κ for regularly arranged sensor positions and directions are given for comparison.

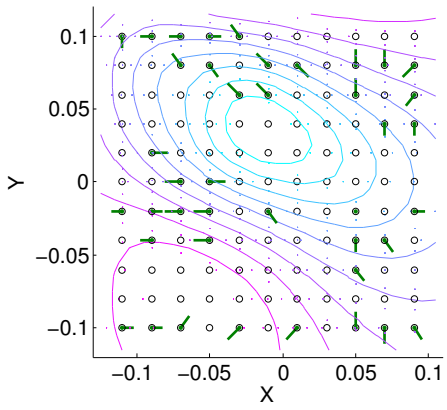

(b) Example result of the tabu search optimization for 41 sensors. The resulting positions and directions are indicated by green bars and spare positions by ∘. The simulated magnetic field of the 13 dipoles is indicated by the contour lines.

Figure 4.2.: Results of the tabu search showing the optimized positions and directions of the sensors.

smaller than the search space of quasi-continuous optimizers. This search space consists of

$$\left(\prod_i \dim\left(x_i\right)\right)^w$$

potential parameter sets that describe the positions and directions of sensors when no constraints are applied. Thereby, $\dim(x_i)$ denotes the quantity of possible values of the optimization variable x_i. The smaller search space of tabu search likely also accounts for the minor growth of κ when the number of sensors to be optimized is increasing.

The values of κ that are provided by tabu search are in our example comparatively small. This indicates a relatively well conditioned linear inverse problem, which is mainly caused by the relatively small number of sources. In addition, the small distances between the sensors and the torso surface lead to a low condition number, too. To substantiate the optimality of the resulting arrangements of sensors, further optimizations with different application-related source and volume conductor models are recommended. The presented study constitutes a first step in the optimization of sensor arrangements for MCG. Since many sensors are positioned close to the boundary of the predefined sensor plane (see Figure 4.2b), the increase of the area of

possible sensor locations seems beneficial. In the subsequent publication of Lau et al. [2008a], PSO is used to improve the arrangement of sensors for vest-like arrays.

Compared with other tabu search approaches as they are applied, for example for schedule or graph optimizations, the presented algorithm appears relatively simple. In particular, we realize just two basic features of tabu search algorithms. First, we use an almost unlimited tabu list to prevent re-evaluations of known sensor combinations. Second, we create new candidate solutions in the neighbourhood of the currently best solution by exchanging sensors. The simplicity of this tabu search strategy enables the control of the optimization by only few parameters: the number of iterations (computational costs), the number of neighbours (costs per iteration), and the number of sensors to be exchanged (locally and/or globally oriented search). To further improve the tabu search strategy, two-level approaches with a subsequent continuous optimization can be deployed.

The tabu search algorithm is designed as a generic tool to optimize sensor arrangements with respect to linear inverse problems. Sensor arrays providing an optimal figure of merit are obtained by directionally testing manifold combinations of sensors. Besides the application in MCG, this tabu search strategy can be applied in numerous fields to place multiple magnetometers, coils, or electrodes optimally. Such fields are MIT [Eichardt et al. 2009b; Gürsoy and Scharfetter 2009], electrical impedance tomography [Polydorides and McCann 2002; Graham and Adler 2007], the transcranial stimulation of direct current [Im et al. 2008; Datta et al. 2008], and the reconstruction of currents in superconducting cables [Bruzzone et al. 2002; Zhang and Di Rienzo 2009].

4.3. Effects of the Definition of Source Space Grids on the Condition

4.3.1. Introduction

We focus in this section on the application of estimating magnetic nanoparticle distributions from remanence measurements. Our objective is to evaluate the effects of parameters that define the source space on the condition of the magnetostatic linear inverse problem. The parameters we consider are the number of sources, the extension of the source space grid, and the directions of sources. In particular, we aim to identify parameter sets that lead to an improved condition of the related lead field matrix.

Furthermore, we quantify the changes of the condition and sensitivity when the distance between sensor and source spaces is increased. This quantification gives relevant insight into the characteristics of the magnetostatic linear inverse problem. For example, substantial differences in the sensitivity to sources can lead to overly biased solutions when applying the TSVD or Tikhonov methods without lead field weighting or normalization.

4.3.2. Methods

Forward Modelling

As sensor models, we use the layouts of two magnetometer arrays, which we typically apply for magnetic nanoparticle measurements. The first array is the 304 channel PTB vector magnetometer system (see section 2.1, Figure 2.1), which we test in 4 configurations: 'PTB 304ch' includes all 304 sensors, 'PTB 114ch' includes the lowest 114 sensors with $Z < 0.5\,\mathrm{cm}$, 'PTB 190ch' includes the sensor layers with $Z < 3.5\,\mathrm{cm}$, and 'PTB 247ch' includes the sensors with $Z < 7.5\,\mathrm{cm}$. The AtB Argos 200 sensor system is used with 195 sensors, 'ATB 195ch'.

To model the source space, we use regular planar grids of magnetostatic dipoles. The distance between the lowest sensor plane and the source grid is 6 cm, which represents a typical distance between the sensor system and the magnetic nanoparticles in our application.

If not stated otherwise, the default parameters for the number of sources is defined to be $25 \times 25 = 625$ and the source grid area is configured with the dimensions $0.28\,\mathrm{m} \times 0.28\,\mathrm{m}$, including extensions of 2 cm beyond the sensor area in the positive and negative X and Y directions. The standard direction of the source dipoles is +Z. The centres of the source grids at $X = Y = 0$ are equivalent to the X/Y-centres of the sensor arrays.

The magnetostatic lead field matrix is set up according section 2.2.2. To quantify and to improve the condition, we use the measure ρ according section 3.4. In the simulation V (see below), we additionally use κ to measure the condition with respect to the 2-norm.

Simulations to Evaluate the Effects of Source Grid Parameters on the Condition

To optimally choose the parameters of the source space grids for our application, we examine in four simulations the effects of the number of sources, the grid extension, and the source dipole directions on the condition of the linear inverse problem. In a fifth simulation, we quantify the relative improvements of TSVD solutions when using source grids that provide according to the simulations I–IV an improved condition.

The objective of **simulation I** is to investigate the influence of the number of sources on ρ. The number is increased from $5 \times 5 = 25$ to $50 \times 50 = 2500$ while keeping the grid extension and the dipole directions constant at their default values. In **simulation II**, we vary the extensions of the source space grid with respect to the sensor area, from $-0.08\,\mathrm{m}$ (smaller than the sensor area) to $+0.12\,\mathrm{m}$ (larger than the sensor area) in positive and negative X and Y directions. **Simulation III** combines the simulations I and II and evaluates simultaneously the effects of the number of sources and the source grid extension on ρ. In **simulation IV**, we gradually change the uniform directions of the dipolar sources in the grid from 0° (Z-direction) to 90° (X-direction).

Concrete effects of adapted source grids on the quality of linear inverse solutions are studied in **simulation V**. TSVD solutions using four exemplary source space grids, identified with 1–4, are compared. In this set, the two pairs 1 & 2 and 3 & 4 provide identical number of sources. To define the source grids 2 and 4, we use grid extensions and source directions, which should improve the condition of the related linear inverse problem. The parameters that define the source grids 1–4 are given in Table 4.1.

We simulate one magnetostatic dipole with a magnetic moment of $1 \times 10^{-9}\,\mathrm{Am}^2$ at the position $P_0 = (0.001, 0.001, 0.065)$. This dipole is directed toward +Z for the source grids 2 and 4 and toward +X for the source grids 1 and 3. To simulate the measurement data, the model of the sensor array 'PTB 304ch' is used. White Gaussian noise with an SNR of 5 dB with respect to the signal level of the simulated source directed toward +X is added. With each source grid, 100 simulations using different random representations of noise are performed.

The quality of the resulting TSVD solutions are evaluated by testing all possible truncation thresholds k, with $1 \leq k \leq 304$. In this process, n^D counts the quantity of parameters k that result in solutions with a maximum dipolar moment located at the grid position (0, 0, 0.6). This position represents for all four source grids the minimum distance to the simulated dipole at P_0 and, therefore, the lowest localization error.

Furthermore, we compare the relative improvements (ri) of the solutions p_μ^k with p_ν^k, where $\mu \in \{1, 3\}$ and $\nu \in \{2, 4\}$ are the indices of the applied source space grids. To determine ri, grids with the same number of sources are compared, that is, grid 1 with 2 and 3 with 4. To obtain a measure ri that not depends on a concrete choice of the truncation threshold k, the individual relative improvements are averaged over

Table 4.1.: Parameters that define the source space grids 1–4 for simulation V of section 4.3.

Source grid	Identified by variable	Number of grid sources	X/Y grid size in m^2	Source directions
1	μ	$25 \times 25 = 625$	0.2×0.2	+X
2	ν	$25 \times 25 = 625$	0.28×0.28	+Z
3	μ	$55 \times 55 = 3025$	0.2×0.2	+X
4	ν	$55 \times 55 = 3025$	0.28×0.28	+Z

k. The ri was evaluated with respect to the residual, ri^{R}, the distance between the grid dipole with the highest estimated moment and P_0, ri^{D}, and the 2-norm of the solution, ri^2. The residual and the 2-norm of the solution should both be small, because their combined minimization is the objective of minimum 2-norm methods, such as TSVD and Tikhonov.

To compare the TSVD solutions p_μ^k and p_ν^k, we define the $ri(\nu, \mu)$ quantities for the residual, the distance to the optimum, and the 2-norm as follows:

$$ri^{\mathrm{R}}(\nu,\mu) := \frac{1}{r}\sum_{k=1}^{r}\frac{\|b - L_\mu\, p_\mu^k\|_2}{\|b - L_\nu\, p_\nu^k\|_2}\,, \tag{4.4}$$

$$ri^{\mathrm{D}}(\nu,\mu) := \frac{1}{r}\sum_{k=1}^{r}\frac{\|P_0 - \mathrm{P}_{\max}\left(p_\mu^k\right)\|_2}{\|P_0 - \mathrm{P}_{\max}\left(p_\nu^k\right)\|_2}\,, \tag{4.5}$$

$$ri^{2}(\nu,\mu) := \frac{1}{r}\sum_{k=1}^{r}\frac{\|p_\mu^k\|_2}{\|p_\nu^k\|_2}\,. \tag{4.6}$$

The term $\mathrm{P}_{\max}(p^k) \in \mathbb{R}^{3\times 1}$ in definition (4.5) represents a 3-by-1 vector that provides the source position with the maximum absolute value among all estimated dipole moments in p^k. Values of $ri(\nu, \mu) > 1$ indicate better solutions when a source grid with index ν is used instead of μ.

Quantifying the Condition and Sensitivity for Increasing Sensor-Source Distances

We quantify the influence of the distance between the source space and the sensor arrays 'PTB 304ch' and 'ATB 195ch' on the condition and the sensitivity. The source space is represented by a 2D planar grid with $25 \times 25 = 625$ regularly arranged magnetostatic dipoles, directed toward +Z. The size of the source grid is $0.28\,\mathrm{m} \times 0.28\,\mathrm{m}$. We increase the distance between the source grid and the lowest

layer of sensors at Z = 0 from 0.025 to 0.25 m. The condition of the resulting lead field matrices are measured by κ and ρ.

To quantify the increase of κ for increasing source-sensor distances, we fit the parameters a and b of the exponential model function

$$f_{ab}^{\kappa}(x) := a\, e^{b\, x}\,, \tag{4.7}$$

to the values of $\kappa(L_i)$, where L_i incorporates the source grid with the distance of x_i to the lowest layer of sensors. To quantify the increase of ρ, we fit the parameters a, b, and c of the polynomial-exponential model function

$$f_{abc}^{\rho}(x) := a\, x^b\, e^{c\, x}\,. \tag{4.8}$$

to the values of $\rho(L_i)$. The polynomial term in (4.8) has a pronounced effect on f^{ρ} for relatively small x, whereas for larger x the function f^{ρ} resembles an exponential function. To minimize the corresponding objective functions

$$\Delta^{\kappa}\,(a,b) := \left[\frac{1}{n}\sum_i \left(\frac{f_{ab}^{\kappa}(x_i)\; -\; \kappa(L_i)}{\kappa(L_i)}\right)^2\right]^{1/2} \qquad \text{and} \tag{4.9}$$

$$\Delta^{\rho}\,(a,b,c) := \left[\frac{1}{n}\sum_i \left(\frac{f_{abc}^{\rho}(x_i)\; -\; \rho(L_i)}{\rho(L_i)}\right)^2\right]^{1/2}\,, \tag{4.10}$$

we use the simplex method of Nelder and Mead [1965].

Furthermore, we visualize for the sensor arrays 'PTB 304ch' and 'ATB 195ch' the decay of the sensitivity. The sensitivity values S^L in the plane of X = 0 are computed by using 100×100 sources. The Z-coordinates of these sources are between 0.025 and -0.25 m and the Y-coordinates are between -0.14 and 0.14 m. At each source position, one dipole pointing toward +Z is located.

To functionally quantify the decay of the sensitivity, we utilize 46 sources that are positioned along the Z-axis with distances x_i to the lowest layer of sensors between -0.025 and -0.25 m. To approximate the decay of the sensitivity S^L according to the distance x, we use the model function

$$f_{abc}^{L}(x) := a\, x^b\, e^{c\, x}\,. \tag{4.11}$$

We fit f^L to the sensitivity values S_i^L by minimizing the objective function

$$\Delta^{L}(a,b,c) := \left[\frac{1}{n}\sum_i \left(\frac{f_{abc}^{L}(x_i)\; -\; S_i^L}{S_i^L}\right)^2\right]^{1/2}\,, \tag{4.12}$$

using the simplex method of Nelder and Mead [1965].

4.3.3. Results

Evaluation of the Influence of Source Grid Parameters on the Condition

The results of **simulation I** indicate for overdetermined inverse problems a considerable increase of ρ for increasing numbers of sources (Figure 4.3a). For the underdetermined linear inverse problem, however, we can observe only a slight increase of ρ when the number of sources is incremented further.

The Figure 4.3b shows the results of **Simulation II**. A source space with extensions clearly smaller than the sensor area impairs the condition considerably. In contrast, positive extensions of the grid beyond the area of sensors lead to a reduction of ρ.

In Figure 4.3c, the results of **simulation III** for the sensor array 'PTB 304ch' are shown. In this simulation, the influence of the number of sources and the grid extension are evaluated simultaneously. The plots show almost no visual differences for ρ when the grid extension is $\geq 2\,\mathrm{cm}$ and when the number of sources is equal or larger than about two times the number of sensors. As already indicated by the simulations I and II, ρ increases considerably when the extension of the source space grid is clearly smaller than the area of the sensors. In contrast, ρ is particularly low when fewer sources than sensors are used.

Figure 4.3d shows the results of **simulation IV**. Source space grids with dipoles directed toward +Z result in relatively low values of ρ. Deviations of the source directions of about $\geq 35°$ from Z lead to clearly worse values of ρ.

Table 4.2 denotes the results of **simulation V** for ρ, κ, and the mean of n^D when using the source space grids 1–4. When the source grid 2 is used instead of 1 (both with 625 sources) ρ drops by a value of about 12 and κ by a factor of 135. For grid 1, only $n^D = 22$ of 304 (7.2%) truncation thresholds k, on average, provide the lowest achievable localization error. When using grid 2, 62 of 304 (20.5%) thresholds k, on average, result in solutions with a minimum localization error. Considering the denser source grids 3 and 4 with 3025 magnetostatic dipoles, the grid 4 shows similar improvements of ρ and κ with respect to grid 3. For the source grid 3, the average number of truncation thresholds that result in solutions with a minimum distance to the simulated dipole is 8 (2.5%); with grid 4 it increases to 34 (11.3%).

The individual results of ri^{R}, ri^{D}, and ri^2 using 100 different representations of noise are shown in Figure 4.4. The averaged relative improvements when using source grid 2 instead of 1 (subfigure 4.4a) are for ri^{R} at 1.4, for ri^{D} at 3.0, and for ri^2 at 26.4. When comparing source grid 4 with 3 (subfigure 4.4b), the mean values of the relative improvements are slightly lower with ri^{R} at 1.3, ri^{D} at 3.0, and ri^2 at 23.0. The variations of ri by using 100 different representations of noise are relatively small. No representation results in values of ri smaller or equal 1.

Figure 4.5 shows for the source grids 1–4 and one representation of noise the best TSVD solutions, which provide minimal localization errors, residuals, and artefacts. The left column of Figure 4.5 presents the results for the source grids 1 and 3, which both are obtained with a truncation threshold of $k = 28$. The right column shows the best TSVD solution for the source grids 2 and 4, using a truncation threshold of

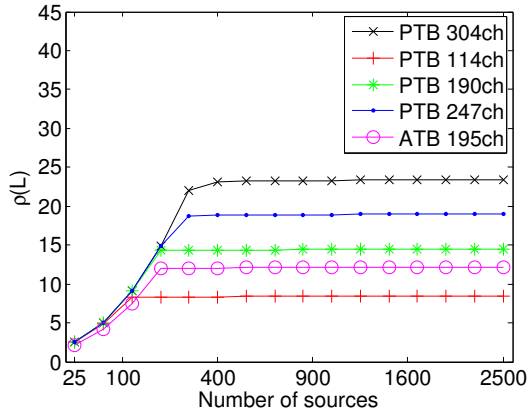

(a) Simulation I.

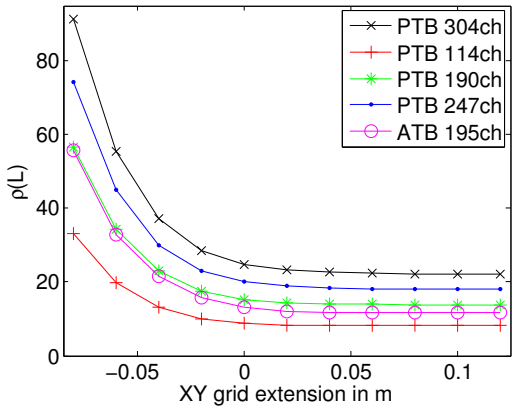

(b) Simulation II.

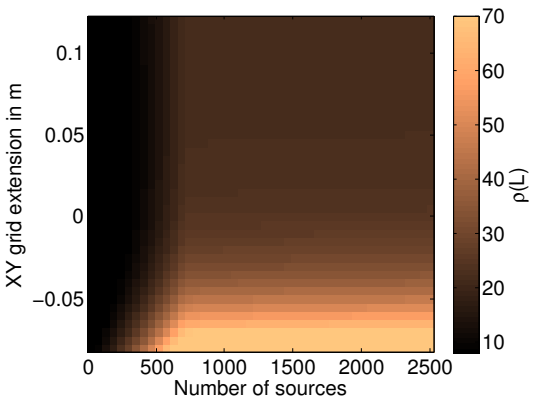

(c) Simulation III.

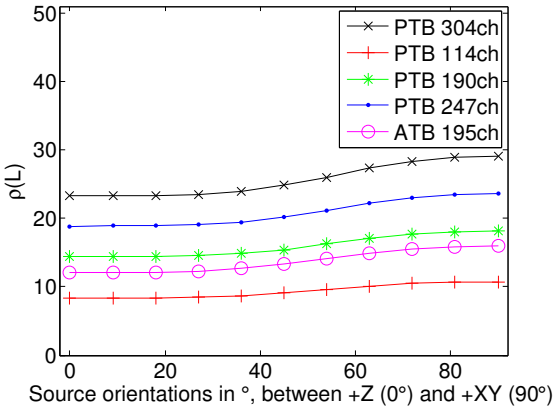

(d) Simulation IV.

Figure 4.3.: Results of the simulations I–IV, showing the effects of the number of sources, the extension of the source space, and the source direction on the measure of condition, ρ. Lower values of ρ indicate a better condition.

$k = 40$. Corresponding to the Figure 4.5, the linear inverse solutions provide clearly less artefacts and the area of the highest source activity is more symmetric and focal when the source grids 2 and 4 are used instead of 1 and 3. The differences between the solutions for the source grids of 625 and 3025 sources are relatively small. For grids 3 and 4 with 3025 magnetostatic dipoles, the TSVD method results in smoother estimations with dipole moments that are by a factor of 5 smaller compared with the source grids 1 and 2.

Quantification of the Condition and Sensitivity

Figure 4.6a shows the results of the fit of f^{κ} to the increase of the condition number κ for the sensor arrays 'PTB 304ch' and 'ATB 195ch'. The increase of κ for increasing source-sensor distances can be functionally described for the sensor system 'PTB

Table 4.2.: Results of ρ, κ, and n^D for the source space grids 1–4 of simulation V.

Source grid	ρ	κ	mean $\left(n^D\right)$
1	35.2	2.7×10^{13}	22±6.7
2	23.3	2.0×10^{11}	62±10.0
3	35.8	2.0×10^{13}	8±4.2
4	23.4	2.0×10^{11}	34±9.7

304ch' by

$$f^{\kappa}(x) = 6.72 \times 10^{7}\, e^{131.7\, x}$$

and for the 'ATB 195ch' by

$$f^{\kappa}(x) = 1.27 \times 10^{5}\, e^{90.6\, x}\,.$$

Because the increase of κ for the 'PTB 304ch' changes considerably for indices $i \geq 30$ with $x_i \geq 17\,\text{cm}$, the fit was performed by using only the first 29 values of κ. All values of κ for $x_i \geq 17\,\text{cm}$ are in the scale of 1×10^{17}.

The fitted functions that quantify the increase of ρ are shown in Figure 4.6b. For the sensor array 'PTB 304ch', the optimization leads to

$$f^{\rho}(x) = 3464\, x^{1.7}\, e^{-3.46\, x}$$

and for the 'ATB 195ch' to

$$f^{\rho}(x) = 2134\, x^{1.76}\, e^{-3.46\, x}\,.$$

The logarithmic sensitivity distributions $\log_{10}(S^L)$ for the sensor arrays 'PTB 304ch' and 'ATB 195ch' are illustrated in Figure 4.7. Figure 4.8a shows the values of S^L in descending order. According to these figures, the sensitivity provided by the sensor array 'ATB 195ch' is close to the sensors slightly higher compared with the 'PTB 304ch'. However, the sensitivity for the 'ATB 195ch' decays faster and is lower for more distant sources. The sensitivity values for sources located along the Z-axis and the fitted model functions f^L are presented in Figure 4.8b. The fit of the parameters a, b and c results for the 'PTB 304ch' sensor array in

$$f^{L}(x) = 1.4 \times 10^{-7}\, x^{-0.93}\, e^{-7.68\, x}$$

and for the 'ATB 195ch' in

$$f^{L}(x) = 8.8 \times 10^{-8}\, x^{-1.05}\, e^{-7.6\, x}\,.$$

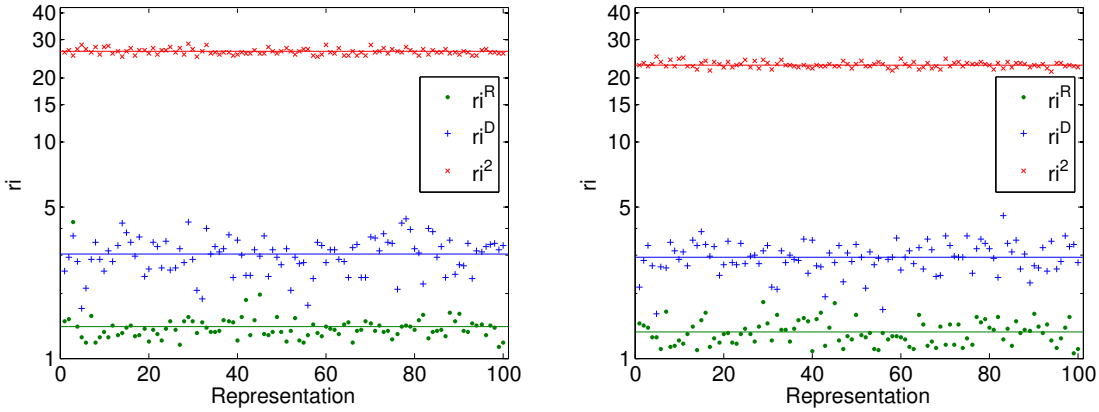

(a) $ri(2,1)$ – relative improvements when using source grid 2 instead of 1.

(b) $ri(4,3)$ – relative improvements when using source grid 4 instead of 3.

Figure 4.4.: Results of simulation V showing the relative improvements ri^R, ri^D, and ri^2 when the source space grids 3 and 4 are used instead of 1 and 2. The mean values of ri are indicated by the horizontal lines. Higher ordinate values represent higher improvements.

4.3.4. Discussion and Conclusions

The inverse problem in our application is typically underdetermined; therefore, the number of sources produces a relatively small effect on the lead field condition. However, the practical application of a sparse source grid with equal or fewer numbers of sources than sensors can considerably improve the condition upon further reductions in the number of sources. The area of the source grid should extend over the sensor area. Brauer et al. [2000] concluded previously, based on a phantom experiment, that a two-dimensional source space grid should extend over at least five times the area of the distributed source. Accounting for the spatial resolution and the number of dipoles within the grid, an extension of $1-3\,\mathrm{cm}$ in each direction should be adequate, in practice.

The orientations of the sources in our application and, therefore, the direction of the magnetic field applied during excitation should not deviate more than 35° from the Z-direction. In addition, sources oriented toward Z also provided for the given sensor arrays higher signal levels and better SNRs.

All five sensor array configurations in simulations I–IV yield a qualitatively similar behavior that depended on the number of sensors. The best results for ρ is obtained for the sensor configuration ‘PTB 114ch’. However, the better values of ρ obtained from the ‘PTB 114ch’, as compared with the values obtained from ‘PTB 304ch’, results mainly from the reduced number of singular values of the lead field matrix. A smaller number of sensors, as compared with the number of other arrays, introduces a relatively small redundancy in the measurement values; however, the ‘PTB 114ch’

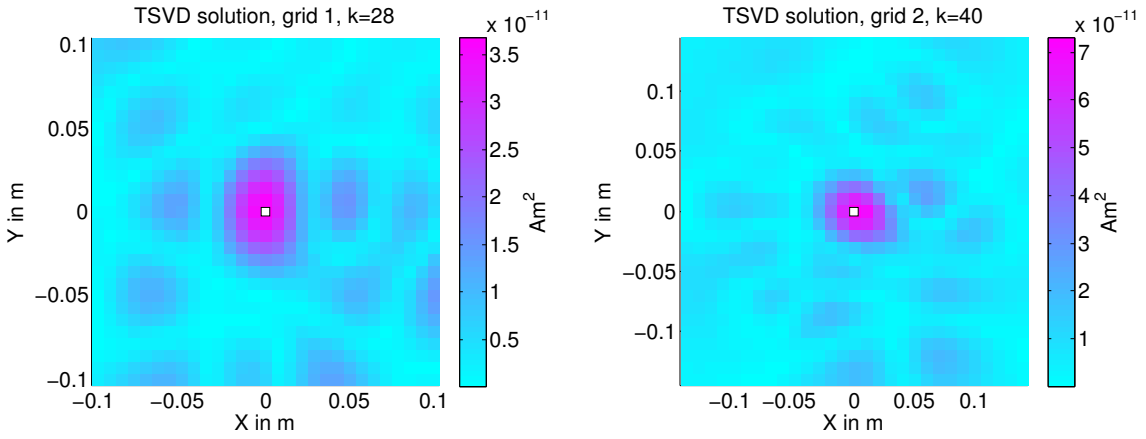

(a) TSVD result using source grid 1.

(b) Source grid 2.

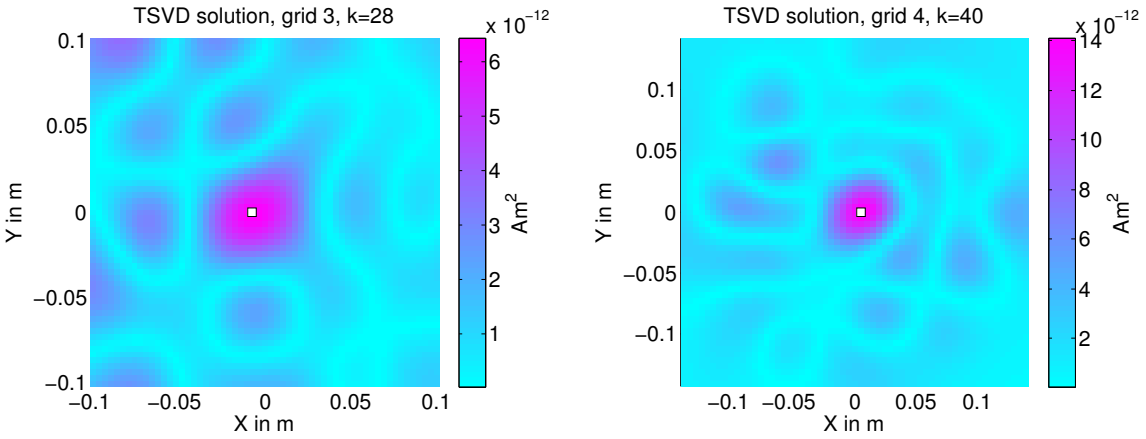

(c) Source grid 3.

(d) Source grid 4.

Figure 4.5.: Plots of the best TSVD solutions of simulation V showing the estimated magnetic moments of the dipoles defined by the source grids 1–4. The sources with the largest moment are indicated by □.

sensors pick up less information from the magnetic field.

As shown by the examples illustrated in simulation V, the quality of the inverse solutions could be improved considerably using the source grid adaptations presented in this paper. Solutions using the adapted grids provide fewer artifacts, smaller L2-norms, and smaller residuals. In addition, a greater fraction of the possible TSVD regularization parameters lead to optimal solutions in terms of the distance to the simulated source. Therefore, the appropriate determination of these parameters, for instance, using the Generalized-Cross-Validation [Wahba 1977] or the L-curve [Hansen 1992] methods, should be easier and more reliable, in practice.

Some of our findings, including the specific recommendations for the source grid extensions and the direction of the magnetic sources, are directly related to the application of magnetic nanoparticle imaging. However, we expect that the basic

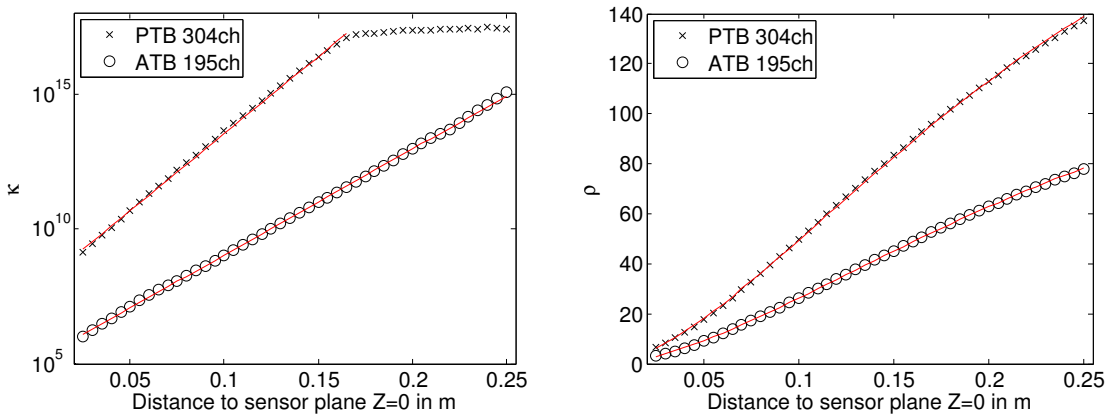

(a) Logarithmic plot of f^{κ} and κ.

(b) Plot of f^{ρ} and ρ.

Figure 4.6.: Values of κ and ρ for increasing distances between the source space and the lowest level of sensors when using the sensor arrays 'PTB 304ch' and 'ATB 195ch'. The fitted functions f^{κ} (a) and f^{ρ} (b) are indicated by thin red lines; the underlying data values are indicated by $\times$ and $\circ$.

findings, such as the general influence of the number of grid sources and the extensions of the source space on the lead field condition, are relevant to various linear inverse problems in magnetic applications. The findings of this study were used, for example, to detect ferromagnetic objects in geomagnetic measurements.

For the reconstruction of electromagnetic sources in EEG and MEG, the definition of the source spaces differs considerably from the application of magnetic nanoparticle imaging. The source space for EEG and MEG is typically determined by using anatomical information of the cortex surface. In this process, the total number of sources and the decision, whether to define one (to fix the directions of the sources) or three dipoles (to enable arbitrary source directions) at each source position, represent two obvious options to influence the condition by means of source space adaptations. Thus, future studies that investigate the possibilities to improve the condition of linear inverse problems in these applications are relevant.

The increase of κ and ρ for increasing distances between the source space and the sensors arrays 'PTB 304ch' and 'ATB 195ch' can be well approximated by using the model functions f^{κ} and f^{ρ}. In this simulation, κ does not exceed values of 10^{17} considerably. This behaviour can be explained by the limited numerical accuracy, since κ is larger than the inverse of the relative machine accuracy, which is $\epsilon \approx 2.2 \times 10^{-16}$ (see section 3.3). Similar numerical effects were not observed when computing ρ. However, this limitation of κ has for the imaging of magnetic nanoparticles only a minor impact, because source-sensor distances of $> 17\,\mathrm{cm}$ are beyond the typical measurement distance.

The decay of the sensitivity for the sensors arrays 'PTB 304ch' and 'ATB 195ch' can be well described by a polynomial-exponential function. Compared with the

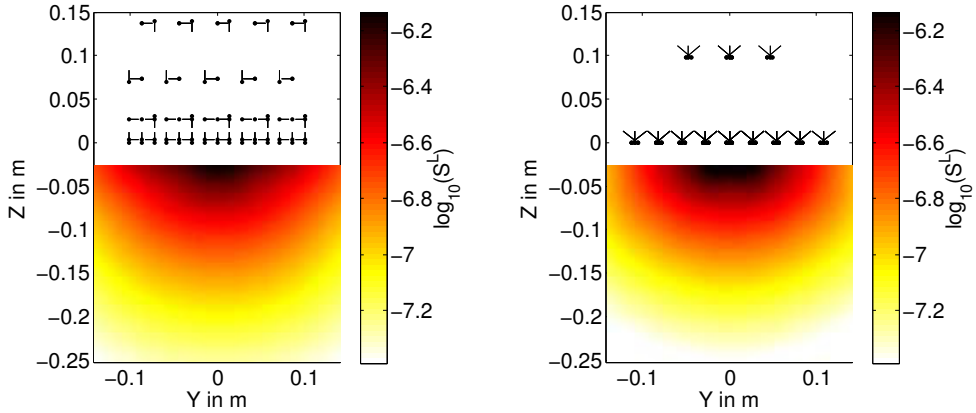

(a) Sensor array 'PTB 304ch'. **(b)** Sensor array 'ATB 195ch'.

Figure 4.7.: Plots of the logarithmic sensitivity distributions of S^L in the plane of X = 0 for the sensor arrays 'PTB 304ch' and 'ATB 195ch'. Dot and bar markers denote the sensor positions and directions for $0 \leq \mathrm{Z} \leq 15\,\mathrm{cm}$.

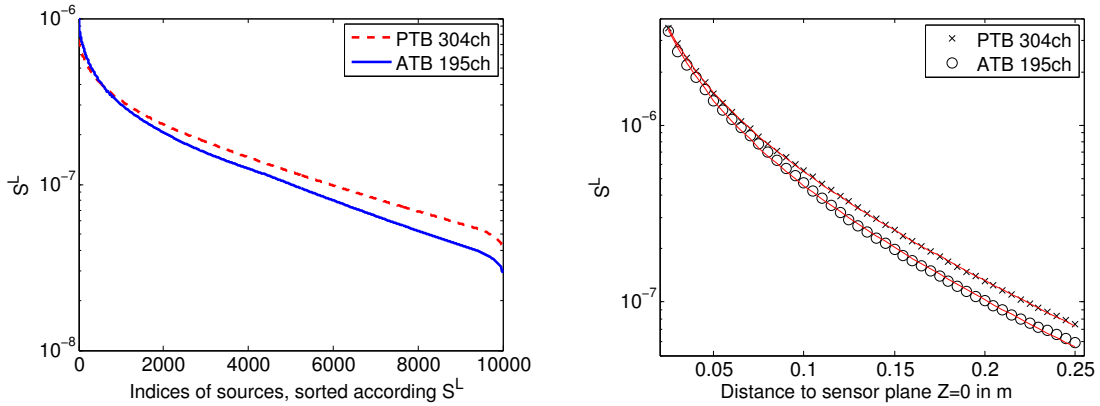

(a) Logarithmic plot of sensitivity values S^L in the plane of $X = 0$, sorted in descending order.

(b) Logarithmic plot of S^L for the sources located along the Z-axis. The fitted functions f^L are indicated by the red lines.

Figure 4.8.: Qualitative evaluation of the sensitivity for 'PTB 304ch' and 'ATB 195ch'.

sensor array 'PTB 304ch', the array 'ATB 195ch' provides slightly higher sensitivities close to the sensors and slightly lower sensitivities to more distant sources. For the most applications, however, the differences in the sensitivities provided by the sensor arrangements of both arrays are presumably small. Similar decays of the sensitivity can also be expected for sensor systems with similar arrangements of magnetometers.

4.4. Effects of Variations in Magnetometer Directions on the Condition

4.4.1. Introduction

Hidden ferromagnetic and paramagnetic objects cause deformations of the earth magnetic field, which can be measured by magnetometers or gradiometers. In our simulation study [Eichardt et al. 2009a], we investigated the localization of buried magnetic objects using a weighted TSVD approach. Sensor positions and orientations were taken from a real measurement data set. They were continuously changing, since the vehicle carrying the sensor system was pulled by car over a very rough surface. It turned out that the realistic sensor setups provided linear inverse solutions with considerably increased stability compared with artificially generated setups that used in parallel arranged sensors.

Therefore, the objective of this study is to systematically examine the influence of random variations in the sensor directions on the condition of the magnetostatic linear inverse problem. With simulations we evaluate, if the experimentally observed effect for one specific setup of sensors holds for generic sensor arrays, too.

4.4.2. Methods

Source and Sensor Models

To set up the lead field matrix L, we use five examples of planar 2D (indicated by 1, 2, 5) and spatial 3D source grids (indicated by 3, 4). The parameters of these source grids are given in Table 4.3. At each source position defined by the grids, three orthogonal magnetostatic dipoles are located to enable arbitrary directions of the sources.

Parameters that define the employed sensor arrays are give in Table 4.4. The lowest layer of sensors is in each case located in the $\mathrm{Z} = 0$ plane. The sensor array A represents a three-axial arrangement magnetometers. The sensor arrays B–D are mono-axial with sensors directed toward $-\mathrm{Z}$ by default. D exhibits two layers of sensors at $\mathrm{Z} = 0$ and $\mathrm{Z} = 0.05$. This approach of multiple layers of sensors can be found in many present sensor arrays; see, for example the section 2.1 and the Figures 2.1 and 2.2.

Random Variations in the Sensor Directions

The default sensor directions d, which are $[1, 0, 0]^T$ for +X, $[0, 1, 0]^T$ for +Y, and $[0, 0, -1]^T$ for $-$Z, are modified independently by using Gaussian distributed random variations $\Delta d = (\Delta d_x, \Delta d_y, \Delta d_z)^T$. The distributions of Δd hold a mean value of 0° and standard deviations $\mathrm{SD}(\Delta d)$ of 0.05, 0.5, 1, 2.5, 5, 10, 15, 20, and 25°. Variations in the sensor directions are obtained by rotations of d, first, by Δd_x about the X-axis, second, by Δd_y about the Y-axis and, third, by Δd_z about the Z-axis. For the array

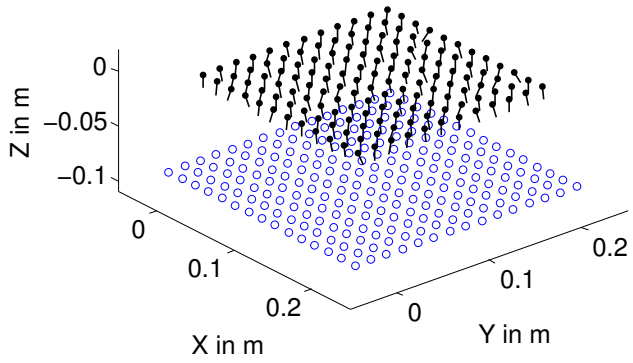

Figure 4.9.: Example configuration illustrating the source positions of grid 2 (∘) and the sensor positions of array B (•). The sensors directions (small bars) are randomly varied about −Z with SD(Δd) = 10°.

A, the orthogonality in the three-axial sensors is preserved. The default lead field matrices that use uniformly toward −Z (mono-axial sensor arrays B–D) or toward (+X, +Y, −Z) (three-axial array A) oriented magnetometer sensors are indicated by L_0. The representations of the lead field matrices using randomly varied sensor directions are denoted by L_i, with index $i > 0$. Figure 4.9 shows one example of randomly varied sensor directions for the array B together with the source positions of grid 2.

Evaluation of the Sensor Arrays

To quantify the effects of non-uniformly oriented sensors on the condition, we compute κ for the related lead field matrices. Relative changes of κ are denoted by

$$\Delta\kappa(L_i) := \frac{\kappa(L_i)}{\kappa(L_0)}\,, \tag{4.13}$$

where L_i is the lead field matrix with respect to the ith representation of randomly varied sensor directions; L_0 is the matrix with identical definitions of the source space and the sensor positions but with uniform directions of sensors. Values of $\Delta\kappa(L_i) < 0$ indicate improvements of the condition when L_i is used instead of L_0.

Table 4.3.: Parameters that define the source space grids 1–5 of section 4.4.

Source grid	Source positions (X, Y, Z) min	max	Number of source pos. ($X \times Y \times Z$)
1	−(0.02, 0.02, 0.09)	(0.22, 0.22, −0.09)	$10 \times 10 \times 1 = 100$
2	−(0.02, 0.02, 0.09)	(0.22, 0.22, −0.09)	$15 \times 15 \times 1 = 225$
3	−(0.02, 0.02, 0.15)	(0.22, 0.22, −0.06)	$8 \times 8 \times 3 = 192$
4	−(0.02, 0.02, 0.21)	(0.22, 0.22, −0.06)	$15 \times 15 \times 6 = 1350$
5	−(0.01, 0.01, 0.05)	(0.21, 0.21, −0.05)	$20 \times 20 \times 1 = 400$

Table 4.4.: Parameters of the simulated sensor arrays A–D of section 4.4.

Sensor array	Sensor positions (X, Y, Z) min	max	Sensor directions	Number of sensors
A	(0, 0, 0)	(0.2, 0.2, 0)	+X, +Y, -Z	$3 \times 12 \times 12 = 432$
B	(0, 0, 0)	(0.2, 0.2, 0)	-Z	$12 \times 12 = 144$
C	(0, 0, 0)	(0.2, 0.2, 0)	-Z	$21 \times 21 = 441$
D	(0, 0, 0)	(0.2, 0.2, 0.05)	-Z	$10 \times 10 + 9 \times 9 = 181$

Simulation Studies

In **simulation I**, the influence of random variations Δd in the sensor directions is analysed. The different combinations of sensor arrays A–D and source space grids 1–5 are investigated. The mean values and the standard deviations for $\Delta\kappa$ are computed by using 100 representations of randomly varied sensor directions, with SD(Δd) between 0.05° and 25°.

In **simulation II**, the effects of non-uniformly oriented sensors on the condition are examined. The numbers of sensors in X- and Y-direction are incremented from $7 \times 7 = 49$ to $23 \times 23 = 529$. Other parameters of the sensor arrays, such as the extension and distance to the source space, correspond to the sensor arrays B and C. Furthermore, we use the source space of grid 2 and apply variations to the sensor directions with SD(Δd) = 0.05°, 1°, 10°, and 25° in 100 repeated runs each.

The objective of **simulation III** is to evaluate the influence of variations in the sensor Z-positions in combination with variations in the sensor directions. We use the source grid 2 and sensor arrays similarly defined to B but with sensor Z-positions that are uniformly randomly distributed in $(0, sZ)$, with $0 \leq sZ \leq 0.1$. For each value of sZ, 50 sensor arrays with random sensor Z-positions are generated. Subsequently, the effects of variations in the sensor directions using these particular arrays are analysed. We perform 50 repeated runs with variations in the sensor directions of SD(Δd) = 0.05°, 1°, 10°, and 25°. The mean values of $\Delta\kappa$ are computed for each value of sZ and SD(Δd) from altogether 50×50 individual results.

In **simulation IV**, we examine for the configuration C2 the effects of variations in the sensor directions on the TSVD solution of the linear inverse problem. In this process, one dipole at position $P_0 = (0.996, 0.996, -0.1)$, directed to (1, 1, 1), and with a magnetic moment of $1 \times 10^{-9}\,\mathrm{Am}^2$ is simulated. The nearest source of the grid 2 is located at (0.1, 0.1, −0.09). We compare the TSVD solutions when using the sensor array C with randomly varying, SD(Δd) = 25°, and with uniform sensor directions. As in the previous section 4.3.2, the measures for the relative improvement of linear inverse solutions are applied, in which ri^{R} specifies the improvements with respect to the residual, ri^{D} the improvements with respect to the distance between the strongest estimated dipole and the simulated source, and ri^2 the improvements of the 2-norm. Altogether, we conduct 100 runs using different representations of white Gaussian noise with an SNR of 5 dB and randomly varied sensor directions. In

Table 4.5.: Condition number κ for lead field matrices L_0 with uniformly oriented sensors.

Sensor array	Source grid 1	2	3	4	5
A	1.53×10^8	2.12×10^{11}	2.23×10^{12}	5.13×10^7	1.52×10^6
B	1.9×10^7	4.12×10^6	1.23×10^5	1.79×10^4	1.81×10^3
C	1.65×10^9	2.41×10^{14}	2.3×10^{15}	8.45×10^9	4.92×10^8
D	6.81×10^8	5.52×10^8	2.83×10^8	6.54×10^6	1.04×10^6

each run, the values of ri^{R}, ri^{D}, and ri^2 are averaged over the r possible truncation thresholds.

In addition, the TSVD solutions using uniform and one example of varied sensor directions are visually compared. White Gaussian noise with SNRs of 5 dB and 30 dB is added to obtain two samples of the measurement data. The two solutions that provide the minimum localization error and that are obtained with the largest possible truncation threshold are compared.

4.4.3. Results

Simulation I: The effects of random sensor direction variations on the relative condition number $\Delta\kappa$ are shown in Figure 4.10 for the different combinations of sensor arrays and source space grids. The condition numbers $\kappa(L_0)$ for lead fields without variations in the sensor directions are shown in Table 4.5. The mean values of $\Delta\kappa(L_i)$ for lead field matrices L_i representing mono-axial sensor arrays B–D can be clearly reduced even by small variations in the sensor directions. Larger variations lead to higher reductions of $\Delta\kappa$, in which the decay of $\Delta\kappa$ decreases for increasing values of $\mathrm{SD}(\Delta d)$. As indicated by the dotted lines in Figure 4.10a, the standard deviations of $\Delta\kappa$ are relatively small. Only for the combination D5, higher deviations of $\Delta\kappa$ can be observed. This also leads to the minor non-monotonicity of $\mathrm{mean}(\Delta\kappa)$ for the configuration D5 in Figure 4.10d, for $5^\circ \leq \mathrm{SD}(\Delta d) \leq 25^\circ$. As expected, random variations in the sensor directions have no effect on κ when the sensor array A with three-axial sensors is used (Figure 4.10a, A2). The improvements of κ when using mono-axial arrays in combination with different source grids varied relatively widely: With $\mathrm{SD}(\Delta d) = 25^\circ$, we obtain mean values of $\Delta\kappa$ between 0.6 (Figure 4.10d, D5) and 3×10^{-4} (Figure 4.10c, C2).

Simulation II: Figure 4.11 shows the mean values of $\Delta\kappa$ for random variations in the sensor directions for an increasing number of sensors in the X- and Y-directions. The results indicate an articulate reduction of $\mathrm{mean}(\Delta\kappa)$ by approximately three orders of magnitude when the number of mono-axial sensors is incremented from $7 \times 7 = 49$ to $19 \times 19 = 361$. In this process, $\kappa(L_0)$ increases from 762 to 1.2×10^{13} when the sensors are uniformly oriented. For the sensor arrays with $21 \times 21 = 441$ and $23 \times 23 = 529$ sensors, $\kappa(L_0)$ is 2.4×10^{14} and 1.6×10^{16}, respectively, which likely

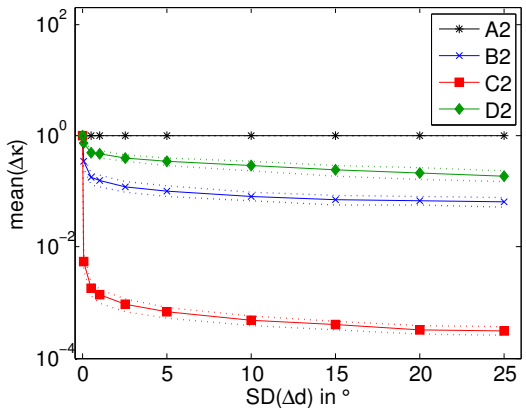

(a) Plots of $\Delta\kappa$ against SD(Δd) for source grid 2.

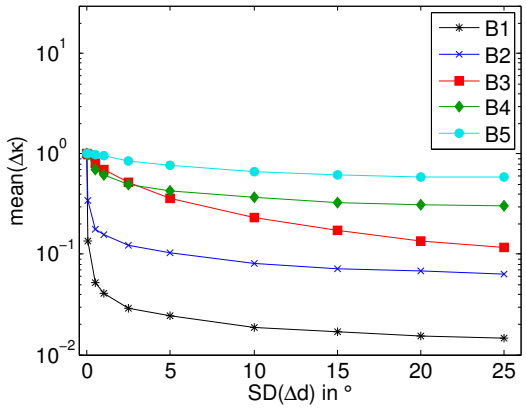

(b) Sensor array B.

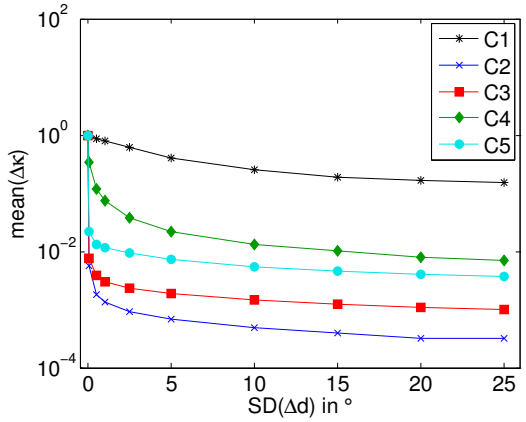

(c) Sensor array C.

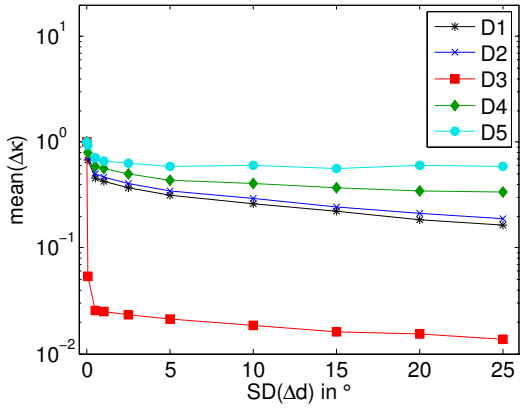

(d) Sensor array D.

Figure 4.10.: Results of simulation I: mean values of $\Delta\kappa$ in logarithmic representation using the sensor arrays A–D and the source grids 1–5. The standard deviations for $\Delta\kappa$ are indicated in (a) by the dotted lines.

causes the small increase of mean $\Delta(\kappa)$ for > 361 sensors. Also in this simulation, larger random variations in the directions lead to higher improvements of the condition.

Simulation III: The objective of this study is to investigate the influence of sensor direction variations in combination with varying sensor Z-positions. Figure 4.12a shows distinct improvements of κ when larger variations in the sensor directions with SD(Δd) $\geq 10°$ are used and when the sensor Z-positions are 0 (planar arrangement) or distributed in a small interval of $(0, sZ)$, with $0.0002 \geq sZ \geq 0.005$ m. For values of sZ between 0.01 and 0.03, the reduction of $\Delta\kappa$ is minimal, considering all the tested intervals of $(0, sZ)$. Figure 4.12b presents the results for $\kappa(L_0)$ when the Z-positions of the sensors are uniformly randomly distributed in $(0, sZ)$. The sensors are constantly directed toward $-$Z. These values of $\kappa(L_0)$ are used to compute $\Delta\kappa$ for varying sensor directions as shown in Figure 4.12a. The results of Figure 4.12b

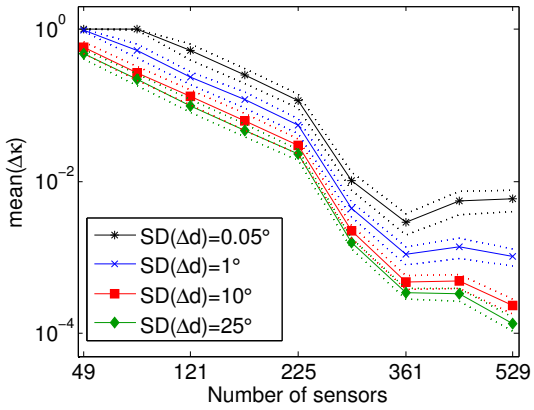

Figure 4.11.: Results of simulation II: mean values of $\Delta\kappa$ using the source grid 2 and sensor arrays similar to B. The number of sensors is incremented from 49 to 529. The standard deviations of $\Delta\kappa$ are indicated by the dotted lines.

indicate that $\kappa(L_0)$ is reduced in all except two cases when the sensor Z-positions are randomly distributed between 0.0002 and 0.02 m. By varying the sensor Z-positions, the sensors are not moved closer to the sources compared with the configuration B2 that uses Z-positions of the sensors equal to 0. An increase of sZ leads to higher expected values for the distances between the sensors and the sources, which causes the increase of $\kappa(L_0)$ for $sZ > 0.01$.

Simulation IV: Figure 4.13 shows clear relative improvements for the residual and the 2-norm of solutions when the sensors of the array C are not uniformly oriented. The distances between the position of the reconstructed dipole with the maximum estimated moment and the simulated source at P_0 improve only marginally. The Figure 4.14 presents the singular values of the lead field for the configuration C2 when using uniform and randomly varied sensor directions. With varied sensor directions, the decay of the singular values is reduced. Particularly the smallest singular values are larger compared with the corresponding lead fields that incorporate uniform sensor directions. In Figure 4.15, two examples of TSVD solutions utilizing the sensor array C with uniform and varying sensor directions are shown. Only marginal differences can be observed when applying noise with an SNR of 5 dB: The artefacts in subfigure 4.15a are slightly more pronounced compared with the results shown in subfigure 4.15b. When using an SNR of 30 dB, however, clearly more distortions are visible in the subfigure 4.15c (uniform sensor directions) compared with the subfigure 4.15d (randomly varied sensor directions). Figure 4.14 shows in this example for randomly varied and for uniform sensor directions almost no differences for the first 30 singular values of the related lead field matrices. Beginning at index 30, the decay of the singular values is clearly reduced when randomly varied instead of uniform sensor directions are used.

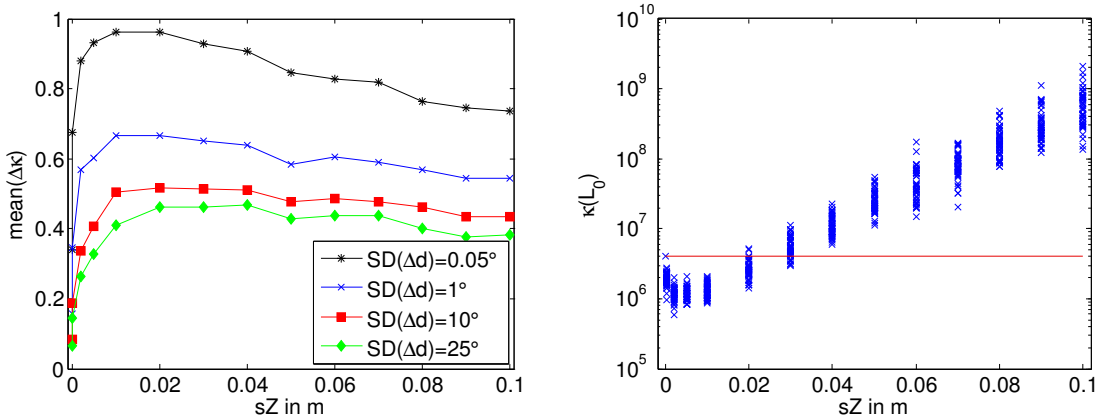

(a) Plot of $\Delta\kappa$ against values of sZ. **(b)** Effects of parameters sZ on $\kappa(L_0)$.

Figure 4.12.: Results for $\Delta\kappa$ and $\kappa(L_0)$ of simulation III. The effects of variations in the sensor positions and directions are shown in (a). The $\times$ in (b) indicate the condition of the arrays with varied sensor Z-position and directions toward $-$Z. The line in (b) indicates κ for configuration B2 without variations.

4.4.4. Discussion and Conclusions

Our findings show that the condition of magnetostatic linear inverse problems can be clearly improved when mono-axial sensors are directed non-uniformly.

The effects on the inverse solutions depend on the applied models of sensors and sources, the inverse solver, the regularization model, the determination of the regularization parameters, and the noise contained in the data. Simulation IV uses a very simple approach but we can already observe considerable improvements of the inverse solutions. The impact of noise and errors on the result shown in Figure 4.15c can be reduced by using a smaller truncation threshold, which, however, increases the residual and the error due to the regularization, respectively.

As a consequence of this study, mono-axial sensors should be directed non-uniformly to support more stable linear inverse solutions. Considerable improvements of the condition can be observed in cases with initially high values of the condition number κ. In our examples, κ was reduced by random variations in sensor directions by factors between 0.6 and 3×10^{-4}, depending on the combination of the source grid and the sensor arrangement. Larger variations, in this study up to 25°, lead to higher improvements of the condition. Besides varying the sensor directions, also small variations in the sensor Z-positions of planar mono-axial arrays, in our example between 0.2 mm and 2 cm, seem to be beneficial for the condition.

The results of this section are likely relevant for further magnetic applications, such as the optimal placements of probes to reconstruct current profiles in superconducting cables [Bruzzone et al. 2002; Formisano and Martone 2003]. Moreover, applications in the fields of electrical engineering, geophysics, materials sciences, and mechanics

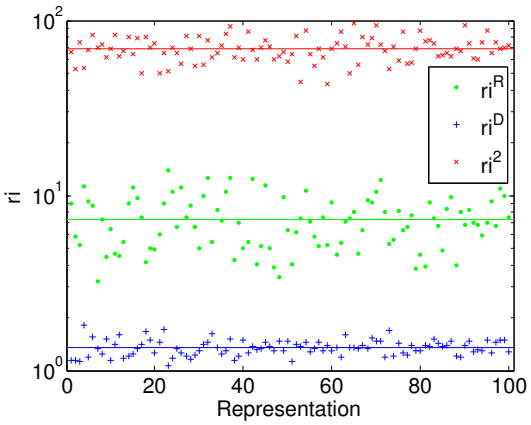

Figure 4.13.: Results of simulation IV: logarithmic plots of the relative improvements for configuration C2 when varying the sensor directions with SD(Δd) = 25°; with respect to the residual (ri^{R}), the distance to the optimum (ri^{D}), and the 2-norm (ri^2).

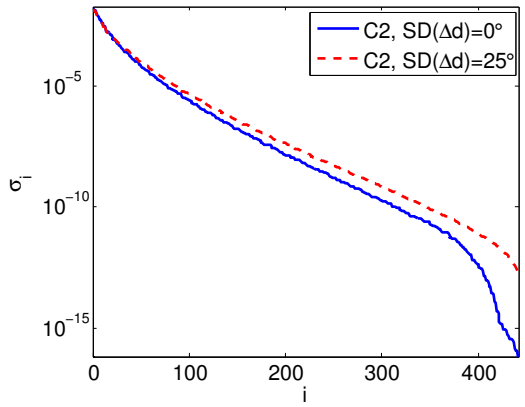

Figure 4.14.: Results of simulation IV: logarithmic plot of the sorted singular values for C2 using uniform (solid line) and varied sensor directions (dashed line).

that focus on the measurement and the inverse analysis of vectorial quantities, such as force, velocity, or acceleration, may benefit when sensor positions and directions are varying.

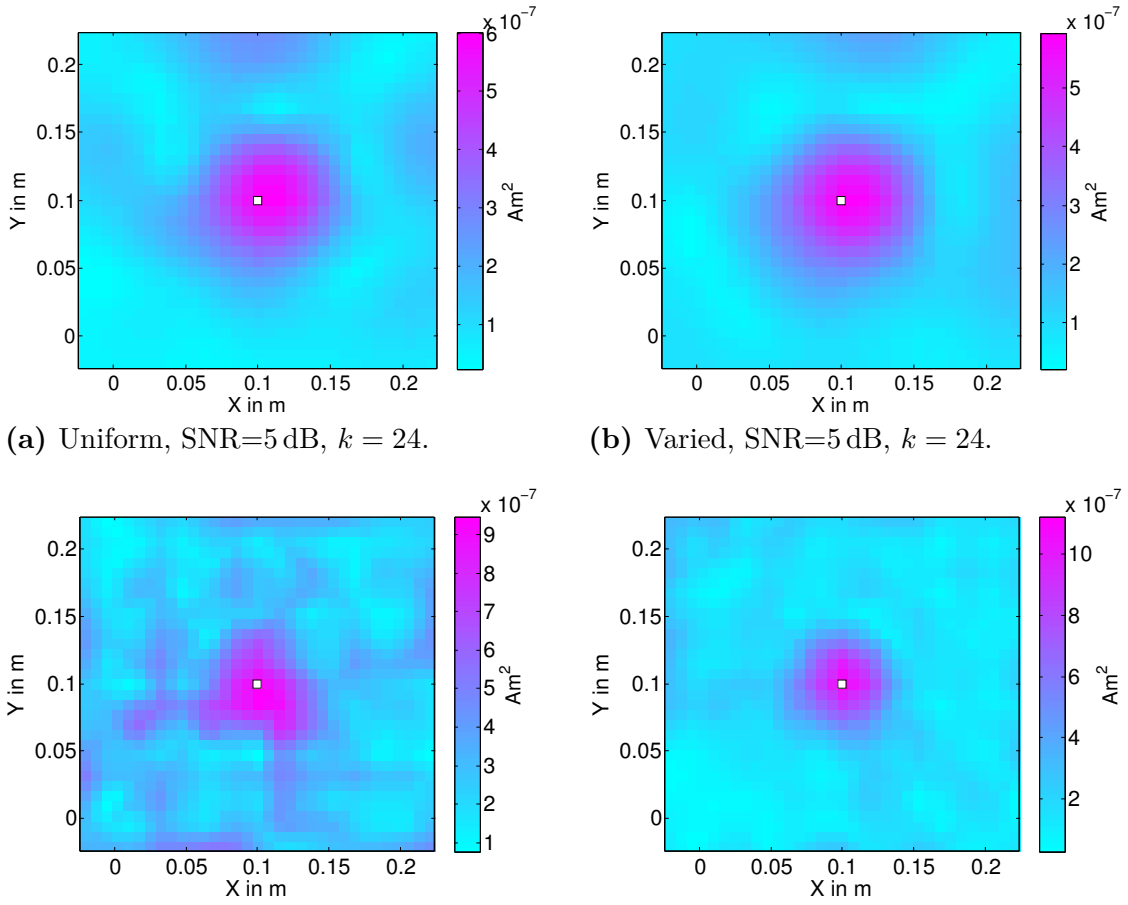

(a) Uniform, SNR=5 dB, $k = 24$.

(b) Varied, SNR=5 dB, $k = 24$.

(c) Uniform, SNR=30 dB, $k = 100$.

(d) Varied, SNR=30 dB, $k = 100$.

Figure 4.15.: Results of simulation IV: plots of the estimated magnetic moments of TSVD solutions for configuration C2, using uniform (left images) and randomly varied sensor directions with SD(Δd) = 25° (right images). The source positions with the largest estimated moment are indicated by □.

4.5. Sensitivity Evaluation for Coil Setups in MIT

4.5.1. Introduction

The sensitivity to conductivity changes of MIT systems is of crucial importance. Owing to the decrease of the primary and secondary magnetic fields, the sensitivity to conductivity changes decays substantially with increasing distances to the coils. The absolute values and the decay of the sensitivity depend on the arrangement, windings, cross sectional areas, and types of coils, as well as on the frequencies and currents used to excite the primary magnetic fields.

In simulations, we compare the sensitivity to the changes of conductivity and the condition of six exemplary MIT systems with cylindrical and hemispherical arrangements of the coils. Two of these systems are models of existing MIT systems. Prior evaluations of the sensitivity in the field of MIT were presented, for instance by Soleimani [2005, section 3.5], Soleimani et al. [2006], and Pham and Peyton [2008].

4.5.2. Methods

To evaluate the sensitivity of different MIT coil setups, we use an EFEM model of tetrahedral elements with volumes of $4/3\,\mathrm{cm}^3$ each. Thereby, six tetrahedra form a cube with an length of 2 cm. The fundamentals on the applied electromagnetic model and the linear inverse problem in MIT are described in section 2.2.4.

The sensitivity to conductivity changes S^J (see section 3.6) and the condition of the Jacobian matrix J are analysed with respect to a spherical volume of interest (VOI) with a radius of 0.11 m. The centre of the VOI is equivalent to the centres of the rings (cylindrical setups) and hemispheres that describe the positions of the measurement and excitations coils. According to this approach, 672 nodal elements form the VOI. To set up J, conductivities are predefined with $0.2\,\mathrm{S\,m}^{-1}$ for nodes inside the VOI and with $0\,\mathrm{S\,m}^{-1}$ for outer nodes. An excitation current of 100 mA is used in these simulations.

We simulate six setups of coils in cylindrical (identified by A) and hemispherical arrangement (B). The cylindrical arrangements allow versatile applications for different types of measurements. In principle, the measurement regions can be accessed from two sides. Hemispherical MIT systems are designed particularly for the measurement of spherical and hemispherical objects, such as the human head.

The setups identified by A1 and B1 exist as hardware devices, developed by Philips Research, Aachen, Germany. The cylindrical setup A1 contains one ring with 16 excitation and measurement coils. Setup A2 is in accordance with A1 but uses larger excitation coils. Similarly, the setup A3 corresponds to A1 but uses larger measurement coils. A detailed description of the MIT system represented by A1 is given by Vauhkonen et al. [2008].

The setup B1 emulates a newer hemispherical MIT system that utilizes 31 pairs of coils with smaller radii for the excitation and measurement. B2 describes a hemispherical coil arrangements similar to B1 with 16 pairs of coils of the same size.

Table 4.6.: Coil parameters for the cylindrical (A1–A3) and hemispherical (B1–B3) MIT setups.

Setup	Pairs of coils	Radii of coils (in m)	Areas of coils (in m^2)
A1	16	0.025	0.0020
A2	16	excitation: 0.060	0.0113
		measurement: 0.025	0.0020
A3	16	excitation: 0.025	0.0020
		measurement: 0.060	0.0113
B1	31	0.016	0.0008
B2	16	0.016	0.0008
B3	30	0.03	0.0028

The setup B3 uses 30 pairs of larger coils, which cover the upper region of the VOI almost completely.

For cylindrical setups, the distance between each measurement coil and the centre of the tomography system at (0, 0, 0) is 15 cm. The excitation coils are placed in a distance of 15.7 cm to the centre. For hemispherical setups, the distances between the centre of the VOI and the coils are 14 cm and 14.5 cm, respectively. Details on the parameters of coils are given in Table 4.6. The arrangement of the excitation and measurement coils together with the VOI are illustrated in Figure 4.16.

Plots of logarithmic distributions $\log_{10} S_i^J$ for elements i within the X = 0 plane of the VOI are used to illustrate the sensitivities of the MIT setups. Moreover, we compute the median of S^J using all elements in the spherical VOI. The condition of J is quantified by means of $\kappa^k(J)$ and $\rho^k(J)$, both are applied relatively to the singular value with index $k = 128$ (see section 3.5). This particular selection of k is related to truncation thresholds, which typically provide adequate TSVD and Tikhonov-Phillips solutions of linear inverse problems using real measurement data of the MIT system represented by A1.

In one example, we qualitatively characterize the decay of the sensitivity for the setup A1 using finite elements with increasing distances to the coils. In this simulation, we use an EFEM model with tetrahedral elements of homogeneous volume, in which six nodal elements form a cube with an edge length of 1 cm. This results in tetrahedral elements with volumes of $0.167\,\mathrm{cm}^3$, which is 1/8 of the element volumes we use to plot the sensitivity distributions. The values of S^J are computed for $n = 15$ elements that are distributed along the Y-axis between the measurement coil at (0, −0.1495, 0) and the centre of the tomography system. This leads to coil-element distances between 2.5 and 14.5 cm. To model the decay of sensitivity, parameters a and b are fitted to the exponential function

$$f_{ab}^J(x) := a\, e^{b\, x}\,, \tag{4.14}$$

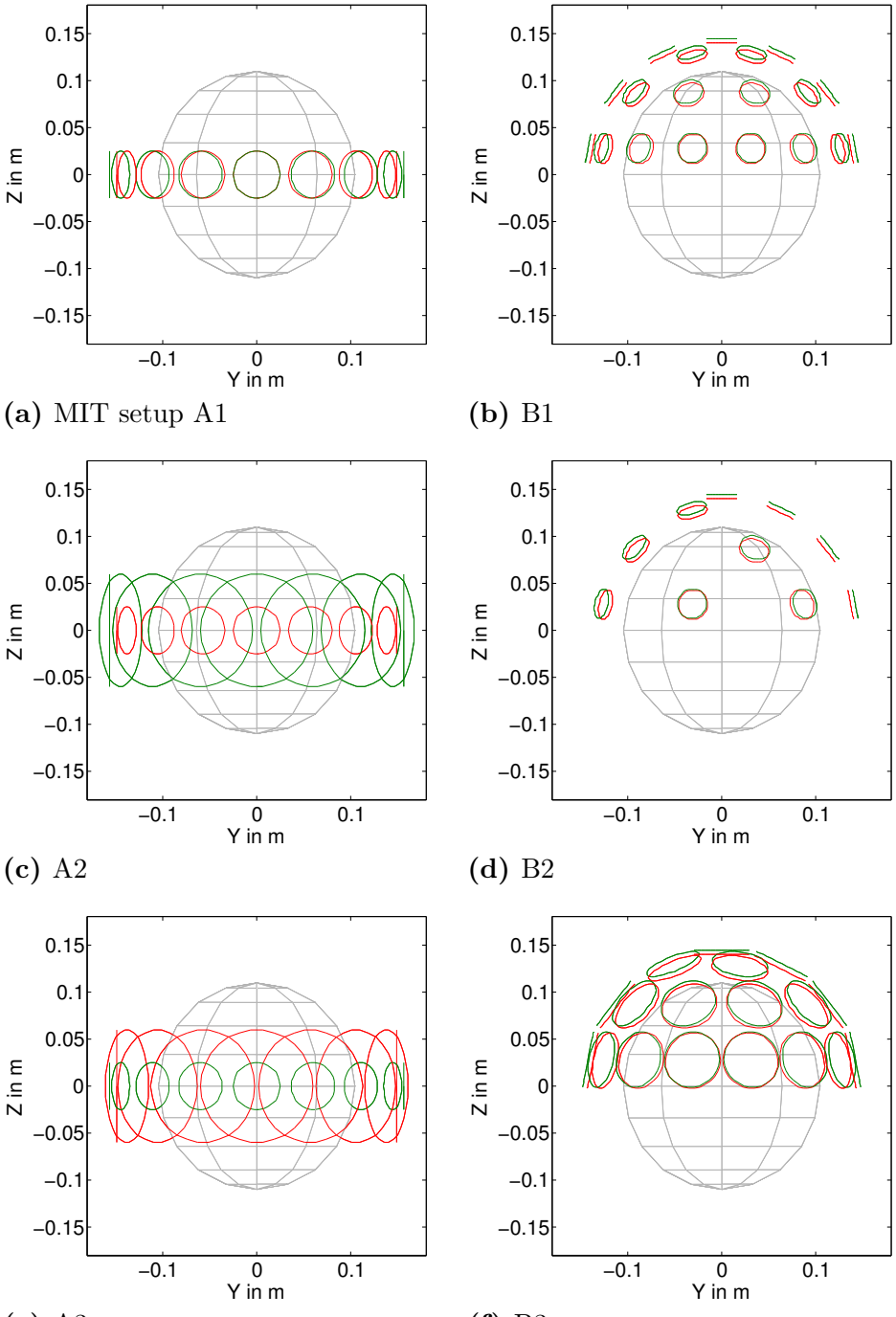

(a) MIT setup A1 **(b)** B1

(c) A2 **(d)** B2

(e) A3 **(f)** B3

Figure 4.16.: Illustration of the arrangement of excitation (outer green circles) and measurement (inner red circles) coils of the emulated cylindrical (left images) and hemispherical (right images) MIT setups. The VOIs are indicated by the spheres.

using the optimization method of Nelder and Mead [1965]. The objective function for the optimization is defined with

$$\Delta^J(a,b) := \left[\frac{1}{n}\sum_i \left(\frac{f_{ab}^J(x_i) - S_i^J}{S_i^J}\right)^2\right]^{1/2}, \tag{4.15}$$

where x_i is the coil-element distance and S_i^J is the sensitivity to conductivity changes of the ith element.

4.5.3. Results

The plots of the logarithmic sensitivity distribution in the plane of Y = 0 are given in Figure 4.17. All subfigures indicate a strong decay of the sensitivity by several orders of magnitude from regions close to the coils towards the centre of the VOI. The hemispherical setups provide in the upper part of the VOI considerably higher sensitivities than cylindrical setups. However, the cylindrical coil arrangements show better sensitivities in the lower and lower central parts of the VOI. In general, the setups with larger coils provide higher absolute values and a reduced decay of the sensitivity compared with similar setups using coils of smaller area.

Results for the median(S^J), $\kappa^{128}(J)$, and $\rho^{128}(J)$ are shown in Table 4.7. The enlargement of the excitation coils in setup A2 compared with A1 results in small improvements of the median of the sensitivity and the measures of condition, κ^{128} and ρ^{128}. By increasing the size of the measurement coils in A3, the median sensitivity is considerably increased compared with A1 and A2. The condition of J for A3 is similar to A2 and better than for A1. With the lower number of coils in B2 compared with B1, a worse median sensitivity and a clear deterioration of the condition can be observed. By using only 16 instead of 31 coils, the setup B2 shows the weakest performance of all reviewed setups. In contrast, the setup B3 provides a superior sensitivity and condition, in which the mean sensitivity is by two and κ is by three orders of magnitude improved regarding the setup B1. Overall, the results for A1–B3 in Table 4.7 tally with the outcomes in Figure 4.17.

Figure 4.18 illustrates for setup A1 the decay of sensitivity together with the fitted function f^J. The fit of sensitivity values S^J to f_{ab}^J results in parameters $a = 4.6 \times 10^{-8}$ and $b = -215.6$ with

$$f^J(x) = 4.6 \times 10^{-8}\, e^{-215.6\, x}\,,$$

for element-coil distances x, where x is between 0.025 and 0.145 m. The sensitivity values are clearly smaller when using finite elements with volumes of 0.167 cm^3 instead of 1.333 cm^3. For comparison, refer also the subfigure 4.17a, which illustrates the sensitivity for the setup A1 in the X = 0 plane, using elements with volumes of 1.333 cm^3.

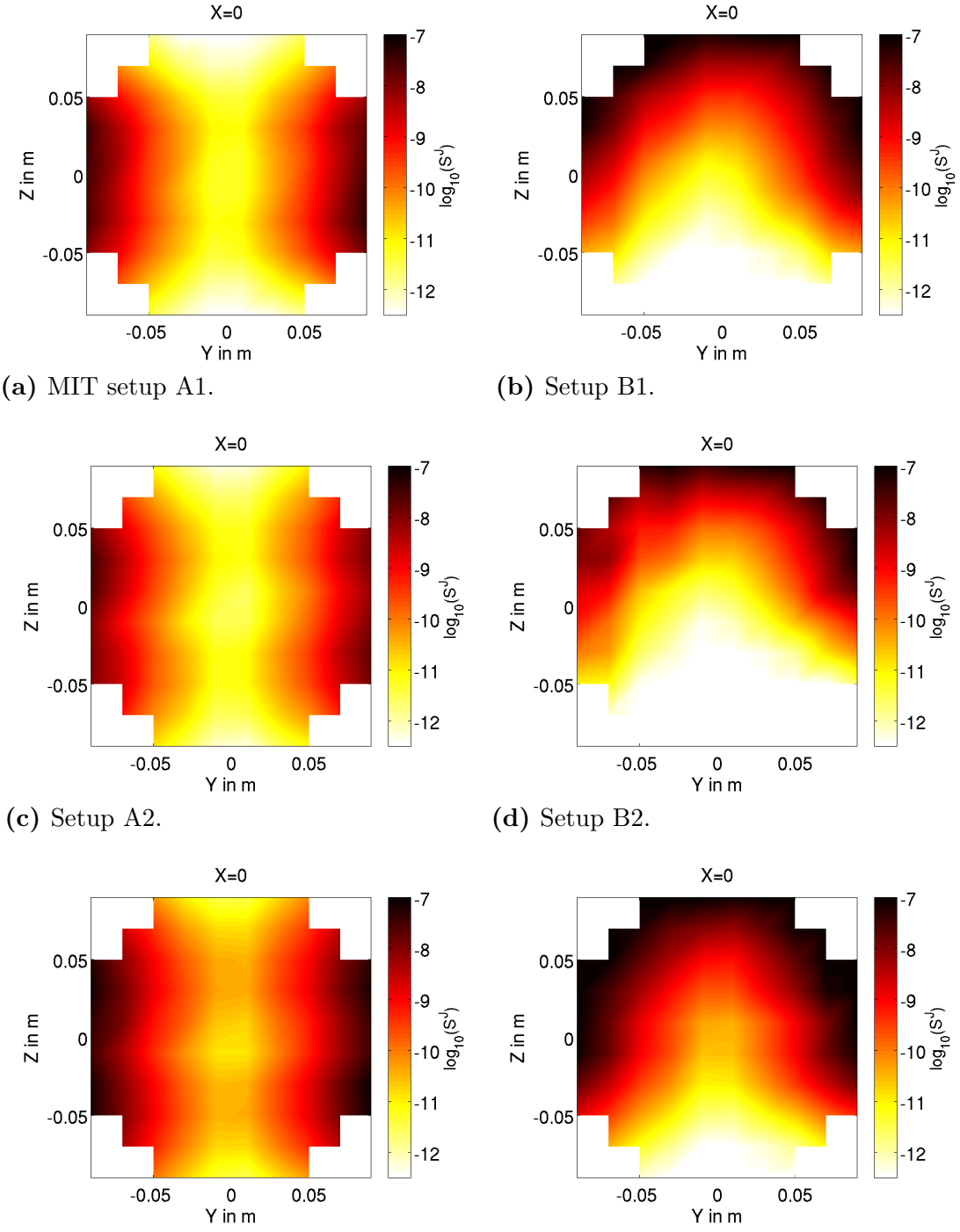

(a) MIT setup A1.

(b) Setup B1.

(c) Setup A2.

(d) Setup B2.

(e) Setup A3.

(f) Setup B3.

Figure 4.17.: Plots of interpolated logarithmic sensitivity distributions in the plane of X = 0 for cylindrical (A1–A3, left column) and hemispherical (B1–B3, right column) MIT setups. Darker colours indicate higher sensitivities.

Table 4.7.: Values of κ^{128}, ρ^{128}, and median(S^J) for cylindrical (A1–A3) and hemispherical (B1–B3) MIT setups. Larger values of median(S^J) and smaller values of κ and ρ indicate better results.

Setup	median(S^J)	$\kappa^{128}(J)$	$\rho^{128}(J)$
A1	2.53×10^{-10}	7.1×10^{4}	16.53
A2	3.32×10^{-10}	1.4×10^{4}	13.62
A3	1.78×10^{-9}	1.2×10^{4}	13.96
B1	5.88×10^{-10}	2.2×10^{3}	24.86
B2	9.59×10^{-11}	2.1×10^{5}	47.79
B3	4.16×10^{-9}	4.4×10^{2}	10.63

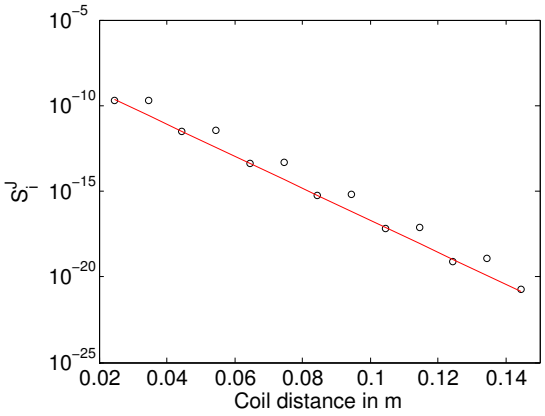

Figure 4.18.: Logarithmic plot of the sensitivity values S^J for nodal elements ($\circ$) located along the Y-axis for the setup A1. The fitted exponential function f^J is indicated by the thin red line.

4.5.4. Discussion and Conclusions

Owing to the spatial distribution of the coils and the definition of the spherical VOI, hemispherical setups provide higher sensitivities than cylindrical setups in the upper VOI, whereas the cylindrical coil setups show better values of the sensitivity in the lower regions. The question whether coils should be arranged in a hemispherical or cylindrical shape basically depends on the considered application and on the typical shape and size of the measurement objects. For stroke classification and the measurement of spherical objects, such as the human head, hemispherical arrangements are advantageous. For general applications and the examination of arbitrary objects, cylindrical setups provide a higher degree of flexibility.

An increase of the total coil area of an MIT system, taking the number and the area of coils into account, leads to considerable enhancements of the sensitivity and the condition. The benefits when enlarging the measurement coils are clearly

higher compared with the enlarging of the excitation coils, which can be explained by the weakness of the secondary magnetic fields. When coils are arranged in pairs the measurement coils should be placed closer to the measurement object than the excitation coils. As indicated by these simulations, the measurement part of MIT systems is more critical to the sensitivity than the excitation part.

This study evaluates only some variations of the parameters for the areas and numbers of coils by considering two typical schemes of cylindrical and hemispherical arrangements. Further parameters, such as the excitation current, the frequency, the number of coil windings, and the distance between coils and the VOI were not in the focus of this section but influence the sensitivity and condition as well.

Adaptations to improve the sensitivity of MIT setups often underlie technical restrictions or require further adjustments to the system, which can result in a significant increase of the costs. Since the large coils of the MIT systems A2 and A3 are each pairwise intersecting, a practical realization of both systems need minor adaptations. One possibility consists in shifting every second pair of coils several millimetre inwards to avoid the intersection of coil loops, which slightly affects the sensitivity, too.

The decay of the sensitivity S^J, which we quantified for setup A1, can be well approximated by an exponential function. The non-continuity of S^J for every second element (see Figure 4.18) can be explained by the particular EFEM model with asymmetrically distributed edge elements and coils. The exponential decay of the sensitivity and the high absolute value of the exponential factor b can lead to fundamental difficulties in practice. Such difficulties can arise within the development of MIT systems, when performing measurements by magnetic induction, and when estimating conductivity changes by solving the linear inverse problem. As shown by the plots of the logarithmic sensitivities in Figure 4.17, the decay of sensitivity can be reduced, for example by using measurement coils of larger area. Since we use volume elements to model the VOI, the sensitivity also depends on the respective element volume. In general, finite elements with larger volumes improve the sensitivity but decrease the spatial accuracy and increase numerical errors. Further investigation that focus on the effects of the size, the shape, and the distribution of finite elements on the sensitivity are important.

5 Conclusions

We aim to reduce the effects of noise and errors on the linear inverse solution by improving the condition of the problem and to increase the sensitivity of measurement setups. Different methodologies to assess the condition and sensitivity are presented. We propose a new measure of condition ρ that quantifies the ratio of the largest and the mean singular value of kernel matrices. In our examinations, the principal outcomes for ρ and the standard condition number κ agree or differ only inconsiderably. By assessing the differences in the scale of singular values, both measures indicate a potential amplification of noise and errors in the inverse solutions.

The condition number κ can be considerably affected by numerical errors that arise during its computation. The resulting values of κ may not exceed the inverse of the floating-point relative accuracy significantly, even if the true values of κ are much larger. However, if we minimize κ in an optimization process or if we focus on relatively small values, then numerical errors in κ are also small and likely to be negligible. Furthermore, the strong dependency of κ on the smallest singular value should be taken into account, when evaluating the condition. Since ρ includes information on all singular values of the kernel matrix, the influence of the smallest singular value is reduced; in addition, the numerical stability of the computation is increased. When solving linear inverse problems, the utilization of regularization methods is typically required to improve the condition by eliminating or attenuating the influence of small singular values on the solution. To consider a specific TSVD truncation threshold, the condition can be evaluated with respect to the corresponding singular value.

The proposed tabu search algorithm improves the condition of sensor arrangements by selecting an optimal subset of sensors with minimum condition number. To reduce the search space for the tabu search optimization, the sensor directions can also be set directly. For example, the directions can be set perpendicularly to the surface of the measurement object, aligned to the closest source, or oriented toward the strongest gradient.

To improve the condition of linear inverse problems in magnetic nanoparticle imaging, we adapt the parameters that define the source space grid. The results

of this study suggest that the area of sources should slightly extend the sensor area. If more sensors than sources are considered in the corresponding linear inverse problems, then the defined number of sources has a significant influence on the condition. Because EEG and MEG use considerably different arrangements of sensors and spatial distributions of sources, further investigations are relevant for these applications.

Furthermore, we show for generic examples of planar mono-axial sensor arrays that random variations in the sensor directions provide a better condition compared with uniformly oriented sensors. So far, all tested configurations representing typical 2D or 3D arrangements of sources and arrays with one or more planes of mono-axial sensor layers indicate benefits of direction variations for the condition. Ongoing research tries to show general benefits of non-uniform sensor orientations for typical arrays of mono-axial sensors. The study also indicates improvements of the condition when the sensor Z-positions are varying in a small range. Further examinations of the effects of variations in the sensor direction and positions could focus on axial and planar gradiometers, on sensors that integrate magnetometers and gradiometers [see, for example Ahonen et al. 1993], and on non-planar arrangements of sensors.

By using simple examples of linear inverse problems, we demonstrate the effects of an improved condition on the quality of inverse solutions. The examples attest that solutions are less affected by errors and noise when the condition is improved in terms of κ and ρ. To evaluate the benefits of an improved condition in a particular application, more realistic examples and representations of noise are recommended.

Moreover, we evaluate the sensitivity of MIT systems as a first step towards the optimization of coil arrangements with respect to the sensitivity and condition. To optimally place coils for measuring electrical conductivity changes in particular regions, the proposed tabu search algorithm can prospectively be applied. The challenges of such improvements of MIT systems are the substantial practical restrictions, which are in particular caused by the high frequency currents and magnetic fields. The described approach, although simple, already provides important insights into the features and limitations regarding the sensitivity of MIT systems. In further works, the assessment of the sensitivity is used for the evaluation of single excitation and measurement coils. Simulation studies using one excitation coil were presented, for example by Rosell et al. [2001] and Scharfetter et al. [2005] by deploying slightly different definitions of the sensitivity. To the best of my knowledge, no other publications that focuses on the comprehensive evaluation of the sensitivity for multi-channel MIT systems exist to date, besides our study [Eichardt et al. 2009b]. Because of the observed rapid decay of the sensitivity in MIT, further research supporting its improvement are crucially important.

The presented methods and strategies facilitate substantial improvements of the condition in magnetic applications. The arrangement of sensors relative to the measurement object is particularly critical to the condition of linear inverse problems and to the quality of inverse solutions. Configurable sensor arrays would have great utility, especially in biomedical applications. Moreover, the methods of this thesis can be applied to improve the condition and the sensitivity in various fields.

Appendix

A

Effects of Predefining Source Directions on the Condition

A.1. Introduction

We consider linear inverse problems in applications, where the directions of dipolar sources are known in advance. For example, when estimating the distribution of nanoparticles from magnetic remanence measurements, only the particles that exhibit magnetization patterns in direction of the previously applied excitation field are of interest, since relaxed particles do not significantly contribute to the measurement signal. By predefining the directions of sources contained in the lead field L, the number of columns of L and unknowns in p are reduced by a factor of 2/3.

By speculation, a smaller amount of unknown sources could improve the condition when the number of measurements is constant. Therefore, our objective is to compare the condition of lead field matrices L^3 providing arbitrary source directions (three dipoles per source position) with lead fields L^1 providing predefined source directions (one dipole per position).

A.2. Methods

We examine five examples of source space grids with source positions corresponding to Table A.1. Moreover, we use the PTB sensor system in configurations with 114, 190, 247, and 304 SQUID sensors and the AtB Argos 200 system with 195 sensors. The sensor arrays correspond to section 4.3; the applied source space grids are similar to section 4.4.

Magnetostatic lead field matrices are created for each combination of source space grid and sensor system. First, three orthogonally oriented dipoles are placed at each of the source positions to create a lead field L^3 that allows arbitrary source directions. Second, a lead field L^1 is created, which contains at each source position one dipole directed toward +Z . Corresponding to the results of section 4.3, the +Z direction provides an optimal condition of L^1. Lead fields L^3 and L^1 exhibit identical number

Table A.1.: Parameters that define the positions of the sources for appendix A.

Source grid	Source positions (X, Y, Z) min	max	Number of source pos. ($X \times Y \times Z$)
1	$-(0.14, 0.14, 0.06)$	$(0.14, 0.14, -0.06)$	$10 \times 10 \times 1 = 100$
2	$-(0.14, 0.14, 0.06)$	$(0.14, 0.14, -0.06)$	$15 \times 15 \times 1 = 225$
3	$-(0.14, 0.14, 0.15)$	$(0.14, 0.14, -0.06)$	$8 \times 8 \times 3 = 192$
4	$-(0.14, 0.14, 0.21)$	$(0.14, 0.14, -0.06)$	$15 \times 15 \times 6 = 1350$
5	$-(0.14, 0.14, 0.05)$	$(0.14, 0.14, -0.05)$	$20 \times 20 \times 1 = 400$

of rows but L^3 has three times the number of columns compared with L^1.

We evaluate the condition of L in terms of κ and ρ. To measure the degree of determination of a linear inverse problem, we define the *relative determination* of $L \in \mathbb{R}^{m \times n}$ by

$$rd(L) := \frac{m-n}{m+n}\,. \tag{A.1}$$

Values of $-1 < rd(L) < 0$ imply underdetermined and $0 < rd(L) < 1$ overdetermined linear inverse problems (see section 2.2.2).

A.3. Results

The individual results of κ, ρ, and the corresponding values of rd are shown in Table A.2. Improvements of κ when applying L^1 instead of L^3 can only be observed for 6 of 25 combinations of sensor arrays and source grids. In these cases, the linear inverse problem related to L^1 is clearly overdetermined with $rd(L^1) \geq 0.15$, whereas the inverse problem related to L^3 is only slightly overdetermined with $rd(L^3) = 0.01$ or underdetermined with $rd(L^3) \leq -0.1$. Thereby, κ is improved by factors between 10 to 10^7 when using L^1 instead of L^3

For the 19 further tested combinations, $\kappa(L^1)$ is slightly (source grids 3 and 4) or even articulately elevated (by a factor of 10^{11} using the source grid 3 and the sensor array 'ATB 195ch') compared with $\kappa(L^3)$.

The measure $\rho(L^1)$ is distinctly smaller than $\rho(L^3)$ for the six combinations that show improvements of κ, too. For all configurations using the source grids 1, 2, 5 and for the source grid 3 in combination with sensor arrays of ≥ 247 sensors, $\rho(L^1)$ is only marginally smaller compared with $\rho(L^3)$. For the remaining eight combinations, $\rho(L^1)$ is slightly larger than $\rho(L^3)$.

Figure A.1a illustrates the differences between $\log_{10}\kappa(L^1)$ and $\log_{10}\kappa(L^3)$ plotted against the differences in the relative determination. Significant improvements of $\kappa(L^1)$ compared with $\kappa(L^3)$ can only be observed, if $rd(L^1) - rd(L^3)$ is in the range of 0.5 or higher. However, differences of rd in this scale lead for two combinations also to better values for $\kappa(L^3)$.

Table A.2.: Results for κ, ρ, and rd for the tested 25 combinations of source grids and sensor configurations. Superior results (better condition of L^1 or L^3) for each combination are indicated by grey backgrounds.

Sensor array	$\kappa(L^3)$	$\kappa(L^1)$	$\rho(L^3)$	$\rho(L^1)$	$rd(L^3)$	$rd(L^1)$
Source grid 1, 100 source positions						
PTB 304ch	3.49×10^{11}	2.34×10^{4}	22.67	7.62	0.01	0.50
114ch	6.62×10^{3}	1.01×10^{5}	8.35	7.34	−0.45	0.07
190ch	7.70×10^{5}	3.14×10^{4}	14.27	7.56	−0.22	0.31
247ch	1.91×10^{8}	2.56×10^{4}	18.66	7.61	−0.10	0.42
ATB 195ch	5.70×10^{6}	5.90×10^{3}	12.04	6.22	−0.21	0.32
Source grid 2, 225 source positions						
PTB 304ch	3.93×10^{10}	3.74×10^{7}	23.12	17.08	−0.38	0.15
114ch	3.95×10^{3}	6.98×10^{3}	8.39	8.33	−0.71	−0.33
190ch	6.04×10^{5}	5.18×10^{6}	14.36	14.30	−0.56	−0.08
247ch	1.16×10^{8}	1.44×10^{8}	18.78	17.07	−0.46	0.05
ATB 195ch	4.36×10^{6}	1.66×10^{8}	12.15	12.01	−0.55	−0.07
Source grid 3, 192 source positions						
PTB 304ch	2.83×10^{11}	3.13×10^{9}	24.76	16.43	−0.31	0.23
114ch	3.04×10^{4}	1.14×10^{6}	8.99	9.40	−0.67	−0.25
190ch	3.94×10^{6}	2.17×10^{11}	15.37	16.10	−0.50	−0.01
247ch	6.10×10^{8}	4.29×10^{9}	20.12	16.42	−0.40	0.13
ATB 195ch	6.87×10^{6}	8.62×10^{17}	12.83	13.24	−0.49	0.01
Source grid 4, 1350 source positions						
PTB 304ch	2.41×10^{10}	2.54×10^{11}	26.50	26.97	−0.86	−0.63
114ch	4.71×10^{3}	7.80×10^{3}	9.61	9.70	−0.95	−0.84
190ch	5.54×10^{5}	2.89×10^{6}	16.43	16.64	−0.91	−0.75
247ch	1.11×10^{8}	4.95×10^{8}	21.53	21.88	−0.89	−0.69
ATB 195ch	3.50×10^{6}	2.18×10^{7}	13.71	13.72	−0.91	−0.75
Source grid 5, 400 source positions						
PTB 304ch	1.11×10^{10}	7.49×10^{10}	17.58	17.48	−0.60	−0.14
114ch	1.17×10^{3}	1.24×10^{3}	6.37	6.32	−0.83	−0.56
190ch	2.84×10^{5}	4.52×10^{5}	10.93	10.85	−0.73	−0.36
247ch	3.19×10^{7}	5.90×10^{7}	14.28	14.20	−0.66	−0.24
ATB 195ch	1.95×10^{6}	1.36×10^{7}	9.13	9.03	−0.72	−0.34

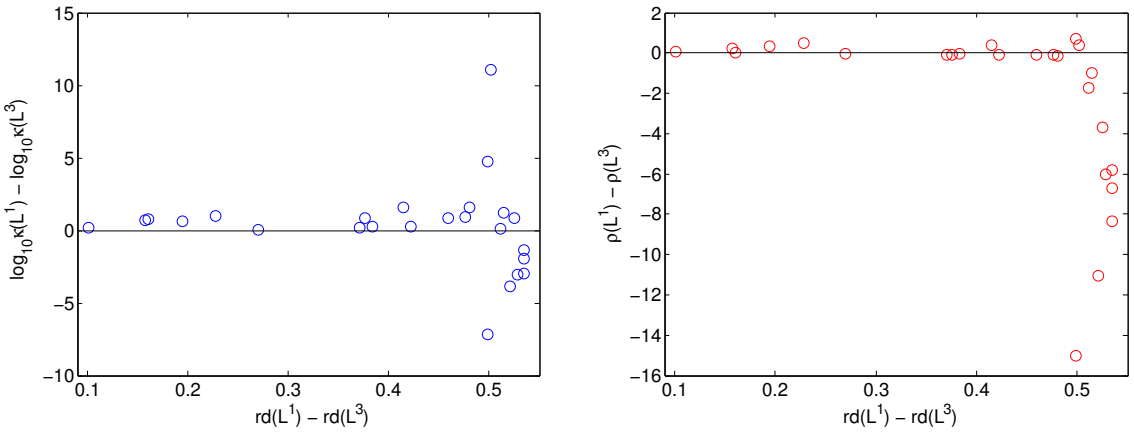

(a) Differences of logarithmic values of κ plotted against the differences of rd.

(b) Differences of ρ plotted against the differences of rd.

Figure A.1.: Effects on κ and ρ, when lead field matrices L^1 instead of L^3 are used. Markers below the horizontal lines indicate a better condition of L^1 compared with L^3.

Similarly, Figure A.1b shows the differences of $\rho(L^1) - \rho(L^3)$ plotted against $rd(L^1) - rd(L^3)$. When $rd(L^1) - rd(L^3)$ is larger 0.5, then $\rho(L^1)$ is superior to $\rho(L^3)$, too. For smaller differences of rd we observe a similar condition with $\rho(L^1) \approx \rho(L^3)$.

A.4. Discussion and Conclusions

The predefinition of the source directions does not improve the condition of lead field matrices in general. Improvements of $\kappa(L^1)$ and $\rho(L^1)$ compared with $\kappa(L^3)$ and $\rho(L^3)$ are observed when L^3 is underdetermined or marginally overdetermined and when L^1 is at the same time notably overdetermined. This finding is in the line with the simulation I of section 4.3, which indicates a considerable dependency of the condition on the number of sources solely for overdetermined problems.

Furthermore, the condition number $\kappa(L^1)$ is in 2 of 25 tested combinations of sensor arrays and source grids substantially higher than $\kappa(L^3)$. For the majority of combinations, the differences between ρ and κ are relatively small when using lead fields L^1 instead of L^3.

This evaluation also indicates that the condition number κ can be improved by increasing the number of dipoles in the source model. Prospective investigations could involve evaluations of the condition for lead fields with predefined and arbitrary source directions in EEG and MEG. In these applications, electrical current dipoles normal to the cortex surface can be assumed to reduce the number of unknown sources to be estimated.

By using correctly posed constraints for the positions and directions of the sources,

the solutions of linear inverse problems provide typically higher localization accuracies [Dale and Sereno 1993]. However, incorrect assumptions introduce model errors, which can lead to deteriorated localization results. With respect to our example, the localization errors can be considerably higher for incorrectly predefined source directions compared with source spaces that facilitate arbitrary directions. A comprehensive study on this issue for MEG beamformers was presented by Hillebrand and Barnes [2003]. The influence of inaccuracies in the source model on the localization error for magnetic nanoparticle imaging should be investigated in a further study.

B Linear Algebra Adjunct

B.1. General Remarks

This chapter collects general facts from linear algebra that are helpful when dealing with linear inverse problems. Comprehensive information can be found for the most part in the textbooks of Golub and van Loan [1996] and Hogben [2007]. Further facts and proofs on matrix theory are given by Bernstein [2009].

B.2. Singular Value Decomposition

The SVD of a matrix $A \in \mathbb{R}^{m \times n}$ is given by [Golub and Kahan 1965]

$$A = U \Sigma V^T \tag{B.1}$$

with

$$U = (u_1, \ldots, u_m) \in \mathbb{R}^{m \times m}\,, \tag{B.2}$$
$$V = (v_1, \ldots, v_n) \in \mathbb{R}^{n \times n}\,, \tag{B.3}$$
$$U^T = U^{-1} \quad \text{and} \quad V^T = V^{-1}\,, \tag{B.4}$$
$$\Sigma = \operatorname{diag}(\sigma_1, \ldots, \sigma_s) \in \mathbb{R}^{m \times n}\,, \tag{B.5}$$
$$\infty > \sigma_i \geq \sigma_{i+1} \geq 0\,. \tag{B.6}$$

The index $s := \min(m, n)$ denotes the total number of singular values σ of A, also including values of 0. The rank r is determined by the number of singular values with $\sigma_i > 0$.

B.3. Moore-Penrose Inverse

The Moore-Penrose inverse of A is defined corresponding Penrose [1955] by the unique matrix A^+ that satisfies the four Moore-Penrose conditions

$$AA^+A = A\,, \tag{B.7}$$
$$A^+AA^+ = A^+\,, \tag{B.8}$$
$$\left(AA^+\right)^T = AA^+\,, \tag{B.9}$$
$$\left(A^+A\right)^T = A^+A \tag{B.10}$$

The term pseudo-inverse is often used synonymously for Moore-Penrose inverse. According to Golub and Kahan [1965] and Golub and Reinsch [1970], the SVD of A can be used to compute $A^+ \in \mathbb{R}^{n\times m}$ by

$$A^+ = \left(U\Sigma V^T\right)^+ = V\Sigma^+U^T \qquad \text{with}$$
$$\Sigma^+ \coloneqq \operatorname{diag}\left(1/\sigma_1, \ldots, 1/\sigma_r, 0, \ldots 0\right) \in \mathbb{R}^{n\times m}\,, \tag{B.11}$$

where $r = \operatorname{rank}(A)$. Relevant properties of A^+ are corresponding Penrose [1955], Bernstein [2009, sections 6.1.6, 6.4.12], and Björck [1996, section 1.2.5]

$$\operatorname{rank}(A) = m = n \implies A^+ = A^{-1}\,, \tag{B.12}$$
$$A = 0 \iff A^+ = 0\,, \tag{B.13}$$
$$\operatorname{rank}(A) = \operatorname{rank}(A^+) = \operatorname{rank}(AA^+) = \operatorname{rank}(A^+A)\,, \tag{B.14}$$
$$\left(A^+\right)^+ = A\,, \tag{B.15}$$
$$\operatorname{rank}(A_1) = \operatorname{rank}(A_2) = n \implies (A_1\,A_2)^+ = A_2^+\,A_1^+\,, \tag{B.16}$$
$$U^T = U^{-1} \wedge V^T = V^{-1} \implies \left(UAV^T\right)^+ = VA^+U^T\,. \tag{B.17}$$

B.4. Matrix Norms

The Frobenius norm $\|A\|_F$ and the p-norm $\|A\|_p$, with $p \geq 1$, for a matrix $A \in \mathbb{R}^{m\times n}$ are given by

$$\|A\|_F \coloneqq \left(\sum_{i=1}^{m}\sum_{j=1}^{n} |A[i,j]|^2\right)^{1/2} \qquad \text{and} \tag{B.18}$$

$$\|A\|_p \coloneqq \sup_{x\neq 0} \frac{\|Ax\|_p}{\|x\|_p}\,, \tag{B.19}$$

with the vector norm

$$\|x\|_p = \left(\sum_i |x[i]|^p\right)^{1/p}\,. \tag{B.20}$$

According Golub and van Loan [1996, section 2.3] and Bernstein [2009, section 9.2], the following properties hold for Frobenius and p-norms

$$\|A\| = 0 \iff A = \mathit{0}\,, \tag{B.21}$$
$$\|A\| > 0 \iff A \neq \mathit{0}\,, \tag{B.22}$$
$$\forall l \in \mathbb{R}\colon\ \|lA\| = |l|\ \|A\|\,, \tag{B.23}$$
$$\|A_1 + A_2\| \leq \|A_1\| + \|A_2\|\,, \tag{B.24}$$
$$\|A\|_2 \leq \|A\|_F \leq r^{1/2}\,\|A\|_2\,, \tag{B.25}$$
$$\|A\|_2 = \sigma_1(A)\,, \tag{B.26}$$
$$\|A^+\|_2 = \sigma_s(A)^{-1}\,, \tag{B.27}$$
$$\|A\|_F = \left(\sum_{i=1}^{s} \sigma_i(A)^2\right)^{1/2}\,, \tag{B.28}$$
$$\|A^+\|_F = \left(\sum_{i=1}^{s} \sigma_i(A)^{-2}\right)^{1/2}\,, \tag{B.29}$$
$$\|A\|_\infty = \max_{1\leq i\leq m} \sum_{j=1}^{n} |A[i,j]|\ . \tag{B.30}$$

In this context, $\|\cdot\|$ represents the norms $\|\cdot\|_p$ or $\|\cdot\|_F$, σ_s is the smallest singular value, and r is the rank of A.

Bibliography

A. I. Ahonen, M. S. Hämäläinen, M. J. Kajola, J. E. T. Knuutila, P. P. Laine, O. V. Lounasmaa, L. Parkkonen, J. T. Simola, and C. D. Tesche. 122-channel squid instrument for investigating the magnetic signals from the human brain. *Physica Scripta*, T49A:198–205, 1993. doi:10.1088/0031-8949/1993/T49A/033. 68

E. Anderson, Z. Bai, C. Bischof, S. Blackford, J. Demmel, J. Dongarra, J. Du Croz, A. Greenbaum, S. Hammarling, A. McKenney, and D. Sorensen. *LAPACK Users' Guide*. Society for Industrial and Applied Mathematics, 3rd edition, 1999. URL `http://www.netlib.org/lapack/lug/`. 21

W. Andrä and H. Nowak, editors. *Magnetism in Medicine: A Handbook*. WILEY-VCH, 2nd edition, 2006. 3, 7

Y. Barrell and H. W. L. Naus. Detection and localisation of magnetic objects. *IET Science, Measurement & Technology*, 1(5):245–254, September 2007. doi:10.1049/iet-smt:20060129. 2

G. Baule and R. McFee. Detection of the magnetic field of the heart. *American Heart Journal*, 66(1):95–96, July 1963. doi:10.1016/0002-8703(63)90075-9. 3

D. Baumgarten, M. Liehr, F. Wiekhorst, U. Steinhoff, P. Münster, P. Miethe, L. Trahms, and J. Haueisen. Magnetic nanoparticle imaging by means of minimum norm estimates from remanence measurements. *Medical and Biological Engineering and Computing*, 46(12):1177–1185, 2008. doi:10.1007/s11517-008-0404-1. 2

D. S. Bernstein. *Matrix Mathematics*. Princeton University Press, 2nd edition, 2009. 77, 78, 79

O. Bíró. Edge element formulations of eddy current problems. *Computer Methods in Applied Mechanics and Engineering*, 169(3–4):391–405, 1999. doi:10.1016/S0045-7825(98)00165-0. 13

G. Bison, R. Wynands, and A. Weis. Dynamical mapping of the human cardiomagnetic field with a room-temperature, laser-optical sensor. *Optics Express*, 11(8):904–909, April 2003. doi:10.1364/OE.11.000904. 8

Å. Björck. *Numerical Methods for Least Squares Problems*. Society for Industrial and Applied Mathematics, 1996. 14, 78

A. L. Bloom. Principles of operation of the rubidium vapor magnetometer. *Applied Optics*, 1(1):61–68, January 1962. doi:10.1364/AO.1.000061. 8

H. Brauer, J. Haueisen, M. Ziolkowski, U. Tenner, and H. Nowak. Reconstruction of extended current sources in a human body phantom applying biomagnetic measuring techniques. *IEEE Transactions on Magnetics*, 36(4):1700–1705, July 2000. doi:10.1109/20.877770. 44

P. Bruzzone, A. Formisano, and R. Martone. Optimal magnetic probes location for current reconstruction in multistrands superconducting cables. *IEEE Transactions on Magnetics*, 38(2):1057–1060, March 2002. doi:10.1109/20.996271. 35, 55

J. Clark and A. I. Braginski, editors. *The SQUID Handbook*, volume I: Fundamentals and Technology of SQUIDs and SQUID Systems. WILEY-VCH, 2004. 7

J. Clark and A. I. Braginski, editors. *The SQUID Handbook*, volume II: Applications of SQUIDs and SQUID Systems. WILEY-VCH, 2006. 3, 7, 12

D. Cohen. Magnetoencephalography: evidence of magnetic fields produced by alpha rhythm currents. *Science*, 161(3843):784–786, August 1968. doi:10.1126/science.161.3843.784. 7

A. Curtis, A. Michelini, D. Leslie, and A. Lomax. A deterministic algorithm for experimental design applied to tomographic and microseismic monitoring surveys. *Geophysical Journal International*, 157(2):595–606, May 2004. doi:10.1111/j.1365-246X.2004.02114.x. 24

A. M. Dale and M. I. Sereno. Improved localizadon of cortical activity by combining EEG and MEG with MRI cortical surface reconstruction: A linear approach. *Journal of Cognitive Neuroscience*, 5(2):162–176, 1993. doi:10.1162/jocn.1993.5.2.162. 75

A. Datta, M. Elwassif, F. Battaglia, and M. Bikson. Transcranial current stimulation focality using disc and ring electrode configurations: FEM analysis. *Journal of Neural Engineering*, 5(2):163–174, April 2008. doi:10.1088/1741-2560/5/2/007. 35

I. Daubechies, M. Fornasier, and I. Loris. Accelerated projected gradient method for linear inverse problems with sparsity constraints. *Journal of Fourier Analysis and Applications*, 14(5–6):764–792, 2008. doi:10.1007/s00041-008-9039-8. 18

F. A. M. Davide, C. Di Natale, and A. D'Amico. Sensor array figures of merit: definitions and properties. *Sensors and Actuators B: Chemical*, 13(1–3):327–332, May 1993. doi:10.1016/0925-4005(93)85393-O. 25

S. Demko. Condition numbers of rectangular systems and bounds for generalized inverses. *Linear Algebra and its Applications*, 78:199–206, August 1986. doi:10.1016/0024-3795(86)90024-8. 21

J. W. Demmel. On condition numbers and the distance to the nearest ill-posed problem. *Numerische Mathematik*, 51(3):251–289, 1987. doi:10.1007/BF01400115. 20, 21

J. W. Demmel. The probability that a numerical analysis problem is difficult. *Mathematics of Computation*, 50(182):449–480, April 1988. doi:10.2307/2008617. 21

J. W. Demmel. *Applied Numerical Linear Algebra*. Society for Industrial and Applied Mathematics, 1997. 20

J. W. Demmel, M. Gu, S. Eisenstat, I. Slapnicar, K. Veselic, and Z. Drmac. Computing the singular value decomposition with high relative accuracy. *Linear Algebra and its Applications*, 299(1–3):21–80, September 1999. doi:10.1016/S0024-3795(99)00134-2. 22

L. Di Rienzo and J. Haueisen. Theoretical lower error bound for comparative evaluation of sensor arrays in magnetostatic linear inverse problems. *IEEE Transactions on Magnetics*, 42(11):3669–3673, November 2006. doi:10.1109/TMAG.2006.882338. 24

L. Di Rienzo and J. Haueisen. Numerical comparison of sensor arrays for magnetostatic linear inverse problems based on a projection method. *COMPEL: The International Journal for Computation and Mathematics in Electrical and Electronic Engineering*, 26(2):356–367, 2007. doi:10.1108/03321640710727719. 24

L. Di Rienzo, J. Haueisen, and C. M. Arturi. Three component magnetic field data – impact on minimum norm solutions in a biomedical application. *COMPEL: The International Journal for Computation and Mathematics in Electrical and Electronic Engineering*, 24(3):869–881, 2005. doi:10.1108/03321640510598193. 21, 32

R. Eichardt and J. Haueisen. Influence of sensor variations on the condition of the magnetostatic linear inverse problem. In *Proceedings of the 17th Conference on the Computation of Electromagnetic Fields, 22–26 November, Florianpolis, Brazil*, pages 251–252, 2009. 27

R. Eichardt and J. Haueisen. Influence of sensor variations on the condition of the magnetostatic linear inverse problem. *IEEE Transactions on Magnetics*, 46(8): 3449–3453, 2010. doi:10.1109/TMAG.2010.2046149. 12, 27

R. Eichardt, J. Haueisen, T. R. Knösche, and E. G. Schukat-Talamazzini. Reconstruction of multiple neuromagnetic sources using augmented evolution strategies – a comparative study. *IEEE Transactions on Biomedical Engineering*, 55(2, Part 1): 703–712, February 2008. doi:10.1109/TBME.2007.912656. 10

R. Eichardt, D. Baumgarten, L. Di Rienzo, S. Linzen, V. Schultze, and J. Haueisen. Localisation of buried ferromagnetic objects based on minimum-norm-estimations – a simulation study. *COMPEL: The International Journal for Computation and Mathematics in Electrical and Electronic Engineering*, 28(5):1327–1337, 2009a. doi:10.1108/03321640910969566. 2, 49

R. Eichardt, C. H. Igney, J. Kahlert, M. Hamsch, M. Vauhkonen, and J. Haueisen. Sensitivity comparisons of cylindrical and hemi-spherical coil setups for magnetic induction tomography. In O. Dössel and W. C. Schlegel, editors, *Proceedings of the World Congress on Medical Physics and Biomedical Engineering, 7–12 September, Munich, Germany*, volume 25/IV of *IFMBE Proceedings*, pages 269–272, 2009b. doi:10.1007/978-3-642-03882-2_71. 27, 35, 68

R. Eichardt, D. Baumgarten, B. Petković, F. Wiekhorst, L. Trahms, and J. Haueisen. Adapting source grid parameters to improve the condition of the magnetostatic linear inverse problem of estimating nanoparticle distributions. In *Proceedings of the XI-th International Workshop on Optimization and Inverse Problems in Electromagnetism, 14–18 September, Sofia, Bulgaria*, 2010. 12, 27

R. Eichardt, D. Baumgarten, B. Petković, F. Wiekhorst, L. Trahms, and J. Haueisen. Adapting source grid parameters to improve the condition of the magnetostatic linear inverse problem of estimating nanoparticle distributions. Submitted. 27

H. W. Engl, M. Hanke, and A. Neubauer. *Regularization of Inverse Problem*. Kluwer Academic Publishers, 1996. 22

A. Formisano and R. Martone. Optimisation of magnetic sensors for current reconstruction. *COMPEL: The International Journal for Computation and Mathematics in Electrical and Electronic Engineering*, 22(3):535–548, 2003. doi:10.1108/03321640310474921. 55

L. Geddes and L. Baker. The specific resistance of biological material – a compendium of data for the biomedical engineer and physiologist. *Medical and Biological Engineering and Computing*, 5(3):271–293, 1967. doi:10.1007/BF02474537. 32

F. Glover. Tabu search: A tutorial. *Interfaces*, 20(4):74–94, July–August 1990. doi:10.1287/inte.20.4.74. 29

F. Glover and M. Laguna. *Tabu Search*. Kluwer Academic Publishers, 2nd edition, 1997. 29

G. H. Golub and W. Kahan. Calculating the singular values and pseudo-inverse of a matrix. *Journal of the Society for Industrial and Applied Mathematics: Series B, Numerical Analysis*, 2(2):205–224, 1965. doi:10.1137/0702016. 14, 77, 78

G. H. Golub and C. Reinsch. Singular value decomposition and least squares solutions. *Numerische Mathematik*, 14:403–420, 1970. doi:10.1007/BF02163027. 78

G. H. Golub and C. F. van Loan. *Matrix Computations*. The Johns Hopkins University Press, 3rd edition, 1996. 14, 19, 20, 77, 79

G. H. Golub, P. C. Hansen, and D. P. O'Leary. Tikhonov regularization and total least squares. *SIAM Journal on Matrix Analysis and Applications*, 21(1):185–194, October 1999. doi:10.1137/S0895479897326432. 1999. 16

I. F. Gorodnitsky, J. S. George, and B. D. Rao. Neuromagnetic source imaging with FOCUSS: a recursive weighted minimum norm algorithm. *Electroencephalography and Clinical Neurophysiology*, 95(4):231–251, 1995. doi:10.1016/0013-4694(95)00107-A. 18

B. M. Graham and A. Adler. Electrode placement configurations for 3D EIT. *Physiological Measurement*, 28(7):S29–S44, June 2007. doi:10.1088/0967-3334/28/7/S03. 35

H. Griffiths. Magnetic induction tomography. *Measurement Science and Technology*, 12(8):1126–1131, August 2001. doi:10.1088/0957-0233/12/8/319. 3

D. Gürsoy and H. Scharfetter. The effect of receiver coil orientations on the imaging performance of magnetic induction tomography. *Measurement Science and Technology*, 20(10):105505, pp. 1–9, September 2009. doi:10.1088/0957-0233/20/10/105505. 35

J. Hadamard. Sur les problèmes aux dérivées partielles et leur signification physique. *Princeton University Bulletin*, 13:49–52, 1902. 10

M. S. Hämäläinen and R. J. Ilmoniemi. Interpreting measured magnetic fields of the brain: Estimates of current distributions. Technical Report TKK-F-A559 (1984), Low Temperature Laboratory, Helsinki University of Technology, December 1984. 11

M. S. Hämäläinen and R. J. Ilmoniemi. Interpreting measured magnetic fields of the brain: Minimum norm estimates. *Medical and Biological Engineering and Computing*, 32(1):35–42, January 1994. doi:10.1007/BF02512476. 11

P. C. Hansen. Analysis of discrete ill-posed problems by means of the L-curve. *SIAM Review*, 34(4):561–580, December 1992. doi:10.1137/1034115. 17, 45

P. C. Hansen. *Rank-Deficient and Discrete Ill-posed Problems*. Society for Industrial and Applied Mathematics, 1998. 15, 16, 17

R. J. Hanson. A numerical method for solving Fredholm integral equations of the first kind using singular values. *SIAM Journal on Numerical Analysis*, 8(3):616–622, September 1971. doi:10.1137/0708058. 15

J. Haueisen, J. Schreiber, H. Brauer, and T. R. Knösche. Dependence of the inverse solution accuracy in magnetocardiography on the boundary-element discretization. *IEEE Transactions on Magnetics*, 38(2):1045–1048, March 2002. doi:10.1109/20.996268. 32

P. W. Hawkes, editor. *Advances in Electronics and Electron Physics*, volume 75. Academic Press, 1989. 10

M. Hermann. *Numerische Mathematik*. Oldenbourg Wissenschaftsverlag, 2001. 21

D. J. Higham. Condition numbers and their condition numbers. *Linear Algebra and its Applications*, 214:193–213, January 1995. doi:10.1016/0024-3795(93)00066-9. 20, 21

N. J. Higham. *Accuracy and Stability of Numerical Algorithms*. Society for Industrial and Applied Mathematics, 1996. 14

B. Hilgenfeld and J. Haueisen. Simultaneous suppression of disturbing fields and localization of magnetic markers by means of multipole expansion. *BioMagnetic Research and Technology*, 2(6):1–8, September 2004. doi:10.1186/1477-044X-2-6. 2

A. Hillebrand and G. R. Barnes. The use of anatomical constraints with MEG beamformers. *NeuroImage*, 20(4):2302–2313, December 2003. doi:10.1016/j.neuroimage.2003.07.031. 75

L. Hogben, editor. *Handbook of Linear Algebra*. Chapman & Hall / CRC, 2007. 20, 77

C. H. Igney, S. Watson, R. J. Williams, H. Griffiths, and O. Dössel. Design and performance of a planar-array mit system with normal sensor alignment. *Physiological Measurement*, 26(5):S263–S278, April 2005. doi:10.1088/0967-3334/26/2/025. 3

C.-H. Im, H.-H. Jung, J.-D. Choi, S. Y. Lee, and K.-Y. Jung. Determination of optimal electrode positions for transcranial direct current stimulation (tDCS). *Physics in Medicine and Biology*, 53(11):N219–N225, May 2008. doi:10.1088/0031-9155/53/11/N03. 35

R. C. Jaklevic, J. Lambe, A. H. Silver, and J. E. Mercereau. Quantum interference effects in josephson tunneling. *Physical Review Letters*, 12(7):159–160, February 1964. doi:10.1103/PhysRevLett.12.159. 7

B. D. Josephson. Possible new effects in superconductive tunneling. *Physics Letters*, 1(7):251–253, July 1962. doi:10.1016/0031-9163(62)91369-0. 7

N. M. Josuttis. *The C++ Standard Library – A Tutorial and Reference*. Addison Wesley Longman, 1999. 31

D. E. Knuth. Big Omicron and big Omega and big Theta. *SIGACT News*, 8(2): 18–24, April 1976. doi:10.1145/1008328.1008329. 31

T. Köhler, M. Wagner, M. Fuchs, H.-A. Wischmann, R. Drenckhahn, and A. Theissen. Depth normalization in MEG/EEG current density imaging. In *Proceedings of the 18th Annual International Conference of the IEEE Engineering in Medicine and Biology Society, Amsterdam, The Netherlands, 31st October – 3rd November 1996*, volume 2, pages 812–813, 1996. doi:10.1109/IEMBS.1996.651989. 18

A. Korjenevsky, V. Cherepenin, and S. Sapetsky. Magnetic induction tomography: experimental realization. *Physiological Measurement*, 21(1):89–94, February 2000. doi:10.1088/0967-3334/21/1/311. 3

S. Lau, R. Eichardt, L. Di Rienzo, and J. Haueisen. Optimal vest-like magnetic sensor array for magnetocardiography. In *Proceedings of the X-th International Workshop on Optimization and Inverse Problems in Electromagnetism, 14–17 September, Ilmenau, Germany*, 2008a. 35

S. Lau, R. Eichardt, L. Di Rienzo, and J. Haueisen. Tabu search optimization of magnetic sensor systems for magnetocardiography. *IEEE Transactions on Magnetics*, 44(6):1442–1445, June 2008b. doi:10.1109/TMAG.2007.915911. 27, 32

U. Leder, J. Haueisen, M. Huck, and H. Nowak. Non-invasive imaging of arrhythmogenic left-ventricular myocardium after infarction. *The Lancet*, 352(9143):1825, December 1998. doi:10.1016/S0140-6736(98)00082-8. 3

U. Leder, J. Haueisen, P. Pohl, F.-M. Malur, J.-P. Heyne, V. Baier, and H. Figulla. Methods for the computational localization of atrio-ventricular pre-excitation syndromes. *The International Journal of Cardiovascular Imaging*, 17(2):153–160, 2001. doi:10.1023/A:1010606030369. 3

F. London. *Superfluids*, volume 1 - Macroscopic Theory of Superconductivity. John Wiley & Sons, 1950. 7

R. L. Lux, C. R. Smith, R. F. Wyatt, and J. A. Abildskov. Limited lead selection for estimation of body surface potential maps in electrocardiography. *IEEE Transactions on Biomedical Engineering*, BME-25(3):270–276, May 1978. doi:10.1109/TBME.1978.326332. 29

J. E. McFee, Y. Das, and R. O. Ellingson. Locating and identifying compact ferrous objects. *IEEE Transactions on Geoscience and Remote Sensing*, 28(2):182–193, March 1990. doi:10.1109/36.46697. 2

R. Merwa, K. Hollaus, B. Brandstätter, and H. Scharfetter. Numerical solution of the general 3D eddy current problem for magnetic induction tomography (spectroscopy). *Physiological Measurement*, 24(2):545–554, May 2003. doi:10.1088/0967-3334/24/2/364. 13

B. J. Messinger-Rapport and Y. Rudy. Regularization of the inverse problem in electrocardiography: A model study. *Mathematical Biosciences*, 89(1):79–118, 1988. doi:10.1016/0025-5564(88)90113-7. 16

A. Morris, H. Griffiths, and W. Gough. A numerical model for magnetic induction tomographic measurements in biological tissues. *Physiological Measurement*, 22(1): 113, February 2001. doi:10.1088/0967-3334/22/1/315. 13

M. Nalbach and O. Dössel. Comparison of sensor arrangements of MCG and ECG with respect to information content. *Physica C: Superconductivity*, 372–376, part 1: 254–258, August 2002. doi:10.1016/S0921-4534(02)00683-4. 22

B. K. Natarajan. Sparse approximate solutions to linear systems. *SIAM Journal on Computing*, 24(2):227–234, April 1995. doi:10.1137/S0097539792240406. 18

J. A. Nelder and R. Mead. A simplex method for function minimization. *The Computer Journal*, 7(4):308–313, January 1965. URL `http://comjnl.oxfordjournals.org/content/7/4/308`. 10, 40, 62

J. Nenonen, M. Mäkijärvi, L. Toivonen, K. Forsman, M. Leiniö, J. Montonen, A. Järvinen, P. Keto, P. Hekali, T. Katila, and P. Siltanen. Non-invasive magnetocardiographic localization of ventricular pre-excitation in the Wolff-Parkinson-White syndrome using a realistic torso model. *European Heart Journal*, 14(2): 168–174, 1993. URL `http://eurheartj.oxfordjournals.org/content/14/2/168.full.pdf+html`. 3

J. Netz, E. Forner, and S. Haagemann. Contactless impedance measurement by magnetic induction – a possible method for investigation of brain impedance. *Physiological Measurement*, 14(4):463–471, November 1993. doi:10.1088/0967-3334/14/4/007. 3

R. Penrose. A generalized inverse for matrices. *Proceedings of the Cambridge Philosophical Society*, 51:406–413, 1955. doi:10.1017/S0305004100030401. 14, 78

M. H. Pham and A. J. Peyton. Computation of 3-D sensitivity coefficients in magnetic induction tomography using boundary integral equations and radial basis functions. *IEEE Transactions on Magnetics*, 44(10):2268–2276, October 2008. doi:10.1109/TMAG.2008.2001989. 25, 59

D. L. Phillips. A technique for the numerical solution of certain integral equations of the first kind. *Journal of ACM*, 9(1):84–97, January 1962. doi:10.1145/321105.321114. 16

J. W. Phillips, R. M. Leahy, and J. C. Mosher. MEG-based imaging of focal neuronal current sources. *IEEE Transactions on Medical Imaging*, 16(3):338–348, June 1997. doi:10.1109/42.585768. 18

N. Polydorides and H. McCann. Electrode configurations for improved spatial resolution in electrical impedance tomography. *Measurement Science and Technology*, 13(12):1862–1870, November 2002. doi:10.1088/0957-0233/13/12/309. 35

P. Ripka, editor. *Magnetic Sensors and Magnetometers*. Artech House, 2001. 8

J. Rosell, R. Casañas, and H. Scharfetter. Sensitivity maps and system requirements for magnetic induction tomography using a planar gradiometer. *Physiological Measurement*, 22(1):121–130, February 2001. doi:10.1088/0967-3334/22/1/316. 68

L.-L. Rouve, L. Schmerber, O. Chadebec, and A. Foggia. Optimal magnetic sensor location for spherical harmonic identification applied to radiated electrical devices. *IEEE Transactions on Magnetics*, 42(4):1167–1170, April 2006. doi:10.1109/TMAG.2006.872016. 21

S. M. Rump. Ill-conditioned matrices are componentwise near to singularity. *SIAM Review*, 41(1):102–112, March 1999. doi:10.1137/S0036144598323216. 20

H. Scharfetter, R. Merwa, and K. Pilz. A new type of gradiometer for the receiving circuit of magnetic induction tomography (MIT). *Physiological Measurement*, 26(2): S307–S318, April 2005. doi:10.1088/0967-3334/26/2/028. 68

H. Scharfetter, A. Köstinger, and S. Issa. Hardware for quasi-single-shot multifrequency magnetic induction tomography (MIT): the Graz Mk2 system. *Physiological Measurement*, 29(6):S431–S443, June 2008. doi:10.1088/0967-3334/29/6/S36. 3

A. Schnabel, M. Burghoff, S. Hartwig, F. Petsche, U. Steinhoff, D. Drung, and H. Koch. A sensor configuration for a 304 SQUID vector magnetometer. *Neurology and Clinical Neurophysiology*, 70:1–5, November 2004. URL `http://www.neurojournal.com/article/view/284`. 8

A. Sheinker, L. Frumkis, B. Ginzburg, N. Salomonski, and B.-Z. Kaplan. Magnetic anomaly detection using a three-axis magnetometer. *IEEE Transactions on Magnetics*, 45(1):160–167, January 2009. doi:10.1109/TMAG.2008.2006635. 2

A. H. Silver and J. E. Zimmerman. Quantum states and transitions in weakly connected superconducting rings. *Physical Review*, 157(2):317–341, May 1967. doi:10.1103/PhysRev.157.317. 7

SimBio. A generic environment for bio-numerical simulations, 2011. URL `https://www.mrt.uni-jena.de/simbio`. last accessed: March 1, 2011. 32

M. Soleimani. *Image and Shape Reconstruction Methods in Magnetic Induction and Electrical Impedance Tomography*. PhD thesis, University of Manchester, 2005. 25, 59

M. Soleimani, W. R. B. Lionheart, A. J. Peyton, X. Ma, and S. R. Higson. A three-dimensional inverse finite-element method applied to experimental eddy-current imaging data. *IEEE Transactions on Magnetics*, 42(5):1560–1567, May 2006. doi:10.1109/TMAG.2006.871255. 25, 59

G. W. Stewart and J. Sun. *Matrix Perturbation Theory*. Academic Press, 1990. 20, 21

A. Tarantola. *Inverse Problem Theory and Methods for Model Parameter Estimation*. Society for Industrial and Applied Mathematics, 2005. URL `http://www.ipgp.fr/~tarantola/Files/Professional/Books/InverseProblemTheory.pdf`. 9

P. P. Tarjan and R. McFee. Electrodeless measurements of the effective resistivity of the human torso and head by magnetic induction. *IEEE Transactions on Biomedical Engineering*, BME-15(4):266–278, October 1968. doi:10.1109/TBME.1968.4502577. 3

A. N. Tikhonov. Solution of incorrectly formulated problems and the regularization method. *Soviet Mathematics Doklady*, 4:1035–1038, 1963. 16

Y. Tsaig and D. L. Donoho. Breakdown of equivalence between the minimal ℓ^1-norm solution and the sparsest solution. *Signal Processing*, 86(3):533–548, 2006. doi:10.1016/j.sigpro.2005.05.028. 18

A. M. Turing. Rounding-off errors in matrix processes. *The Quarterly Journal of Mechanics and Applied Mathematics*, 1(1):287–308, 1948. doi:10.1093/qjmam/1.1.287. 19

M. Vauhkonen. Personal communication, July 2008. 8

M. Vauhkonen, M. Hamsch, and C. H. Igney. Imagereconstruction approaches for philips magnetic induction tomograph. In R. Magjarevic, H. Scharfetter, and R. Merwa, editors, *Proceedings of the 13th International Conference on Electrical Bioimpedance and the 8th Conference on Electrical Impedance Tomography*, volume 17 of *IFMBE Proceedings*, pages 468–471. Springer Berlin Heidelberg, 2007. doi:10.1007/978-3-540-73841-1_121. 13

M. Vauhkonen, M. Hamsch, and C. H. Igney. A measurement system and image reconstruction in magnetic induction tomography. *Physiological Measurement*, 29(6): S445–S454, June 2008. doi:10.1088/0967-3334/29/6/S37. 3, 59

C. R. Vogel. *Computational Methods for Inverse Problems*. Society for Industrial and Applied Mathematics, 2002. 17

G. Wahba. Practical approximate solutions to linear operator equations when the data are noisy. *SIAM Journal on Numerical Analysis*, 14(4):651–667, September 1977. doi:10.1137/0714044. 17, 45

S. Watson, R. J. Williams, W. Gough, and H. Griffiths. A magnetic induction tomography system for samples with conductivities below $10\,\mathrm{Sm}^{-1}$. *Measurement Science and Technology*, 19(4):045501, pp.1–11, April 2008. doi:10.1088/0957-0233/19/4/045501. 3

H. Weinstock, editor. *SQUID Sensors: Fundamentals, Fabrication and Applications*. Kluwer Academic Publishers, 1996. 3

Z. Zhang and L. Di Rienzo. Optimization of magnetic sensor arrays for current measurement based on swarm intelligence and D-optimality. *COMPEL: The International Journal for Computation and Mathematics in Electrical and Electronic Engineering*, 28(5):1179–1190, 2009. doi:10.1108/03321640910969430. 35

G. Zielke. Some remarks in matrix norms, condition numbers and error estimates for linear equations. *Linar Algebra and its Applications*, 110:29–41, 1988. doi:10.1016/0024-3795(83)90130-1. 19, 20

Index

List of Figures

List of Tables

Theses

1. Considering the linear inverse problem related to $y = Ax$ and the condition numbers

$$\kappa(A) = \|A\|_2 \, \|A^+\|_2 \quad \text{and} \quad \kappa(A, y) = \kappa(A) + \|A^+\|_2 \|y\|_2 / \|A^+ y\|_2 \, .$$

   The matrix condition number $\kappa(A)$ is also an adequate measure for the condition number of the inverse problem $\kappa(A, y)$, for any y, with the limitation

$$\kappa(A) \leq \kappa(A, y) \leq 2 \, \kappa(A) \, .$$

2. With respect to the floating-point relative accuracy ϵ, the values of κ are potentially inaccurate even in the order of magnitude, if $\kappa \geq \epsilon^{-1}$.

3. The newly proposed measure

$$\rho(A) = \frac{\sigma_1(A)}{\frac{1}{n} \sum_{i=1}^{n} \sigma_i(A)}$$

   enables a numerically robust determination of the condition.

4. To take regularization into account and to compare the condition for matrices with different numbers of singular values, κ^k and ρ^k can be used to determine the condition relative to the kth singular value.

5. By using tabu search for the optimization of sensor arrangements, the condition of the linear inverse problem in magnetocardiography can be improved considerably.

6. The reduction of the number of sources, particularly for underdetermined linear inverse problems, the extension of the source space beyond the sensor area, and the direction of sources toward the sensors are beneficial for the condition of the linear inverse problem in magnetic nanoparticle imaging.

7. Variations in mono-axial sensor directions and small variations in sensor positions of planar arrays lead to a better condition of the magnetostatic linear inverse problem.

8. The sensitivity to conductivity changes in MIT exponentially decays by several orders of magnitude within a range of a few centimetres. Measurement setups with relatively large coils that cover the measurement region almost completely improve the sensitivity clearly.

9. The predefinition of source directions in the lead field matrix is not improving the condition in general, although the number of unknown source parameters is reduced by a factor of 2/3. Benefits for the condition mainly arise when by predefining the source directions the linear inverse problem is considerably overdetermined.

Erklärung

Ich versichere, dass ich die vorliegende Arbeit ohne unzulässige Hilfe Dritter und ohne Benutzung anderer als der angegebenen Hilfsmittel angefertigt habe. Die aus anderen Quellen direkt oder indirekt übernommenen Daten und Konzepte sind unter Angabe der Quelle gekennzeichnet.

Stephan Lau stellte mir unentgeltlich die in Abschnitt 4.2.3 dieser Arbeit genutzten Simulationsdaten und Ergebnisse zur Verfügung. Diese basieren auf unserer gemeinsamen Publikation Lau et al. [*IEEE Trans. Magn.*, 4(6):1442–5].

Weitere Personen waren an der inhaltlich-materiellen Erstellung der vorliegenden Arbeit nicht beteiligt. Die Arbeit wurde bisher weder in gleicher noch in ähnlicher Form einer Prüfungsbehörde vorgelegt.

Ich bin darauf hingewiesen worden, dass die Unrichtigkeit der vorstehenden Erklärung als Täuschungsversuch angesehen wird und den Abbruch des Promotionsverfahrens zur Folge hat.

Ilmenau, 29. September 2011 Roland Eichardt